POLITECNICO DI TORINO

Collegio di Ingegneria Chimica e dei Materiali

Master of Science Course
in Materials Engineering for Industry 4.0

Master of Science Thesis

Analysis of the structural evolution of Ce and La-based metallic glasses during annealing

Tutors

Prof. Silvia Spriano, Politecnico di Torino
Prof. Eloi Pineda Soler, Universitat Politècnica de Catalunya
Prof. Pere Bruna Escuer, Universitat Politècnica de Catalunya

Candidate

Maria Aimetti

March 2025

Abstract

Metallic glasses are a class of materials developed since the 1960s that have gained increasing interest due to their unique properties. Among the most important aspects to study for potential applications are thermal stability and the thermally induced transformations that the material might undergo during use. This study aims to investigate the structural changes that a family of metallic glasses of composition $(Ce_xLa_{1-x})_{65}Al_{10}Co_{25}$ (x=1, 0.7, 0.6, 0.5, 0.4, 0.3, 0) undergoes when heated from room temperature to about 380 ºC. The analyzed samples are in the form of ribbons produced using the single wheel melt spinning technique. Combining Differential Scanning Calorimetry (DSC) analysis with Small-Angle X-ray Scattering (SAXS), Wide-Angle X-ray Scattering (WAXS) and Focused Ion Beam Scanning Electron Microscopy (FIBSEM) analyses allowed for the comparison of the structures of various samples in terms of system order and density as the temperature increased. The study concluded that, following an initial structural relaxation present for each composition, a liquid-liquid transition occurs, in some cases accompanied by what could be a dissociation of the resulting liquid in regions of different chemical composition, which precedes crystal nucleation and growth.

INDEX

1 Introduction

Metallic glasses, also known as amorphous metals, are a class of materials which have attracted a lot of interest due to their unique properties, resulting from their non-crystalline structure, that have both functional and engineering application potential. This class of materials have been first discovered in the 1960s and have attracted growing interest in both scientific and industrial fields. They are produced by rapidly cooling the molten metal at a rate high enough to prevent the atoms from organizing into the orderly structures typical of the crystalline state. Over the years, many studies on this class of materials have focused on developing new compositions that are sufficiently stable in an amorphous form and on determining their properties. Since the stability of metallic glasses is favoured by variety in terms of size of the constituent atoms, the possible combinations of elements are numerous, each bringing unique properties determined by the elements they contain and their relative quantities. Among the possible compositions, there are cerium-based glasses and lanthanum-based glasses, which exhibit different mechanical, magnetic and thermal properties. However, by producing glasses that contain both element, one can obtain intermediate properties determined by the relative amounts of these two elements. In this work, the class of composition $(Ce_xLa_{1-x})_{65}Al_{10}Co_{25}$ will be subjected to an increase in temperature, and through WAXS/SAXS, DSC and FIBSEM analyses, the structural variations that the material might undergo will be studied. This operation is important because it allows us to understand the thermal stability of metallic glasses to determine their suitability for high-temperature applications. Moreover, this class of materials is of great scientific interest for studying the glass transition and the process preceding crystallization due to the slow transformation dynamics. The work is divided into four chapters, in addition to this introductory one:

Chapter 2 provides an overview of metallic glasses, presenting their properties, history, and possible applications. At the end of the chapter, a paragraph is specifically dedicated to

cerium-based and lanthanum-based metallic glasses and the studies conducted so far on them.

Chapter 3 explains the process used to produce the samples, the analysis technique employed, with particular attention to the theoretical principles behind the WAXS/SAXS analysis, and the data processing steps.

In chapter 4, the results obtained for four of the analysed compositions are presented and discussed, and a comparison is made to highlight similarities and differences in behaviour as the content of cerium and lanthanum varies.

Chapter 5 summarizes the conclusions and proposes further analytical methods that could be useful for a complete characterization of these materials.

2 Metallic glasses

Metallic glasses are amorphous metals or alloys produced by preventing the formation of a crystalline structure. In this chapter will be made an introduction about the differences between the crystalline and the glassy state, and then this class of glasses will be presented in terms of history, structure, properties and applications, lastly, Ce and La-based metallic glasses will be introduced, along with the studies conducted on them so far.

2.1 Crystals and glasses

Cooling a melt to a temperature lower than the melting temperature T_m, the system can evolve in two different forms: a crystalline material or a glass.

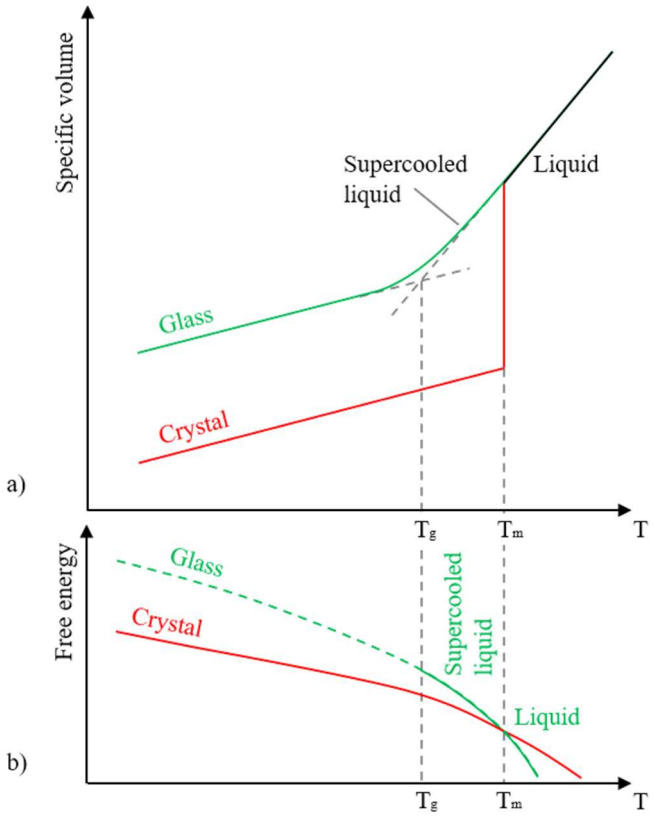

***Figure 2.1**: variation of volume (a) and free energy (b) with temperature for a glass and a crystalline material*

During cooling, as long as the temperature is higher than the melting point, the melt is stable (as can be seen from figure 2.1b if $T > T_m$ the liquid has a free energy lower than that of the crystalline solid), so the system remains liquid reducing its volume as temperature decreases (Figure 2.1a). When temperatures fall below the melting temperature ($T < T_m$), the liquid becomes metastable, is referred to as supercooled liquid and can evolve along two different paths, leading to its transformation into either a glass through the glass transition or a crystalline solid through the phase transition [1].

2.1.1 Liquid to crystalline solid: phase transition

As shown in figure 2.1b at temperatures below T_m, the free energy of crystal is lower than that of the liquid. Since any system tends to minimize its energy, this difference of energy constitutes the driving force for the crystallization process [2]. As can be observed in figure 2.1a a discontinuous decrease in volume corresponds to the formation of the crystalline solid. This is a first-order phase transition: as long as liquid and solid phase coexist, the equilibrium temperature of the system remains constant and equal to the melting temperature [3].

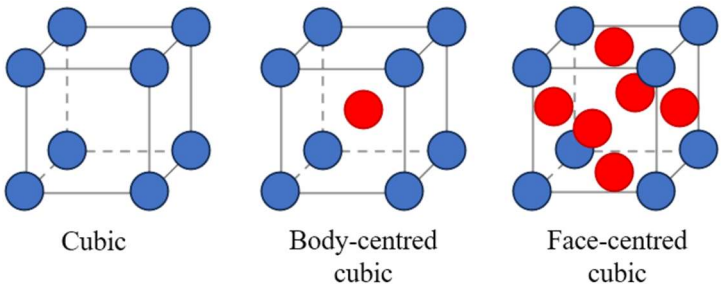

***Figure 2.2**: cubic, body-centred cubic and face-centred cubic crystalline cells*

From a structural point of view, crystalline solids are characterized by long-range order because their microstructure is periodic: each crystal can be represented as a symmetric translation of his unit cell in three-dimensional space. These cells consist of atoms ordered in well-defined geometric shapes [4]. Figure 2.2 shows the cubic, the body-centred cubic (bcc) and the face-centred cubic (fcc) unit cells, which are the primary elementary cells constituting crystalline solids. To crystallize, atoms must organize themselves in these ordered structures, so in addition to the thermodynamic aspects it is important to consider the kinetics of this process.

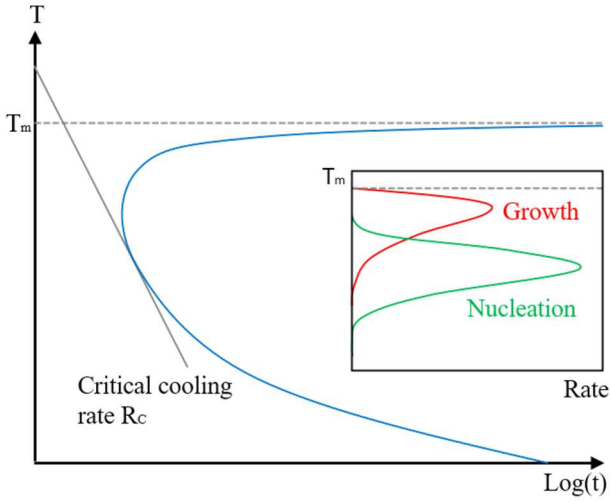

***Figure 2.3**: TTT curve for crystallization process. In box: growth and nucleation ratesas a function of temperature*

Crystallization is the result of two phenomena: nucleation, typically initiated by impurities in the melt or the walls of the container, and subsequent growth of these nuclei through an orderly aggregation of surrounding atoms. As represented in figure 2.3 (inset) the nucleation is favoured by low temperatures (high undercooling $\Delta T = T_m - T$) because lower kinetic energy leads to more stable nuclei, while the growth is favoured by higher temperatures (lower undercooling $\Delta T = T_m - T$) as the atoms can easily reach the nuclei and bind to them. Being the crystallization given by these two contributions the time-temperature-transformation curve (TTT) presents a sort of nose (Figure 2.3). This TTT curve represents, in correspondence of the temperatures at which the melt can be exposed, the time that is necessary to obtain a fraction of crystallization $X_V = X_V^{\circ} = 1 \times 10^{-6}$ (typically this value is regarded as a threshold to obtain a material that can be considered crystalline) [5]. Considering the tangent of the curve it represents the critical cooling rate R_C: if the cooling rate is higher than R_C the crystallization is avoided because the atoms do not have time to organize themselves and the result of the cooling process is a glass [1][5].

2.1.2 Liquid to glass: glass transition

As mentioned in the previous paragraph, cooling the melt with a cooling rate higher than the critical cooling rate R_C can lead to vitrification of the melt, indeed a glass can be defined as an amorphous solid produced by the rapid cooling of a melt at an average rate R higher than the characteristic critical speed R_C of the liquid [6]. During this rapid cooling, there is a

gradual decrease in the mobility of molecules until the liquid's configuration freezes, which occurs at a temperature known as the glass transition temperature (T_g). It has been experimentally observed that T_g (related to the mobility of molecules) corresponds to a temperature at which viscosity reaches 10^{12} Pa·s. The nature of T_g can be explained by considering the dependence of certain properties of the liquid on temperature: from figure 2.1 a, it is evident that for $T > T_g$, the volume is strongly dependent on temperature because the still sufficiently high mobility allows for configurational changes in the liquid. For $T < T_g$, however, the mobility of atoms within the melt is so reduced that there is not enough time for these configurational changes to occur. At this point, the volume reduction with temperature is analogous to that of the crystalline solid, as it is due to thermal contraction [1][3]. The system obtained, being a frozen liquid, is characterized by the lack of periodicity and long-range order in the structure (figure 2.4).

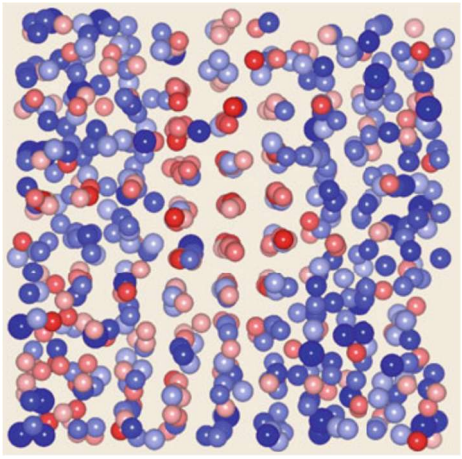

***Figure 2.4**: atomic structure of a glass [3]*

2.2 History of metallic glasses

The first case of metallic amorphous alloy in literature was reported in 1960 by Pol Duwez, who produced amorphous $Au_{75}Si_{25}$ by splat quenching, using as cooling mean a cold metal plate on which the droplets spread into a 10 μm layer. The cooling rate was higher than 10^6 K/s and allowed to obtain a glass structure [7][8]. Since that moment many researchers began to study and produce metallic glasses with different compositions and properties using different techniques. The obtained metallic glass samples had a very limited size, due to the high critical cooling rate ($10^6 – 10^8$ K/s) necessary to avoid the crystallization [9]. This limit has pushed the research to investigate possible compositions that allowed to obtain glass

structures through slower cooling, in order to produce larger samples. Turnbull in the early 1960s proposed a first criterion for establishing the glass forming ability (GFA) of a composition, based on the ratio of the glass-transition temperature to the melting point [10]. Over the years new studies have been carried out, new criteria identified, and new production methods developed, allowing, in 1974, to produce the first bulk metallic glass (BMG) with centimetre dimension. This sample was produced by Chen et al. from a ternary Pd-Cu-Si alloy by a suction-casting method, in form of rods of the metallic glass at cooling rate of 10^3 K/s [11]. In 1982 Turnbull and coworkers prepared a Pd-Ni-P BMG using boron oxide fluxing to dissolve heterogeneous nucleants. Doing this it was possible to obtain a centimetre size ingot solidified at cooling rates of the order of 10 K/s [10][11]. All the BMGs obtained during those years were based on the noble metals of palladium and platinum, which had been seen to be excellent for improving the glass forming ability. The main problem with these elements, which led to a temporary halt in BMGs research, is that they are very expensive, and therefore not usable in a wide range of applications [7]. The breakthrough in BMG research came with the discovery of multicomponent glass formers by Inoue and coworkers at Tohoku University. These new bulk glassy alloys exhibit excellent high forming ability and low critical cooling rates, like those of the noble metal-based metallic glasses [7]. In these alloys, cooling speeds down to 1 K/s allow the production of bulk metallic glasses, reaching dimensions of some centimetres. In Figure 2.5 are shown some of the samples.

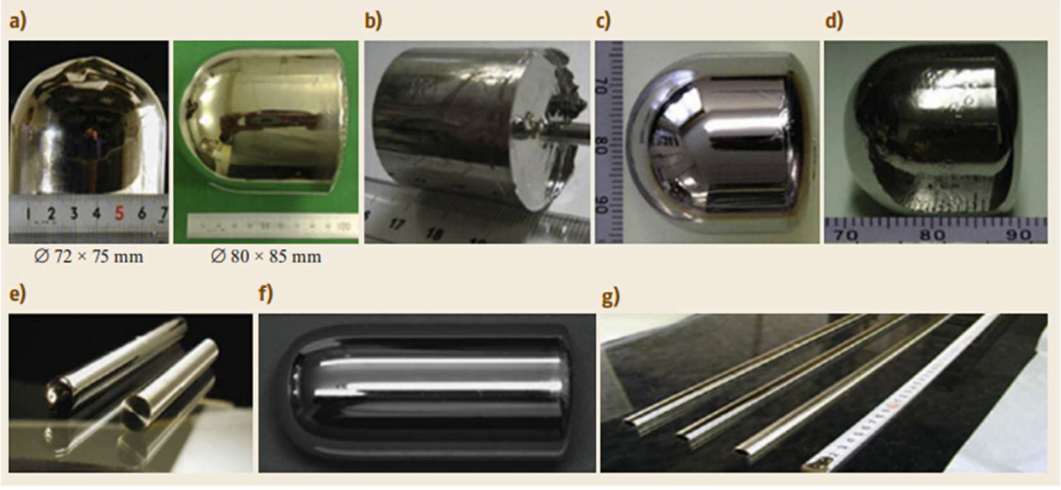

***Figure 2.5**: Examples of bulk metallic glasses: (a) Pd-Cu-Ni-P, (b) Zr-Al-Ni-Cu, (c) Cu-Zr-Al-Ag, and (d) Ni-Pd-P-B. Cylindrical rods: (e) Pd-Cu-Ni-P and (f) Pt-Pd-Cu-P. Hollow pipes: (g) Pd-Cu-Ni-P [3]*

2.3 Important characteristics

For a metal alloy to be used in its glassy state it is important that its composition allows the formation of a glass structure and that this is maintained over time. The intrinsic properties to evaluate these abilities are the glass forming ability and the thermal stability.

2.3.1 Glass-Forming Ability

The glass forming ability is defined as the ease of vitrification for a material. This parameter is used to design and identify a range of glassy alloys. In the case of cooling from melt, a higher GFA implies a lower critical cooling rate and a higher section thickness for the glass sample [12][13]. By comparing the alloys with which BMGs have been obtained and by looking for their common characteristics, different methods have been theorized to try to evaluate the GFA of a composition a priori. In this paragraph these theories will be presented.

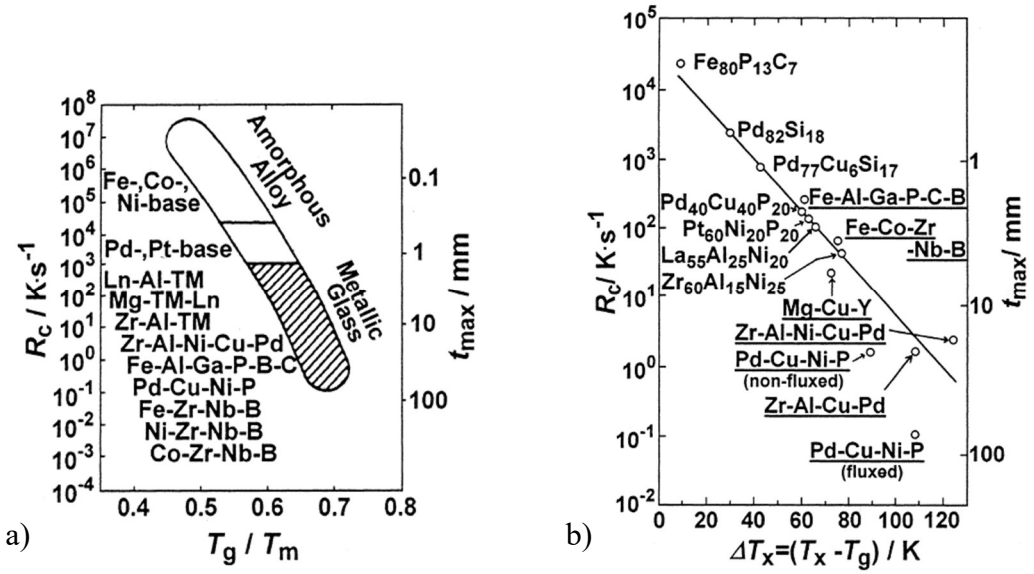

***Figure 2.6**: (a) Relationship between the critical cooling rate for glass formation (R_c), maximum sample thickness for glass formation (t_{max}) and reduced glass transition temperature (T_g/T_m) for bulk amorphous alloys. The data of the ordinary amorphous alloys, which require high cooling rates for glass formation, are also shown for comparison. (b) Relationship between R_c, T_{max} and the temperature interval of the supercooled liquid region between T_g and T_x, ($\Delta T=T_x-T_g$) for bulk amorphous alloys. [15]*

As mentioned in the previous paragraph the first criterion was introduced by Turnbull. He observed that as the ratio of the glass-transition temperature to the melting point of an alloy (referred to as the reduced glass-transition temperature $T_{rg} = T_g/T_m$) increased from values near 1/2 to values near 2/3, the homogeneous nucleation of crystals becomes very slow [14]

allowing to obtain a glass with lower cooling rates. The relationship between the critical cooling rate for glass formation, maximum sample thickness and reduced glass transition is reported in figure 2.6a.

Another theory associates the GFA to the stability of the metallic supercooled liquid, and so to the amplitude of the supercooled liquid region ΔT_X, defined as the difference between the onset crystallization temperature T_X and the glass transition temperature T_g [13]. The relationship between the critical cooling rate for glass formation, maximum sample thickness and the amplitude of the supercooled liquid region is reported in figure 2.6b.

Based on the experimental data in literature Inoue established three rules that all the amorphous alloys seems to have [15]:

- multicomponent systems consisting of more than three elements
- significant difference in atomic size ratios above about 12% among the three main constituent elements
- negative heats of mixing among the three main constituent elements

The reason why these three empirical rules are associated to high GFA are not clear, but some possible explications have been proposed. The first rule has been understood by the 'confusion principle': the higher the quantity of elements in the composition, the lower the chance that the alloy can select viable crystal structures. [7]. The second rule is explained by considering that differences in the atomic size lead to stresses in the lattice that frustrate the crystallization [13]. Also, the second rule is associated to the packing of atoms [16]: for a better GFA it is necessary to have a higher density, as a high packing density tends to reduce voids and defects, making the formation of crystalline structure less likely [7]. The third rule is essential for mixing of atoms and for the formation of a homogeneous glassy phase [16]. Considering the phase diagrams is possible to state that the multicomponent alloys with the three empirical rules always have very deep eutectic valleys – with low melting temperatures, leading to high T_{rg} and large ΔT_X [15] – that decreases the amount of undercooling needed to vitrify the liquid [13]. This is due to the long-range atomic diffusion needed for the crystallization of at least two phases [17]. Related to that it is important to know that good glass formers usually have compositions close to the eutectic.

2.3.2 Thermal stability

At temperatures below the glass transition temperature the system is in a metastable equilibrium condition, so it will tend to reach a more stable state, either the supercooled liquid state or the crystalline state. The former evolution is called structural relaxation and lead to a more stable disordered state, while the latter one corresponds to crystallization [3].

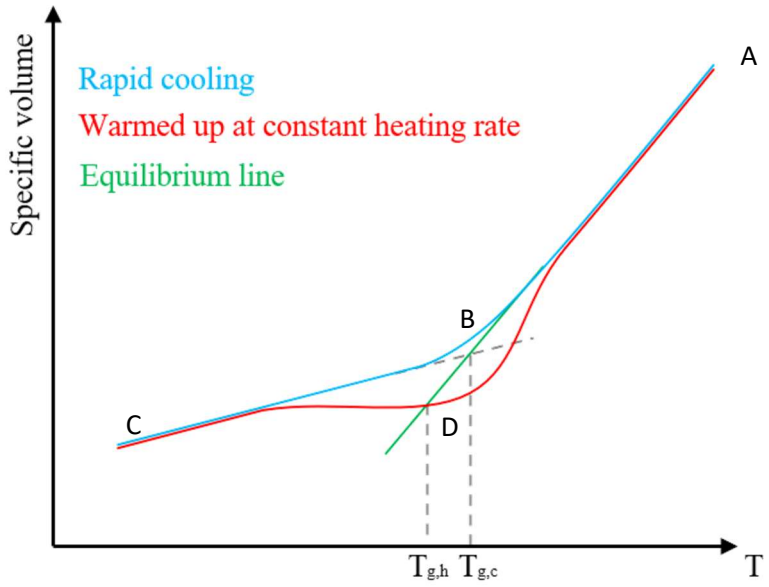

***Figure 2.7**: free volume of a glass during its production by rapid quenching and a subsequent heating.*

To better understand the phenomenon of structural relaxation, consider the Figure 2.7, where is represented the free volume of a glass during its production by rapid quenching and a subsequent heating. During the rapid quenching of the melt to produce the glass, at higher temperatures (AB) the kinetics of free volume annihilation is fast enough to maintain the equilibrium. In the low temperature region (BC) the kinetics is slow and cause an excess (non equilibrium) amount of free volume which is frozen. As stated before the volume reduction at these temperatures is only due to thermal contraction. If the glass obtained is warmed up at a constant heating rate (for example into a DSC) it tends to move towards the equilibrium state (CD) through atomic rearrangements; this is an exothermic process. At D the warmed up glass crosses the equilibrium line because the kinetics is too slow to follow that line. From now on the volume of the glass is smaller than expected from its equilibrium state, so new free volume must be produced to reach the equilibrium line; this is an endothermic process [18].

2.3.3 Polyamorphism

It is well known that crystalline solids, when subjected to changes in pressure and temperature, can undergo phase transitions and transform into the most stable polymorphic form under various conditions. Recent studies have highlighted the existence of similar transitions for amorphous solids and liquids: it has been demonstrated that the same composition can exist in different liquid states (liquid polymorphism), and the transition between them is called liquid-liquid transition (LLT). Similarly, the same composition can exist in different amorphous states (polyamorphism), and the transition between these is called an amorphous-amorphous transition (AAT). About that, one of the most well-studied systems is water; in fact, the existence of two amorphous forms of water has been verified: high-density ice and low-density ice. Being the amorphous solids obtained by freezing the atoms of the liquid, it has been hypothesized that there are two corresponding liquids, also with high and low density. However, further studies are being conducted to better understand this correspondence [19]. Similar phenomena have been observed for metallic glasses.

2.4 Structure

As mentioned in previous paragraphs, the structure of metallic glasses is characterized by lack of long-range order. However, common sense and experimental results [20] suggest the presence of a short-range (SRO) [21] and medium-range (MRO) orders [22] where the short-range order can be defined as the local structures formed by the atoms and their nearest neighnors, while the medium is defined as the next-level structural organization beyond the SRO, for example how the local units are connected and arranged to fill three dimensional space [22]. The details of how atoms are packed in metallic glasses are not well understood, and structural models have not been established yet, but over the years some theories have been developed.

The dense random packing model proposed by Bernal in 1960 regards the atoms as incompressible hard spheres stacked as closely as possible through random dense packing [21]. Now it is well understood that Bernal's idea can only model monoatomic systems (and also alloys with comparable atomic sizes of constituents) but fail to describe binary metallic glasses as it does not reflect the short and medium order observed in real samples being based on purely geometrical aspects [7][22]. The most recent models have considered, in addition to geometry, the chemical interactions between atoms to describe the SRO and the

MRO. In theories developed later the short-range order was explained by introducing the concept of atomic cluster, while the medium-range order was interpreted as the organization of these cluster in space.

2.4.1 SRO: organization of atoms in clusters

Clusters are structures consisting of an inner sphere and k other spheres in contact with it. They can be designated as (1 + k) clusters (shown in figure 2.8).

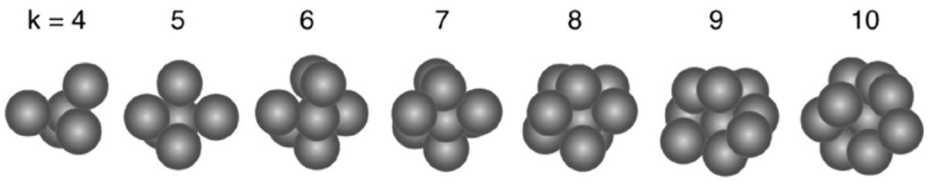

***Figure 2.8**: clusters of irregular shape and varying coordination comprising spheres of the same size [23]*

In a glassy structure these clusters are constituted by atoms, are usually solute centred and can be characterized by a number of parameters such as coordination number (k), geometrical structure and chemical composition [23].

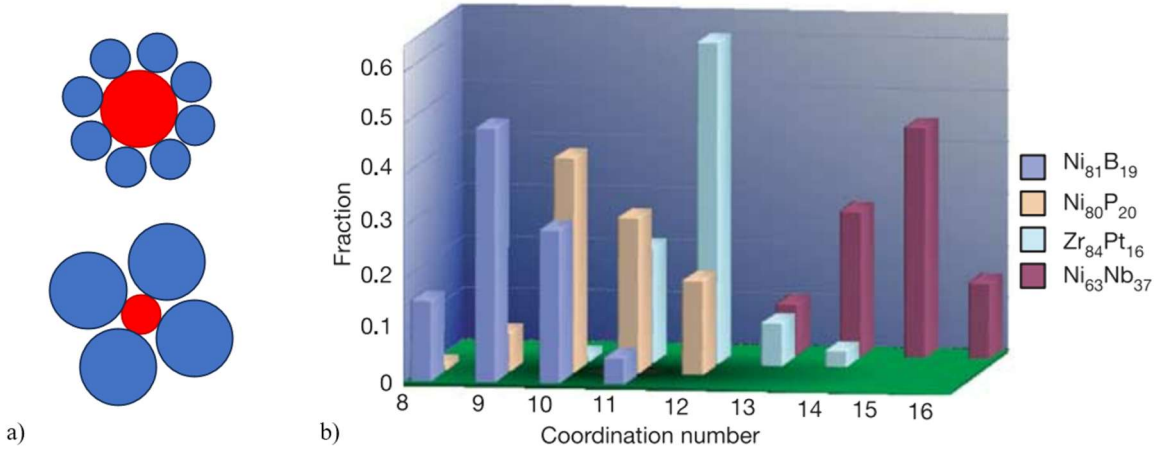

***Figure 2.9**: (a) 2D cluster scheme: different coordination number for different size ratio R*. (b) Average coordination number changes for different binary alloys having different atomic size ratio R* [22].*

Chemical composition and coordination number are correlated as the number of atoms which is probable to find in contact with the centred one depends by the size ratio R* between the

solute and the solvent, as evident in figure 2.9. Regarding the possible geometric structures of clusters these can be defined through the Voronoi tessellation method: each solute atom is associated to a Voronoi polyhedron (locus of all the point that are closer to that atom than to any other) characterized by a Voronoi index $<n_3,n_4,n_5,n_6,\ldots>$, where n_i represents the number of i-edges faces. According to this the coordination number for each atom is given by $\sum_i n_i$. Also, the preference of a particular type is controlled by the effective atomic size ratio [22].

Each one of the metallic glasses have several types of local coordination polyhedral not identical in topology and coordination number. Nevertheless, they can be considered quasi-equivalent clusters, due to their similar size and to the fact that the coordination number is distributed with a small variance around a certain average value controlled by R* [22].

2.4.2 MRO: packing of quasi-equivalent clusters

According to some more recent models, the medium-range order in metallic glasses is given by the way these clusters are connected in 3D space. According to the efficient cluster packing model proposed by Miracle [24][25] the solute centred clusters are organized in a distorted face centred cubic-like structure without any orientational order; in this structure, shown in figure 2.10, adjacent clusters share solvent atoms in common faces, edges or vertices so that neighbouring clusters overlap in the first coordination shell.

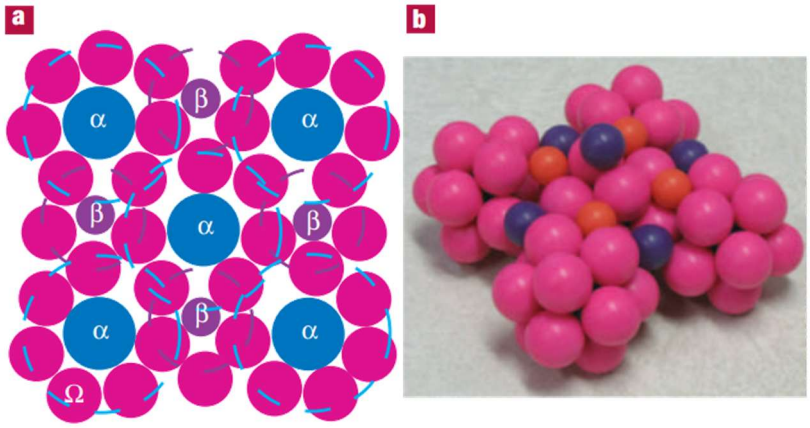

***Figure 2.10**: (a) A two-dimensional representation of a dense cluster-packing structure. (b) 3D model of a dense cluster-packing structure. The α sites are occupied by blue spheres, the β sites are occupied by purple spheres and the γ sites are occupied by orange spheres [24].*

Besides the solvent atoms (Ω) and the primary cluster-forming solute atoms (α) in this model are introduced two additional topologically distinct solutes: a secondary (β) solute that occupies cluster-octahedral interstices and a tertiary (γ) solute that occupies cluster-tetrahedral interstices. Despite the large number of possible elements in a metal glass, is considered that these belong to three topological classes based on the size ratio, so that this model can be used to describe also glasses with more than three solute elements [24]. According to other models such as the quasi-equivalent cluster model proposed by Ma et al. [22] clusters are not disposed in an FCC-like structure but in a non-strict icosahedral configuration [21]. For higher solute fractions there are other types of MRO given by the dense packing of 'extended clusters' (cluster centred not on a solute atom but on a string of solute atoms) or by the network-like arrangement of solute atoms [22].

A unified structure for metallic glasses has not been determined so far, but the research on SRO and MRO in metallic glasses is going to continue in future years to gain a better understanding of these materials.

2.5 Manufacturing processes

As discussed previously the first amorphous metallic alloy was produced by applying a rapid quenching method with a cooling rate of ~10^8 ºC/s. Since then many studies have been carried out to develop other manufacturing processes. In this paragraph a brief overview of the methods used for the production of metallic glasses will be provided.

2.5.1 Rapid quenching and water-quenching methods

The first methods developed are based on rapid quenching, which, by preventing the rearrangement of atoms, avoids crystallization and allows the formation of an amorphous structure, as described in the first paragraph of this chapter. Examples of these methods are the twin roller quenching, the melt spinning technique, and the pendant-drop melt extraction, schematized in figure 2.11 . All these rapid quenching techniques reach a cooling rate range of 10^4-10^8 K/s. In the third paragraph a few words will be spent on the melt spinning technique as it is the one used to produce the samples studied in this work. For some compositions it is sufficient a cooling rate of 10-100 ºC/s to obtain an amorphous structure. These values can be achieved through water quenching method. In this process the sample is heated at a specific temperature for a predetermined time, and then immersed into the

quenching medium. With this method samples with few centimeters diameters can be prepared. One of the main advantages of this method is low stress due to the low cooling rates [26].

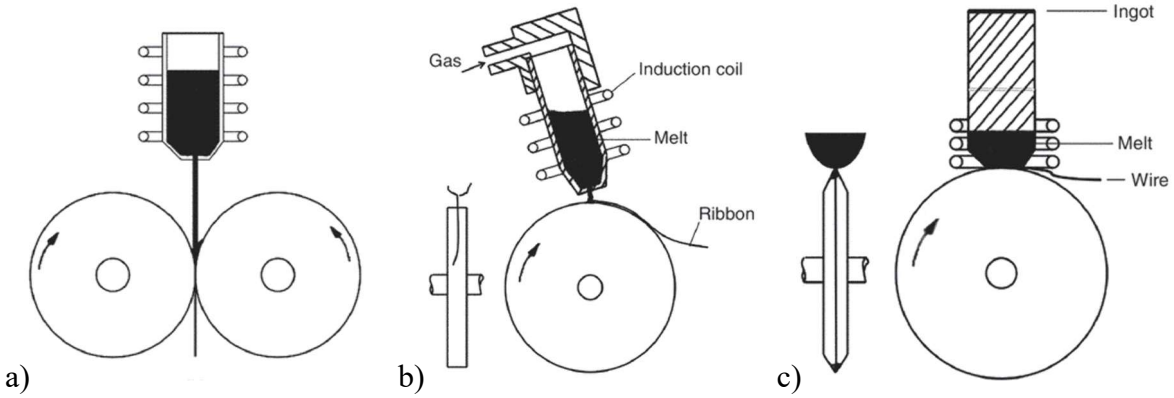

***Figure 2.11**: some common rapid quenching methods. (a) Twin roller quenching technique, (b) melt spinning technique and (c) pendant-drop extraction technique [26].*

2.5.2 Severe plastic deformation

Plastic deformation of a crystalline solid can introduce defect such as dislocations and vacancies. If the material is highly deformed, the concentration of introduced defects is such that the crystalline structure disappears. The main techniques of severe plastic deformatioin are ball milling, equal channel angular extrusion (ECAE) and high pressure torsion (HPT) [3]. The first one is used for powders and platelets: the particles are loaded into a rotating drum with balls of grinding media. The collision and friction between the particles and the balls lead to the reduction in powder size and the introductioin of defects. One of the problems of this process is that it can take up to one or two days. HPT and ECAE are typically applied to bulk samples rather than particles. In HPT the sample is placed between two anvils that apply high pressure and torsion to the material inducting severe plastic deformation. The ECAE method consists of extruding the material through a channel with a constant cross-section. The channel is characterized by a certain angle (usually between 90º and 150º) to plastically deform the sample.

2.5.3 Vapor deposition

Physical vapour deposition can be used to obtain metallic glasses in the form of thin films. In particular, the most used technique is sputtering. In this technique a target material is deposited on a substrate. To do that both the materials are placed in a vacuum chamber where a gas is ionized to create a plasma. The ions from the gas are accelerated towards the target

causing the sputtering of the atoms of the target that deposit on the substrate. This method can be used for many compositions, even for unstable phases, as the atoms are isolated when reach the substrate, and, being the target cold, crystallization is avoided as no diffusion occurs.

2.5.4 Densification of amorphous powders

Amorphous particles produced by ball milling can be densified to obtain large sample geometries. This densification can be carried out at high temperature or at room temperature depending on the technique. At room temperature the methods are cold pressing and equal channel angular extrusion, while at high temperature the techniques are hot pressing, injection, warm extrusion and spark plasma sintering (SPS).

2.6 Properties and applications

The difference in structure between amorphous and crystalline alloys results in the unique properties of metallic glasses. These properties are controlled by the glass composition, but they are also dependent on the structure. Since the amorphous structure is a metastable phase the properties of metallic glasses are closely related to the formation history (controlled by parameters like time, process conditions,…) and to the service conditions, since structural relaxation can occur in the material due to temperature, pressure and service time [21]. In this paragraph will be presented the main properties of these materials and their usefulness in various fields of application.

2.6.1 Mechanical properties

Studies of mechanical properties of metallic glasses have been facilitated by the progress made in the field of glass production: as long as the samples were limited to small and irregular geometries, the studies were mostly concerned with thermal, electrical, magnetic and structural properties; when improved production techniques have made it possible to produce larger specimens, mechanical properties could also be tested. An initial comparison of the mechanical behaviour of metallic glasses with that of conventional materials can be made by looking at the Ashby plots.

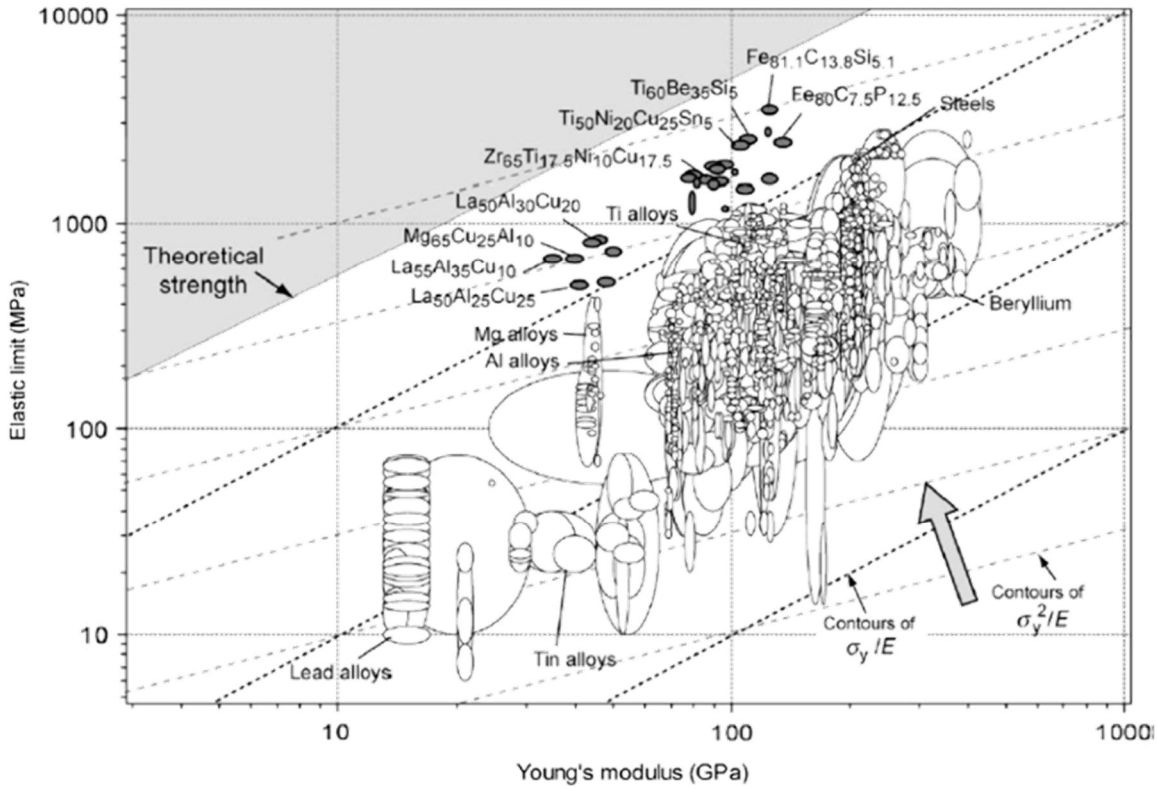

***Figure 2.12**: Elastic limit (yield stress) σ_y plotted against the Young modulus E for 1507 metals, alloys, metal-matrix composites, and metallic glasses (annotated with compositions in at. %). The contours are for elastic strain limit (σ_y/E) and resilience (σ_y^2/E). [8]*

Figure 2.12 is a map showing the elastic limit (yield stress) σ_y and Young's modulus E of some classes of materials. The metallic glasses have the unusual combination of high yield stress and low Young's modulus ($\sigma_y \approx E/20$). The main cause of the low Young's modulus of these materials is their disordered structure: compared to crystals, it imposes less constraints on atoms and leads, under stress, to local anelastic deformations, which result in a macroscopically lower stiffness. As regard the high yield stress values, unlike crystalline materials in which plastic deformation is due to the movement of dislocations under stress, metallic glasses do not have dislocations, so they resist deformation even under high loads. These features ensures that for this particular class of materials the merit indices associated with yield strain (σ_y/E) and resilience (σ_y^2/E measuring the capacity to store and return elastic energy per unit volume) are very high [1][8]. Metallic glasses therefore have an excellent behaviour in the elastic field, which makes them attractive for many applications, however they have some limitations in terms of plasticity and toughness that restrict their widespread use in various applications.

Since dislocations are absent in metallic glasses, studies have been and are being carried out to understand the deformation mechanism of these materials. Research have shown that the plasticity of amorphous alloys is very limited at room temperatures [7]. On the other hand, at higher temperatures a homogeneous deformation occurs [3]. As an example, Figure 2.13 shows stress-strain curves for a metallic glass ($Zr_{41.2}Ti_{13.8}Cu_{12.5}Ni_{10}Be_{22.5}$) obtained by Lu et al. testing the material in uniaxial compression at different temperatures.

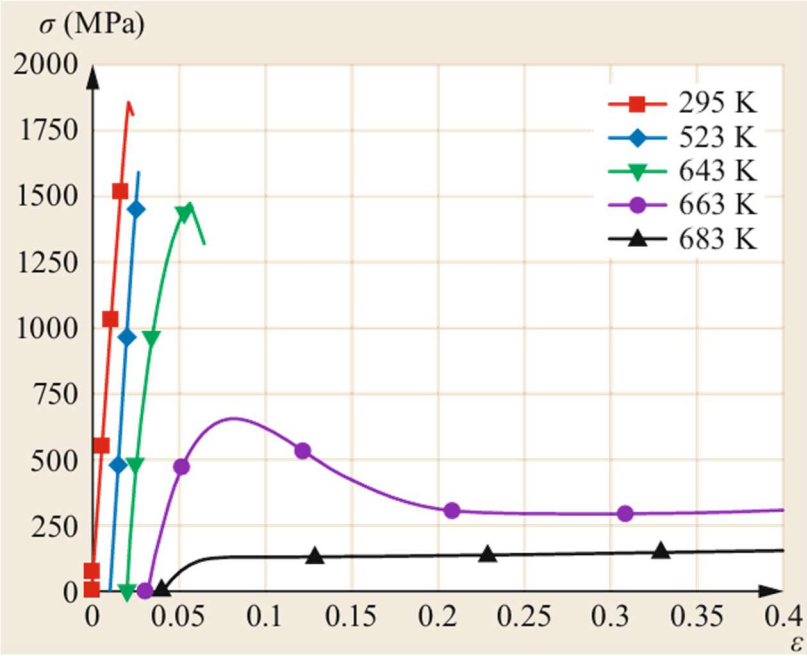

***Figure 2.13**: Stress-strain curves in compression at a given compression speed (1x10-1 s-1) for the different temperatures indicated (between 295 and 683 K) in the bulk glass $Zr_{41.2}Ti_{13.8}Cu_{12.5}Ni_{10}Be_{22.5}$.[3]*

At low temperature the plot is typical of a brittle material. The plastic deformation at this temperature is inhomogeneous both spatially and temporally and it tends to localize in shear transformation zones (STZs) which coalescence forming narrow zones called shear bands that can propagate quickly in the material. This mode of deformation, not seen in conventional glasses, results in unattractive surface markings, but is mainly of concern because it reduces the effective tensile ductility of the metallic glass to zero. The propagation of local shear in shear band is due to strain softening along a shear plane: contrary to what happens in polycrystalline metals in which, thanks to the movement of dislocations, the material hardens if plastically deformed, in metallic glasses the opposite behaviour occurs, so the bands, in which the deformation was located, are preferential sites for further plastic flow and lead to a brittle fracture which generally causes the sample to break along a single

band without the specimen having undergone macroscopic plastic deformation [7]. At higher temperatures, the yield stress is lower and catastrophic failure can be avoided. It has been determined that the temperature at which the material behaviour changes from brittle to ductile varies from 0.7 T_g and 1.1 T_g, depending on the metallic glass and the deformation conditions [3]. To improve the plastic behaviour of amorphous alloys at room temperature some solutions have been proposed. The most immediate solution is to create composites whose matrix is metallic glass and the dispersed phase is a ductile crystalline solid solution. Other proposals instead aim to modify the properties of the glass without adding other phases and go in two opposite directions: one proposal is to increase the density of bands (by cold-working or by surface treatment that initiate the shear bands), so as to reduce the stress supported by each one. This method improves compressive and bending plasticity and toughness, but can't provide the strain hardening behaviour, required to achieve significant ductility. The other proposal is to look for the strain hardening also in metallic glasses, to obtain the associated suppression of shear banding. Studies report that this is possible rejuvenating the samples to relax it, but the maximum attainable ductility of metallic glasses is only ~1 percent [27].

2.6.2 Other properties

In addition to the mechanical characteristics already seen, metallic glasses have other properties that make them interesting in various fields of application. One of these features is corrosion resistance: having a uniform structure free from grain boundaries, dislocations and stacking faults, which often act as initiation sites for localized corrosion, metallic glasses have good corrosion resistance, also because this homogeneity helps in the formation of a highly protective passive film without preferential nucleation sites for corrosion attack. Besides atomic homogeneity, corrosion resistance also depends on the composition of the glass, as it is possible to incorporate elements in the passive layer to protect the material or to retard the dissolution rate of the underlying metallic substrate [28][21].

Other attractive characteristics of metallic glasses are magnetic properties. Thanks to the disordered atomic arrangement, the structural isotropy and the high resistivity metallic glasses present high permeability and low loss, that make some of them excellent soft magnetic materials, which means that they can be easily magnetized and demagnetized requiring only small energy [21]. On the other hand it is important to highlight that some

metallic glasses exhibit hard magnet behaviour and therefore retain magnetization even in the presence of opposing fields.

2.6.3 Applications

As stated earlier, metallic glasses can be used as soft magnets, but not only: due to their mechanical, thermal, and physical properties, metallic glasses have emerged in various fields. As mentioned in the previous paragraph metallic glasses are characterized by high strength and lightweight. These properties make metallic glasses perfect for aeronautical field and sports applications, especially for equipment that must withstand high impacts and stresses while maintaining a certain lightness to improve athletes' performance. Examples in this field include tennis rackets, golf clubs and some parts of skis. Furthermore, having many possible compositions and being resistant to corrosion, metallic glasses are characterized by good biocompatibility, which makes them suitable for use in the biomedical field. Because of their excellent formability at a not very high temperature metallic glasses can also be used to manufacture microgears and microtools for microsystems but also jewellery. Finally, metallic glasses can conduct sound energy efficiently improving the sound quality of musical instruments [3].

2.7 RE-based metallic glasses

The elements belonging to the rare earth (RE) class are often used as minor binders or main constituents in rare earth based bulk metallic glasses (REBMG). Rare-earth-based metallic glasses have variable thermal and mechanical properties: their glass transition temperatures range from 330 K to 700 K, and their Young's moduli range from 30 to 80 GPa, depending on the element chosen as the base for the metallic glass. As for the magnetic properties of REBMGs some exhibit hard magnetic properties (for example those based on neodymium), while others (based on Ce and La) seem to exhibit paramagnetic behaviour. Additionally, metallic glasses based on gadolinium exhibit a significant magnetocaloric effect, which is useful for applications in magnetic refrigeration [29].

2.7.1 Cerium and lanthanum

To develop a metallic glass composition one element is selected as a base, but it is also possible to base the metallic glass on two elements with different properties: by changing

the amount of those two elements in a range without deteriorating the glass-forming ability it will be easier to tune the properties of the metallic glass. The base of the metallic glasses studied in this work are Cerium and Lanthanum, whose atomic properties are summarized in the table 2.1.

	Lanthanum (La)	Cerium (Ce)
Atomic number	57	58
Atomic weight	138.9055	140.12
Atomic radius	240 pm (Van der Waals)	235 pm (Van der Waals)
Electron configuration	$[Xe]5d^16s^2$	$[Xe]4f^15d^16s^2$
Oxidation states	3	3, 4

***Table 2.1**: atomic properties of cerium and lanthanum*

Cerium and lanthanum have similar atomic radii but different properties due to their different electronic structures. These different properties of the constituent elements translate into different properties of the metallic glasses that contain them. Below, the main properties studied for cerium-based metallic glasses and lanthanum-based metallic glasses will be presented. Producing glasses that contain both elements it is possible to obtain intermediate properties.

2.7.2 Ce-based metallic glasses

Cerium-based metallic glasses typically include cerium (Ce) as the primary element, combined with other elements such as aluminium (Al), copper (Cu), nickel (Ni) and cobalt (Co) [30][31]. Among the most important and studied properties of these glasses are the low glass transition temperature and melting temperature, comparable to those of polymers, and the slow transformation dynamics, related to the high stability of the glasses, which make these materials of scientific interest as a model system for investigating the processes of glass transition and transformations preceding crystallization. Furthermore, regarding mechanical properties, cerium-based metallic glasses have the lowest elastic constants (E, G and K) among the metallic glasses developed so far. Ce-based metallic glasses are interesting for the fabrication of microcomponents and phase-change erasable optical storage, given their super plasticity at low temperatures [30][32]. Finally, among peculiarities of these materials is the tendency to undergo an amorphous-amorphous transition from a low-density amorphous (LDA) to a high-density amorphous (HAD) under pressure and at high temperatures [33]. This transition is accompanied by a change in the electronic structure of

Ce, consisting of the delocalization of the 4f electronic states. Similar to what happens in pure cerium, where this electronic transition leads to a volume collapse that cannot be explained by simple compression, cerium-based metallic glasses also exhibit volume reductions of 10-15% during amorphous-amorphous transitions [34][35][36].

2.7.3 La-based metallic glasses

Lanthanum-based metallic glasses contain, in addition to La, also Ni, Al and Co. Regarding these glasses, the papers in the literature mainly address the topic of secondary relaxation: the structural relaxation mentioned in paragraph 2.3.2, known as α-relaxation, is a universal characteristic of metallic glasses, observable in all amorphous materials and irreversible [37][38][39]. This type of relaxation is related to the glass transition and represent a large-scale movement of atoms. Some metallic glasses, such as those based on lanthanum, undergo secondary relaxation, also known as β-relaxation, which is reversible. This phenomenon occurs at lower temperatures compared to α-relaxation, is associated with dynamic heterogeneities and it depends on local and limited movements of atoms and defects in glasses. It was found that the β relaxation is related to mechanical properties of the glass [40]. Studies on secondary relaxation conducted on lanthanum-based metallic glasses have revealed a correlation between the activation energy of β-relaxation and STZs events, which have the same value. Therefore, a glass with pronounced β-relaxation will be characterized by a structure that favours the activation of STZs potential. It is thus believed that β-relaxation could be an indicator for toughening [41].

2.7.4 (La-Ce)-Al-Co metallic glasses

(La-Ce)-Al-Co metallic glasses are a class of pseudo-ternary alloys obtained through row substitution: starting from an A-B-C system (with B=Al and C=Co) a mixture of cerium and lanthanum atoms in different proportion was used as A. This type of operation is called row substitution because cerium and lanthanum are neighbouring elements and belong to the same raw in the periodic table, thus having similar atomic size but different valences and electronic structures, as already mentioned at the beginning of the paragraph. Ran Li et al. [42] investigated composition $(La_xCe_{1-x})_{65}Al_{10}Co_{25}$, particularly its GFA in relation to the substitution of La with Ce and vice versa: it was concluded that the coexistence of Ce and La in the glass increases its GFA. This cannot be explained by conventional criteria seen in paragraph 2.3.1 (the ΔHmix between Ce and La is 0 kJ/mol and the difference between their

atomic radii is small). Therefore, a model based on the system's thermodynamics was proposed: the lower ΔG, due to the configurational entropy, provides a reasonable explanation for this higher GFA.

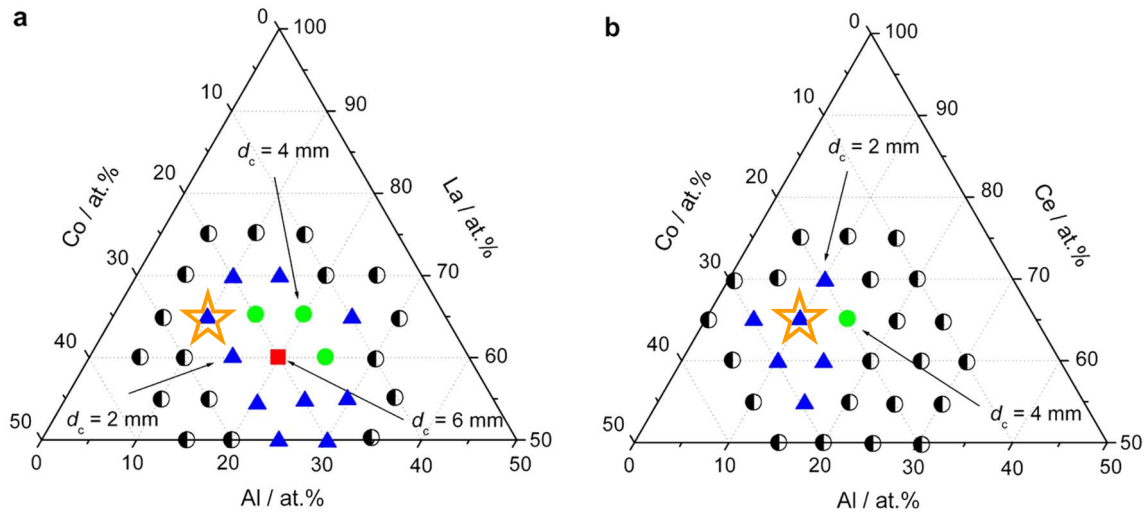

***Figure 2.14**: composition map for the glass-forming range in the La-Al-Co (a) and Ce-Al-Co (b). The symbols represent: ▲, BMGs with d_c of 2 mm; ●, BMGs with d_c of 4 mm; ■, BMGs with d_c of 6 mm; ◐, crystalline. d_c is maximum diameter at which the fully glassy rod is produced successfully [42].*

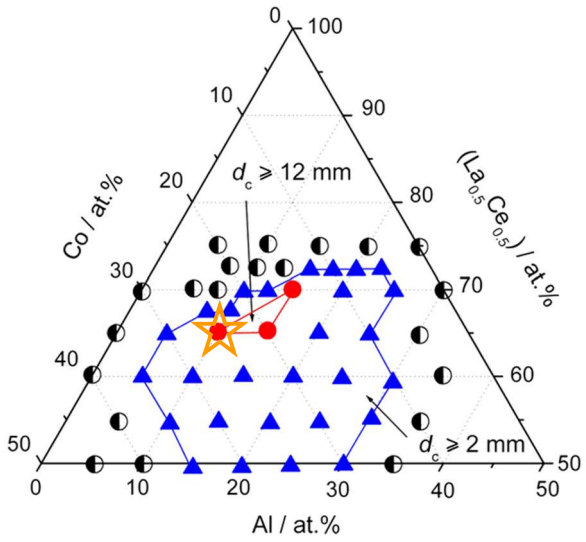

***Figure 2.15**: composition map for the glass-forming range in the ($La_{0.5}Ce_{0.5}$)-Al-Co. The symbols represent: ▲, BMGs with d_c of at least 2 mm; ●, BMGs with dc of at least 12 mm; ◐, crystalline [42].*

In figure 2.14 and 2.15, ternary diagrams are presented, highlighting the compositions with which it is possible to obtain BMG and the sizes achieved. Larger sizes are associated with a higher GFA. The stars shown on the graphs indicate compositions $Ce_{65}Al_{10}Co_{25}$,

$La_{65}Al_{10}Co_{25}$ and $(Ce_{0.5}La_{0.5})_{65}Al_{10}Co_{25}$, which are among those to be analysed in Chapter 4 of this work.

The properties of these metallic glasses will be intermediate between those of Ce-based and La-based metallic glasses, depending on their relative content. Differently from others metallic glasses, that are usually brittle, among the most interesting properties of this class of metallic glasses is their polymer-like thermoplastic behaviour, achievable at low temperatures (starting around 360 K), which can be useful for the creation of microstructures: it is possible to obtain even nanometric structures while saving energy and achieving precision, as the lack of crystallinity reduces the tendency for solidification shrinkage. This behaviour is due to their glass transition temperature, which is lower compared to other metallic glasses. This is because of the weak bonds they form - allowing the atoms to reorganize themselves under mechanical stress at lower temperatures - and their electronic configurations that influence their ability to form a stable amorphous network with a low softening point. The advantages in terms of production methods are therefore similar to those of polymers, but the different bonding nature allows metallic glasses to achieve high strength and good electrical conductivity.

3 Experimental process

In this chapter the experimental process will be covered, from the production of samples to their analysis and processing of the collected data. The analyses described in this chapter were carried out at the Universitat Politécnica de Catalunya.

3.1 Sample preparation

In this work all the analysed samples were in form of ribbon produced by single wheel melt spinning technique (Figure 3.1). In this technique, already mentioned in chapter 2 the alloy is inductively melted and dropped on the surface of a rotating wheel that is cooled internally by water. The heat of the molten liquid is absorbed rapidly, allowing cooling rates in the order of 10^4-10^7 K/s, which is high enough to avoid the crystallization [43].

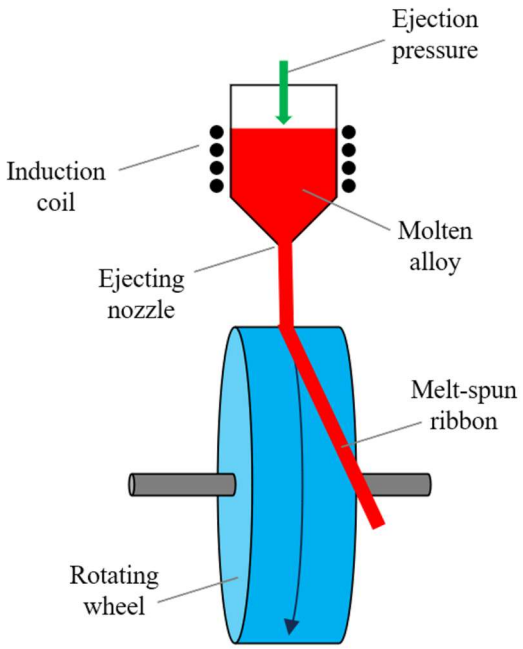

***Figure 3.1**: single wheel melt spinning technique*

In the compositions under investigation the atomic percentage of Al and Co are the same in all systems (respectively 10% and 25%); the remaining 65% is composed by Ce and La in different percentages (0-100, 30-70, 40-60, 50-50, 60-40, 70-30, 100-0).

3.2 Differential Scanning Calorimetry (DSC)

The DSC is a thermal analysis technique which plays a significant role in the research and development of materials. The results presented in the next chapter were collected using a heat flux DSC. In heat flux DSC two pans, one with the sample inside and one empty reference pan, are heated in a furnace in which there are two temperature sensors on whom the two pans are placed. When the furnace is heated, both the sample and the reference will initially heat at the same rate, so there will be no temperature differences between the two pans [44]. During the heating, if in the sample occur endothermic (or exothermic) processes it will absorb (or release) heat and its temperature will fall behind (or exceed) the temperature of the reference. Therefore, in case of endothermic process the difference ΔT between the sample and the reference temperatures will be negative, while in case of exothermic process it will be positive. By measuring ΔT it is possible to determine the heat flow dq/dt, being proportional to each other according to the relationship

$$\frac{\mathrm{d}q}{\mathrm{d}t} = k\Delta T$$

where k is an experimentally determined cell constant [44]. This analysis results in a heat flow curve, that is a representation of the difference in heat flow between the sample and the reference as a function of temperature while their temperature varied at a constant rate [45]. The heat flux DSC setup is shown in figure 3.2.

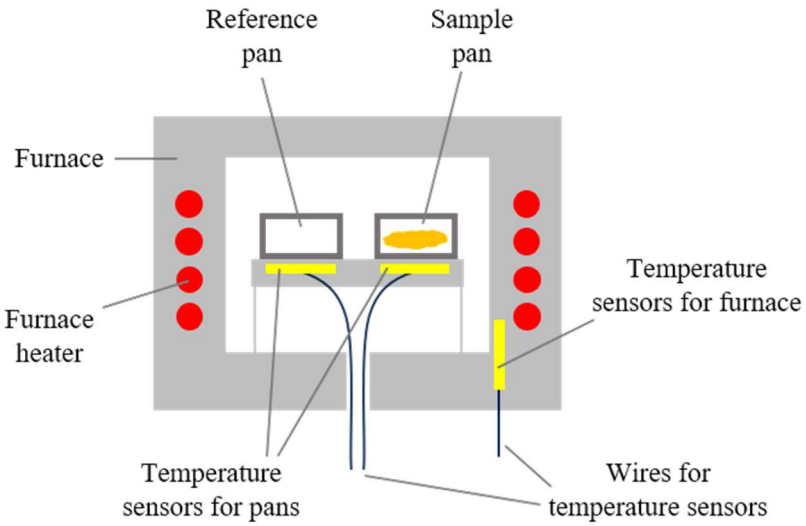

***Figure 3.2**: heat flux DSC scheme*

The heat flow curves presented in the following chapter were obtained by heating the sample from 25ºC to 400ºC with a heating rate of 5 K/min. To have more results to compare, the DSC was also performed using a heating rate of 1 K/min and 20 K/min.

3.3 X-Rays Diffraction (XRD)

The XRD is an analytical technique that is based on the interactions between an incident X-rays beam and the sample to obtain information relating to its internal structure. In this work all the produced samples were analysed by XRD; in particular, for each sample Small-Angle X-Rays Scattering (SAXS) and Wide-Angle X-Rays Scattering (WAXS) analysis were performed simultaneously during annealing from 25-30ºC to 400ºC, in order to study the structural changes during the heat treatment.

3.3.1 Experimental setup

The XRD setup is reported in figure 3.3: first, the X-ray beam is generated by a source and collimated to uniform it. Once collimated it irradiates the sample and interacts with it. There are various possible interactions between the beam and the sample, but for this analysis the only one of interest is the elastic scattering. The signal produced by the X-rays scattered by the electrons will have different intensities in different directions, the angle of which depends on the structure of the sample. By detecting this signal, is therefore possible to obtain information relating to the structure of the material [46]. This was a brief introduction about

the steps from the X-rays beam generation to the detected signal; the theoretical principal underlying this technique (explained in the following paragraph) allow us to better understand how the interaction between the incident beam and the sample can give information about the structure of the material.

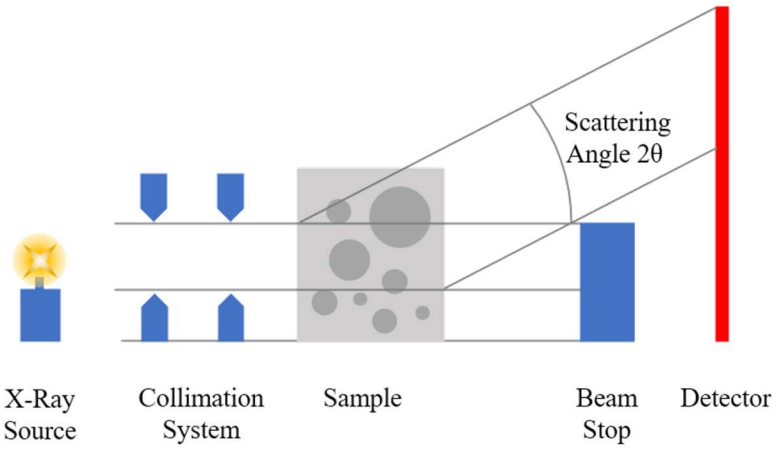

***Figure 3.3**: XRD experimental setup scheme*

3.3.2 Theoretical principles

X-rays interacts with matter in three main ways as they can be elastically scattered, inelastically scattered or absorbed. As already mentioned, the XRD analysis is based on elastic scattering phenomena, which are here described.

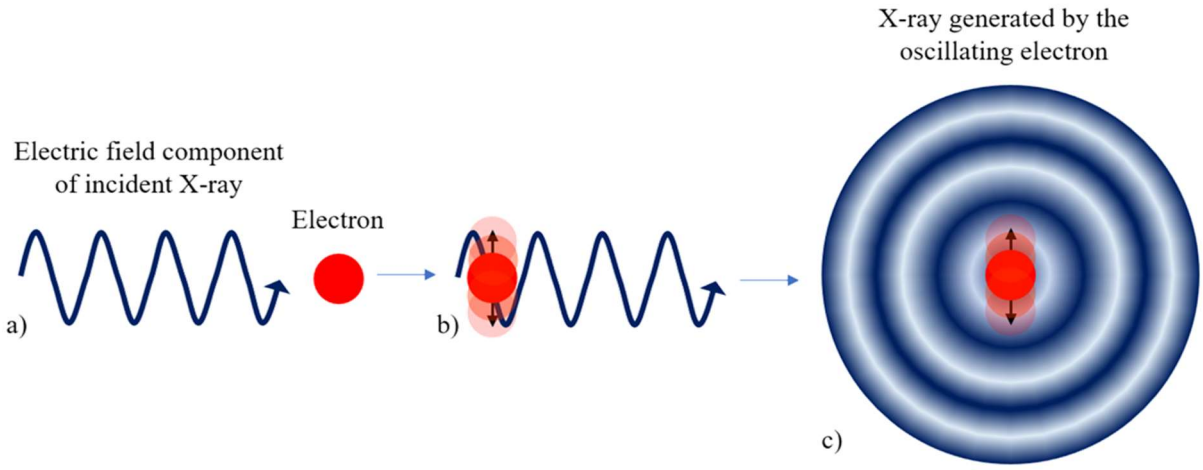

***Figure 3.4**: elastic scattering scheme. a) X-ray and electron before interacting. b) electron oscillation due to the electric field component of the radiation. c) the accelerated electron emits an X-ray in 3D space*

Considering a single electron (Figure 3.4a) interacting with an X-ray, this, being charge, will oscillate (up and down) due to the electric field component of the radiation at a frequency that is the same as the incident X-ray (Figure 3.4b). Because of the X-ray, the electron is therefore an accelerated charged particle, and so it will emit electromagnetic radiation with a frequency equal to that of its oscillation (equal, as already said, to the incident X-ray frequency). The electron then becomes a source by emitting in all directions a radiation equal to that of the incident X-ray (Figure 3.4c) [46].

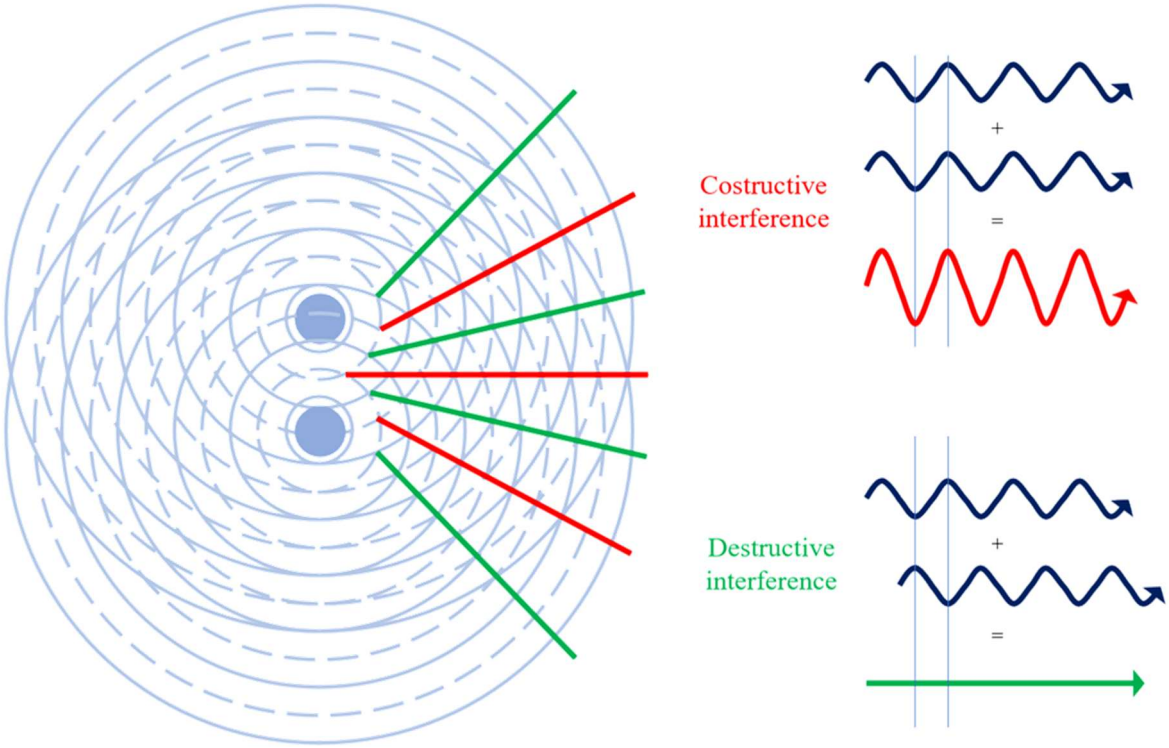

***Figure 3.5**: constructive and destructive interference. The dotted circles correspond to troughs, while the solid ones correspond to the crests of the waves.*

Within a material, all electrons will behave in the way just described, and the X-rays emitted by them will interfere each other. Consider several electromagnetic waves emitted, they interfere in the various directions in a destructive or a constructive way: the interference is constructive if the waves are in phase, which means that the crests are aligned with the crests and the trough are aligned with the trough; in the directions in which the interference is constructive the sum of the two waves results in a wave with the same frequency of them and an amplitude equal to the sum of the two amplitudes. The interference is destructive in the directions in which crests and trough are aligned, resulting in a wave with amplitude

zero. In figure 3.5 these interactions are shown for the simple case of two electrons, while in a scattering experiment the intensity collected by the detector corresponds to the contribution of all the electrons in the illuminated volume of the sample.

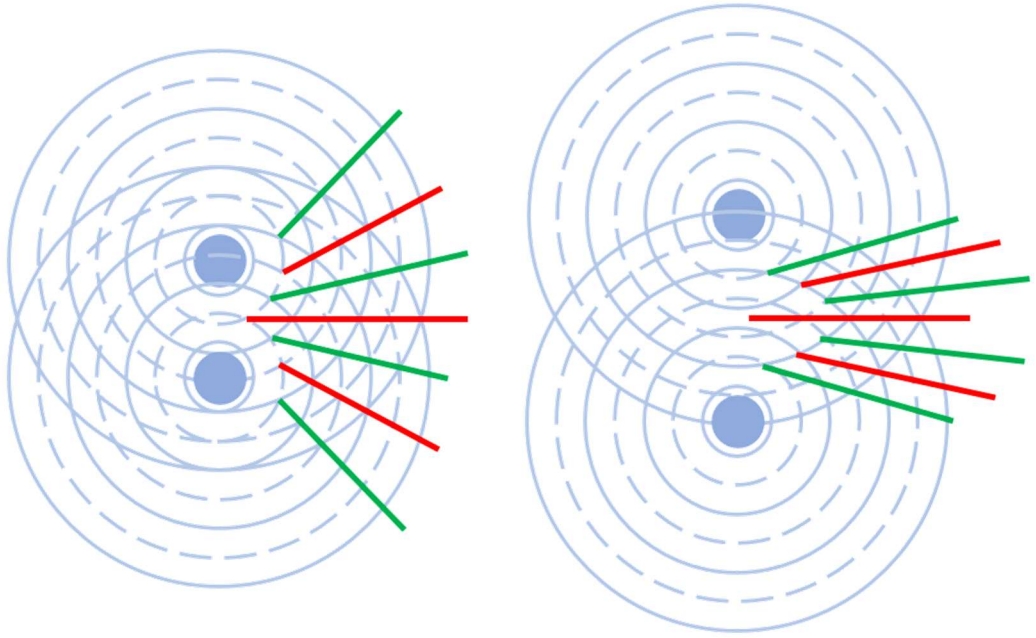

***Figure 3.6**: constructive (red) and destructive (green) directions depending on the electron distance*

By observing figure 3.6 it is evident that the directions in which the interference is constructive or destructive depends by the positions of the electrons that being the latter around the atomic nuclei are related to the positions of the atoms in the material.

The correlation between these directions and the atomic distance is given by the Bragg's law:

$$2d \sin \theta = n\lambda$$

where d is the distance between atoms, λ is the wavelength of the X-ray and n is any integer. The angles θ at which this law is satisfied correspond to maximum in intensity [47]. From figure 3.7 it is possible to better understand a more concrete meaning of this law: considering a crystalline structure the X-rays scattered by two atoms will interact in a constructive way if they are in phase. This happens only if the difference in their path is equal to an integer multiple of the wavelength. The Bragg's Law can be obtained by simple geometrical considerations.

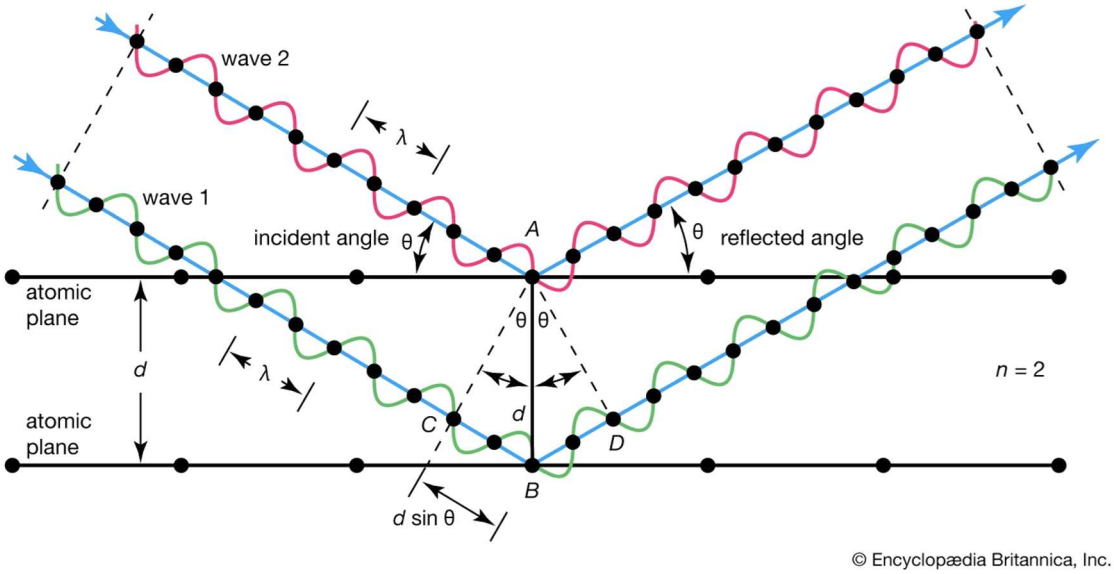

***Figure 3.7**: Scheme to better understand the Bragg's law*

As in crystalline materials the distances between the atoms are regular and equal in all the material, these angles will be well defined, while in an amorphous material, in which the distances between the atoms varies in a range of values (as the atomic positions are random but still with a certain degree of packing), these maximum intensities do not correspond to precise angles. Figure 3.8 represents the XRD spectra for a crystalline and an amorphous material. Looking at the Bragg's law (and at figure 3.6) it is evident that smaller angles correspond to higher atomic distances.

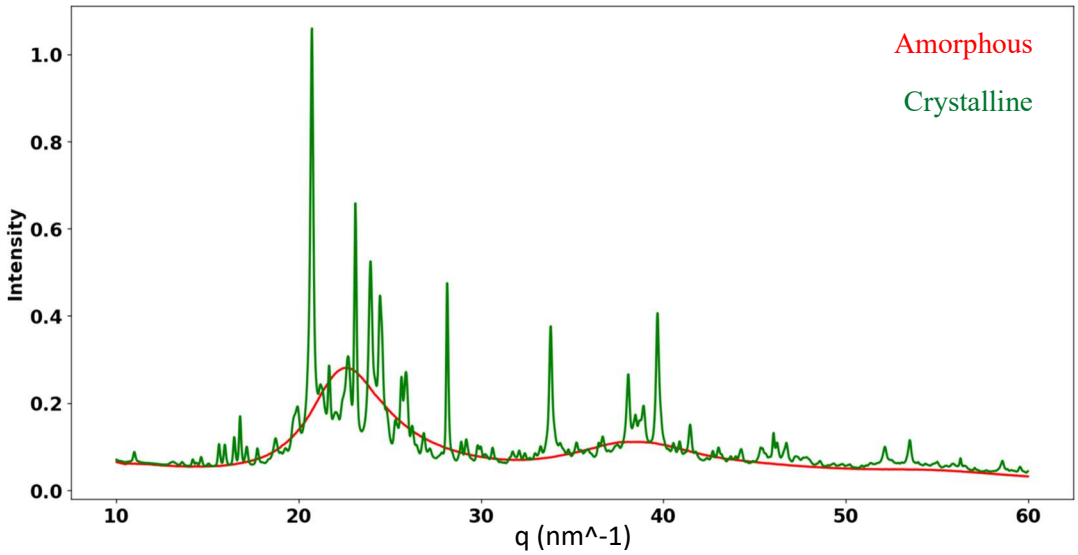

***Figure 3.8**: XRD spectra for a crystalline (green) and an amorphous (red) material ($(Ce_{0.7}La_{0.3})_{65}Al_{10}Co_{25}$)*

To make the XRD results independent from the wavelength, in the spectra used in this work the intensity will not be reported as a function of the angle 2θ but as a function of the momentum transfer q defined according to the expression

$$q = \frac{4\pi}{\lambda} \cdot \sin\theta \qquad [1/nm]$$

by which it is evident that an increasing in q corresponds to an increasing in θ [46].

3.3.3 WAXS and SAXS

Small-Angle X-Rays Scattering and Wide-Angle X-Rays Scattering differ, as suggested by the name, by the range of angles on which the signal is detected. In table 3.2 the main differences between these two analyses in terms of angle, scale and applications are reported.

	SAXS	WAXS
Scattering angle	$0 < 2\theta < 5$	$5 < 2\theta < 60$
Scale	Structure and morphology of materials on a nanometric scale.	Atomic and molecular structure on an Angstrom scale.
Applications	To study non-homogeneous systems with particle sizes ranging from few to hundreds of Angstroms.	To study crystalline (periodic) structures or the SRO and MRO of liquids and amorphous samples

***Table 3.2**: main differences between SAXS and WAXS*

The experiment was performed in the NCD-SWEET beamline of the ALBA synchrotron, which uses a Pilatus3 S1M detector for SAXS and a Rayonix LX255-HS detector for WAXS [47].

3.3.4 Data processing

The result of an XRD (SAXS or WAXS) analysis is a 2D map of the detector in which at every point is associated the detected intensity. The resulting image for SAXS and WAXS,

need to be converted to obtain the plot of the intensity as a function of q. To perform this conversion the images were first masked and then integrated using the PyFAI software [48]. These steps are schematized in figure 3.9.

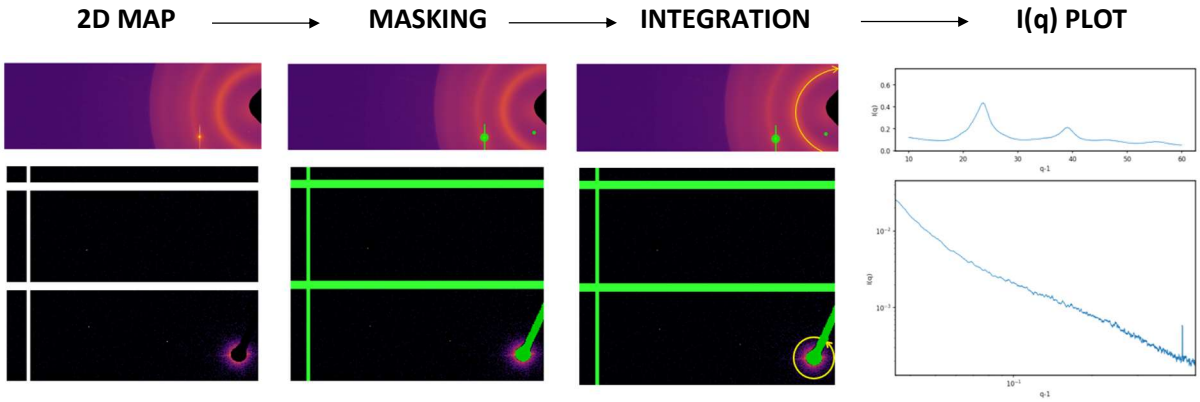

***Figure 3.9**: Data processing steps for WAXS (above) and SAXS (below) analysis*

The masking phase consists in covering points and areas of the images in which there are obvious errors in the signal due to impurities present on the window of the sample stage and to the beam stop shadow. The clean images obtained are then integrated to obtain the I(q) values.

3.3.5 Temperature correction

Due to the large size of the measuring chamber in SAXS and WAXS the set temperatures do not represent the actual temperature of the studied systems. This difference between the real temperature and the set temperature, which is not the same for the various compositions and at the various temperature, complicates the comparison between DSC and XRD. To solve this problem the temperature of the DSC was considered as the correct one (as the DSC equipment was properly calibrated using standard materials) and the temperature of the XRD was shifted using the DSC as a reference. To do this adaptation for every composition two temperatures were selected in XRD. The first temperature T_{AXRD} was the one at which the WAXS plot starts to change (at relatively low temperatures), while the second one was a temperature T_{BXRD} at which there was a clear crystallization in the WAXS signal. T_{AXRD} was considered to correspond to the first major peak in DSC with onset at T_{ADSC}, while T_{BXRD} was associated to the peak that in DSC was due to the crystallization process with onset in T_{BDSC}. In table 3.3 are reported the differences between these T_{XRD} and the T_{DSC} (in A and B) that were believed to correspond to the same process.

	T_{AXRD}	$\Delta T_A = T_{AXRD} - T_{ADSC}$	T_{BXRD}	$\Delta T_B = T_{BXRD} - T_{BDSC}$
Ce0La100	186	14	290	28
Ce30La70	197	15	290	30
Ce40La60	196	15	370	37
Ce50La50	175	12	335	36
Ce60La40	167	14	325	31
Ce70La30	164	14	316	31
Ce100La0	141	12	248	19

***Table 3.3**: differences between DSC and XRD temperatures in A and in B*

The values ΔT_A and ΔT_B were subtracted respectively from T_{AXRD} and T_{BXRD} obtaining a correspondence between the temperatures in XRD and in DSC at these two points. To have a good correspondence at every temperature it was assumed a linear trend in this difference of temperatures. By comparing the XRD results corrected this way and the DSC it was observe a reasonable matching between the changes in WAXS and the peaks of the heat flow curve. It can be observed in the table that the difference between the set temperature and the real temperature increases at higher temperatures, indicating that the control of the temperature in the sample stage was progressively worsening with increasing temperature.

The XRD temperatures reported in this work will be corrected according to the method described above.

3.4 Focused Ion Beam Scanning Electron Microscopy

In Focused Ion Beam Scanning Electron Microscopy (FIBSEM) a nearly flat surface is milled in the sample using a focused ion beam (usually Ga^+) and then this surface is observed using a scanning electron microscopy [49]. The present images were collected using a ZEISS NEON 40 Crossbeam workstation with a CANION31 Gallium FIB column, a GEMINI SEM column with (Shottky-FE) gun and an INCAPentaFETx3 EDS detector for micro-elemental analysis. A photo of the used instrument is shown in figure 3.10. In the following paragraphs the functionality of this instrument will be presented.

***Figure 3.10**: ZEISS NEON 40 Crossbeam workstation*

3.4.1 Focused Ion Beam

In the ion column the ion beam of Ga^+ is generated by a liquid metal ion source (LMIS) and then it is accelerated down the column applying a potential. The beam size and shape are controlled thanks to a system of electrostatic lenses and apertures until reaching the specimen, the atoms of which can be removed if the ions energy is high enough. For this work the ion beam was used to cross-section the specimen (figure 3.11): first, a protective layer of platinum is deposited on the surface, in correspondence of the position where the transversal section will be obtained. To deposit this layer a platinum-rich precursor is introduced in the chamber by the Gas Injection System (GIS) and the molecules are then cracked with either the ion beam or the electron beam; the non-volatile product, rich in platinum, is adsorbed onto the sample and forms the deposited layer. After this deposition the cross-section (evidenced in red in figure 3.11a) is cut with the ion beam, using a smaller ion beam current in the finishing phase to polish the surface.

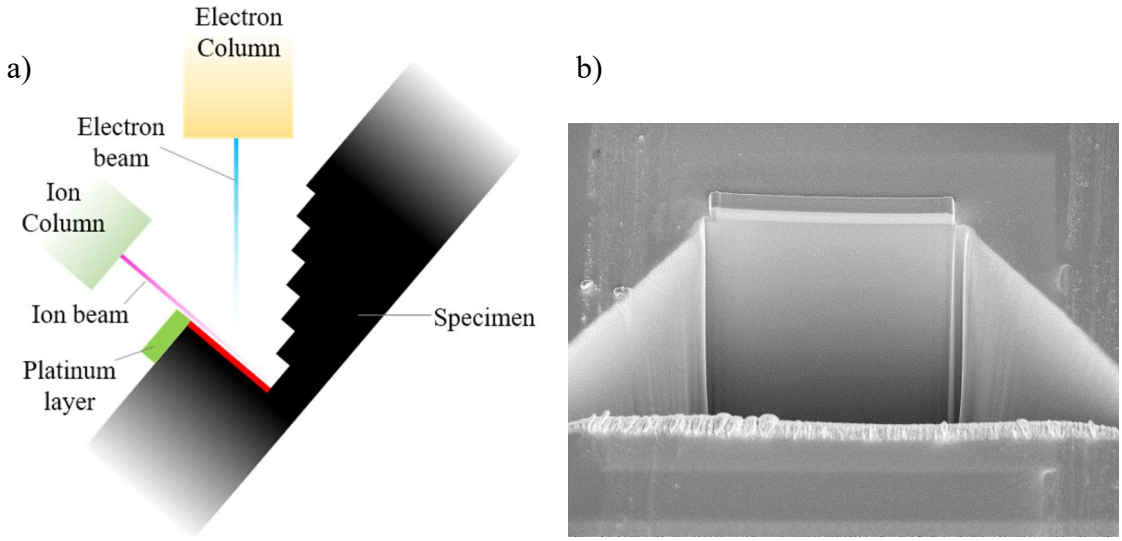

***Figure 3.11**: scheme of FIB and SEM image of the cross-sectioned sample of* $(Ce_{0.7}La_{0.3})_{65}Al_{10}Co_{25}$

3.4.2 Scanning Electron Microscopy

The obtained cross-sections were then observed using the scanning electron microscopy: in the electron column, similarly to the ion column, there is an electron source from which an electron beam is generated and focused onto the surface of the sample; here the electrons interact with the atoms of the sample producing various signals that are detected and used to create detailed images of the surface. The signals can be secondary electrons (SE) or backscattered electrons (BSE): secondary electrons are low energy electrons ejected from the surface of the sample and give information about the surface topography, while backscattered electrons are electrons of the beam that are scattered back from the sample and give information about the composition of the sample. During our analysis, also Energy Dispersive Spectroscopy (EDS) was used in combination with SEM to detect composition fluctuations within the samples. This technique is based on the detection of X-rays emitted by atoms when struck by electron beam, which, since each element has unique X-ray emission spectrum, allows for the determination of the local composition of the specimen.

4 Results and discussion

In Table 4.1 are summarized the compositions under investigation and the label that will be used in this document to refer to them. As told, the molar percentages of Al and Co are the same in all systems (respectively 10% and 25%); the remaining 65% is composed by Ce and La in different percentages.

$La_{65}Al_{10}Co_{25}$	Ce0La100	x = 0
$[Ce_{0.3}La_{0.7}]_{65}Al_{10}Co_{25}$	Ce30La70	x = 30
$[Ce_{0.4}La_{0.6}]_{65}Al_{10}Co_{25}$	Ce40La60	x = 40
$[Ce_{0.5}La_{0.5}]_{65}Al_{10}Co_{25}$	Ce50La50	x = 50
$[Ce_{0.6}La_{0.4}]_{65}Al_{10}Co_{25}$	Ce60La40	x = 60
$[Ce_{0.7}La_{0.3}]_{65}Al_{10}Co_{25}$	Ce70La30	x = 70
$Ce_{65}Al_{10}Co_{25}$	Ce100La0	x = 100

***Table 4.1**: Studied compositions and reference name*

In this chapter, the transformations of compositions Ce0La100, Ce30La70, Ce70La30 and Ce100La0 will be analysed in more detail. Finally, a comparison between all the compositions will be made. Ce50La50, Ce60La40 and Ce40La60 will only be considered in this final phase of comparison since the results obtained for these are in agreement with those obtained for the other compositions.

4.1 Ce0La100

The DSC signal of Ce0La100 is shown in figure 4.1. Considering the plot, increasing the temperature from 30ºC to 375ºC, a first shallow exothermic peak appears at T_r~115ºC. This signal is typical of a structural relaxation of the glass. This relaxation phenomena ends with the glass transition which occurs at T_g~160ºC: the glass phase transforms to a supercooled

liquid. Following the glass transition, another exothermic phenomenon begins at T_1~170ºC. After that there are three partially overlapping exothermic peaks, the first of which begins at around T_2=250ºC.

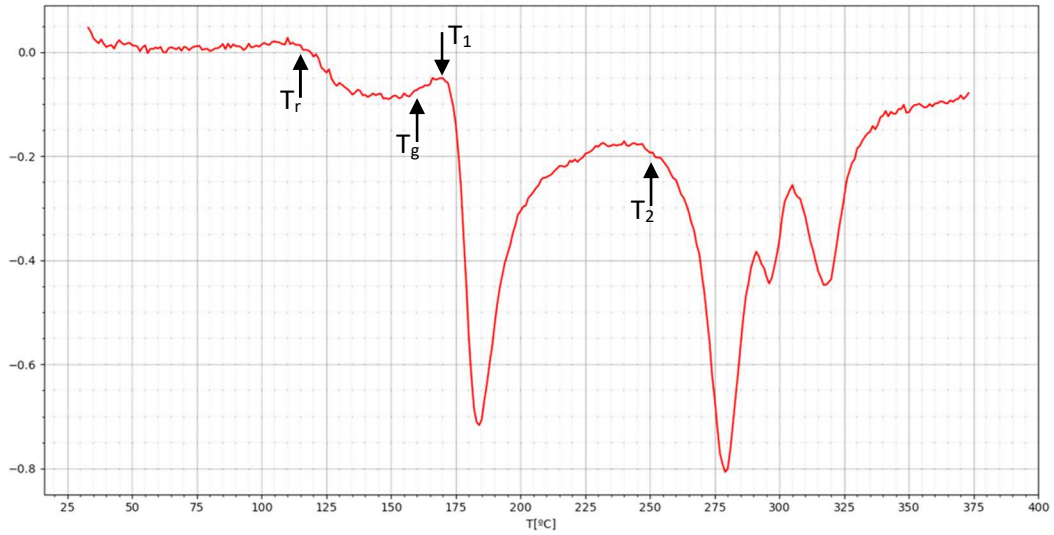

Figure 4.1: *DSC plot for Ce0La100 heated at 5 K/min until 375ºC*

4.1.1 Relaxation

Figure 4.2 shows the SAXS and WAXS signals of the as-prepared sample and the sample at the end of the relaxation peak.

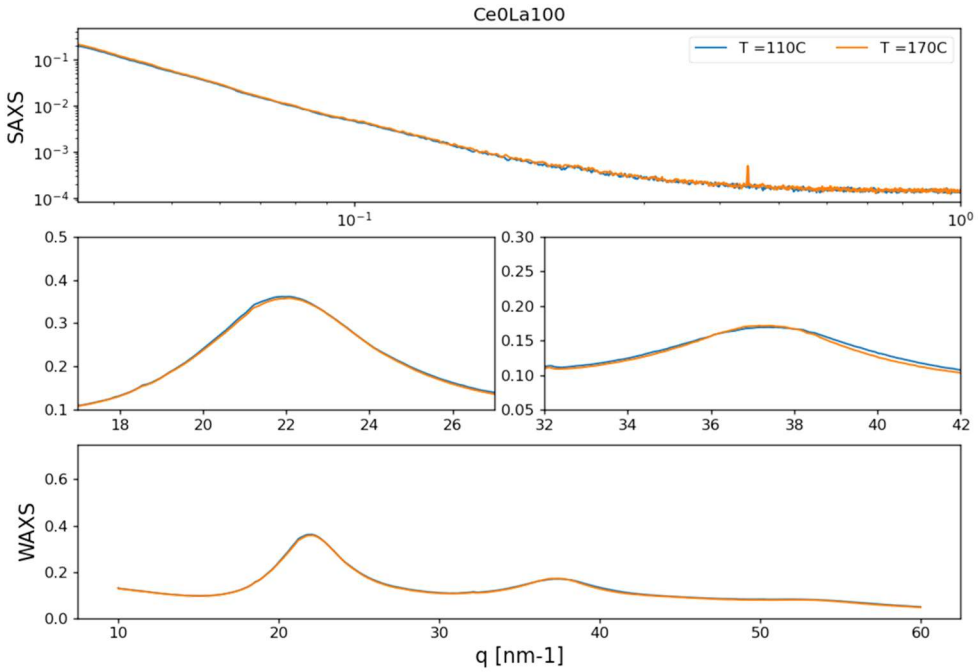

Figure 4.2*: SAXS (top) and WAXS (bottom) intensity patterns for Ce0La100 heated at 5 K/min at 110ºC (onset of the relaxation) and at 170ºC (offset of the relaxation). The two middle plots are magnifications of the sharp amorphous peaks in WAXS.*

As can be seen, the changes in the WAXS and SAXS signals are minimal. This result was expected because during relaxation the atomic displacement is so limited that they are not visible with XRD [33]. Only a really small shift of the first peak, towards higher q values (i.e. smaller lengths), can be observed. This shift agrees with the expected densification of glasses during structural relazation.

4.1.2 From 170ºC to 225ºC

Focusing on the first DSC peak after the glass transition, some considerations can be made regarding the fact that plotting the WAXS and SAXS signals from the beginning of the peak (170ºC) to a temperature where the transformation is evidently complete (200ºC) shows one type of change, while the signal after this peak shows more significant changes despite the transformation appearing nearly complete based on the DSC comparison. This can be observed in figure 4.3 and 4.4.

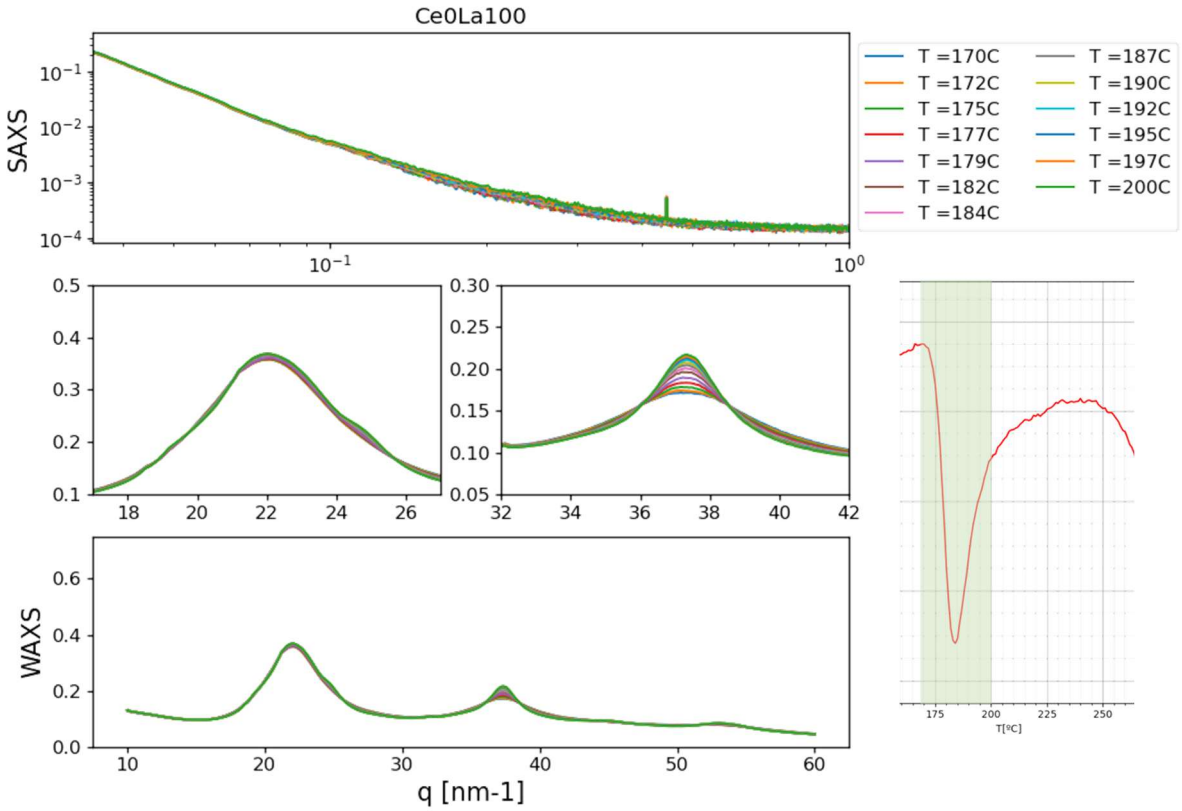

***Figure 4.3**: SAXS (top) and WAXS (bottom) intensity patterns for Ce0La100 heated at 5 K/min from 170ºC to 200ºC. The two middle plots are magnifications of the sharp amorphous peaks in WAXS.(inset) correspondent temperature range in DSC plot.*

Figure 4.3 shows the SAXS and WAXS signals between 170ºC and 200ºC. In this temperature range, there is a small difference in the SAXS and a variation in the WAXS mainly affecting the second peak in terms of intensity and width. The narrowing of the WAXS peak indicates changes in terms of order affecting short range distances within the structure. By applying Bragg's law with n=1, it is possible to interpret the peak at q=37.5 nm^{-1} as a more ordered packing at distances of 0.168 nm, maintaining an amorphous structure, so this first process could be an amorphous transition between two amorphous states with different SRO and MRO.

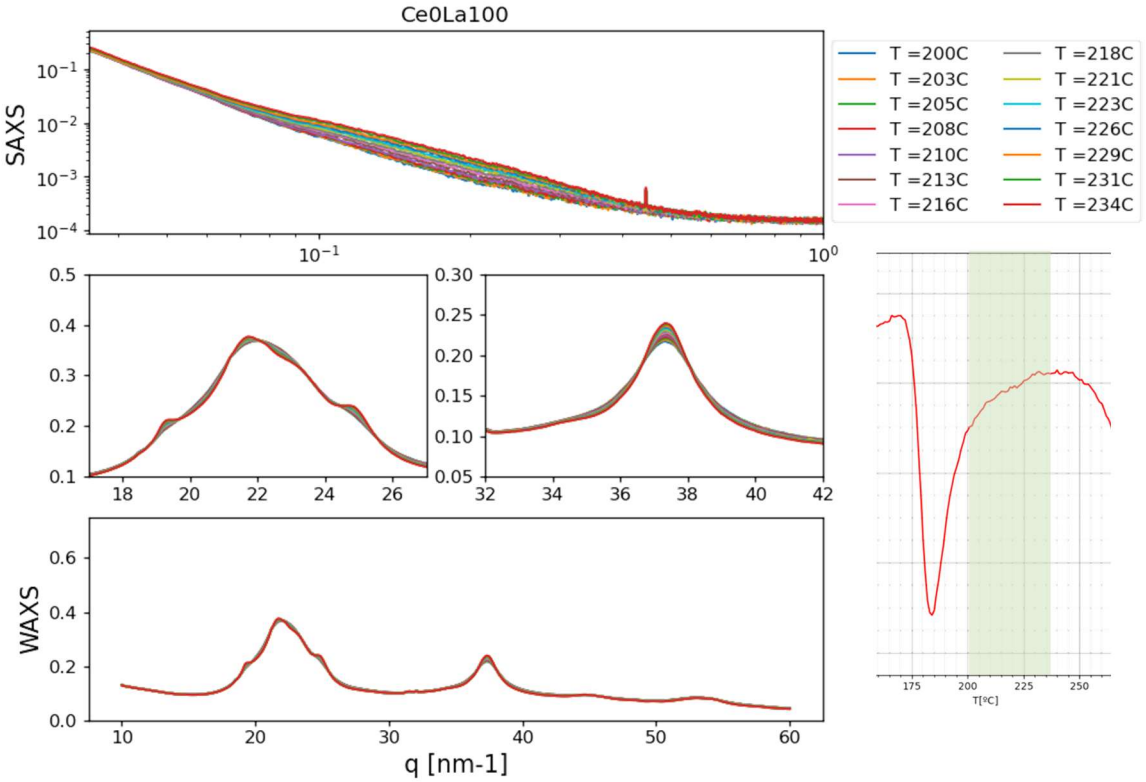

***Figure 4.4**: SAXS (top) and WAXS (bottom) intensity patterns for Ce0La100 heated at 5 K/min from 200ºC to 235ºC. The two middle plots are magnifications of the sharp amorphous peaks in WAXS. Inset: correspondent temperature range in DSC plot.*

Figure 4.4 is analogous to the previous one but between 200ºC and 235ºC. In this case, there are more significant changes in the SAXS and a sort of undulation of the first WAXS peak. A possible explanation for such different changes in WAXS/SAXS corresponding to the DSC peak and when it is concluding could be the presence of two partially overlapping peaks in the DSC or some inaccuracies in the temperature correction of the XRD to adapt its results to the DSC.

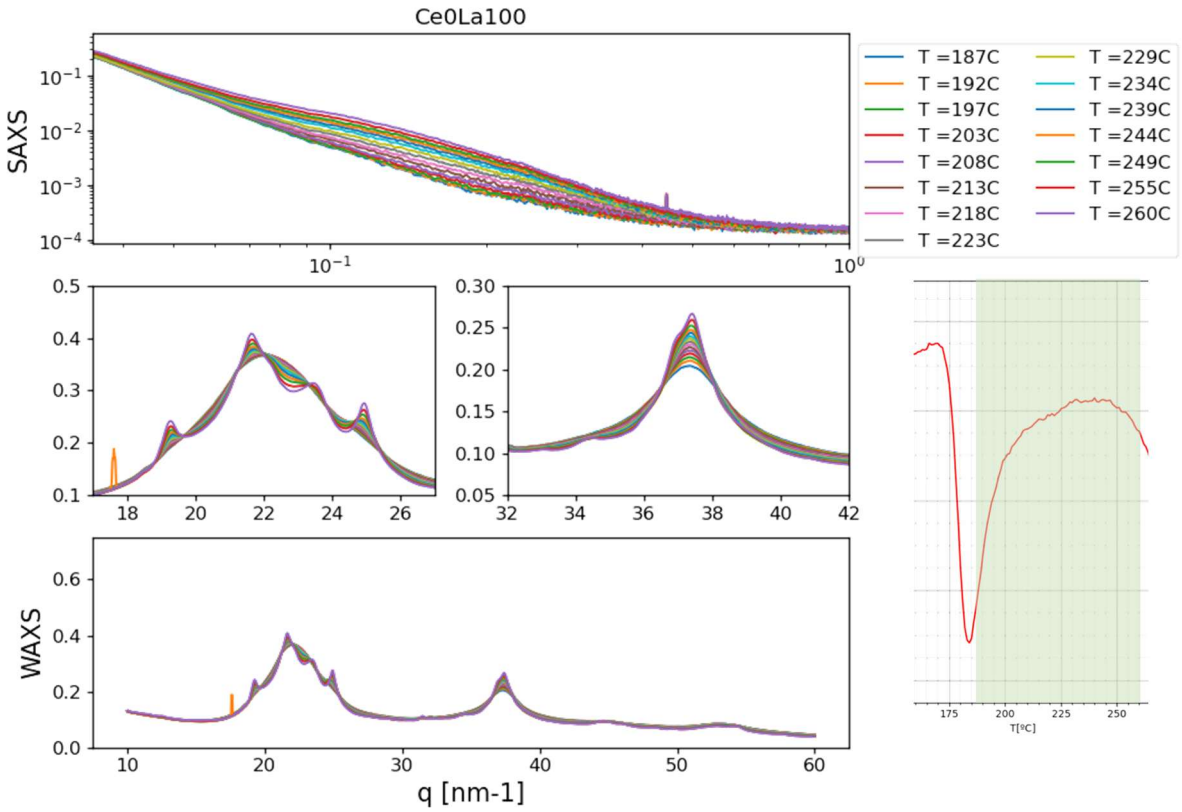

***Figure 4.5**: SAXS (top) and WAXS (bottom) intensity patterns for Ce0La100 heated at 5 K/min from 187ºC to 260ºC. The two middle plots are magnifications of the sharp amorphous peaks in WAXS. Inset: correspondent temperature range in DSC plot.*

Assuming that the slight bump that forms at q=25 is associated with the second of these overlapping phenomena (a reasonable assumption since similar changes occur at other q values between 200ºC and 235ºC), the onset temperature of the second phenomenon was estimated by magnifying on this particular region of the WAXS and the temperature turned out to be ~185ºC. These changes occur within a temperature range from 185ºC to 260ºC, at which point the changes associated with the last DSC peaks begin. The SAXS/WAXS signal in this temperature range is shown in Figure 4.5. The WAXS signal shows broad and weak peaks overlapping with the amorphous halo; these could be associated with the formation of crystals that are too small to produce well-defined peaks. To better understand these initial transformations Ce0La100 heated up to 225ºC has been also analysed with FIBSEM. Observing Figure 4.6, one can notice the presence of heterogeneities with variable sizes up to approximately 80-90 nm; these entities are likely responsible for the increase in the SAXS signal. The image highlights an inhomogeneity in terms of sizes.

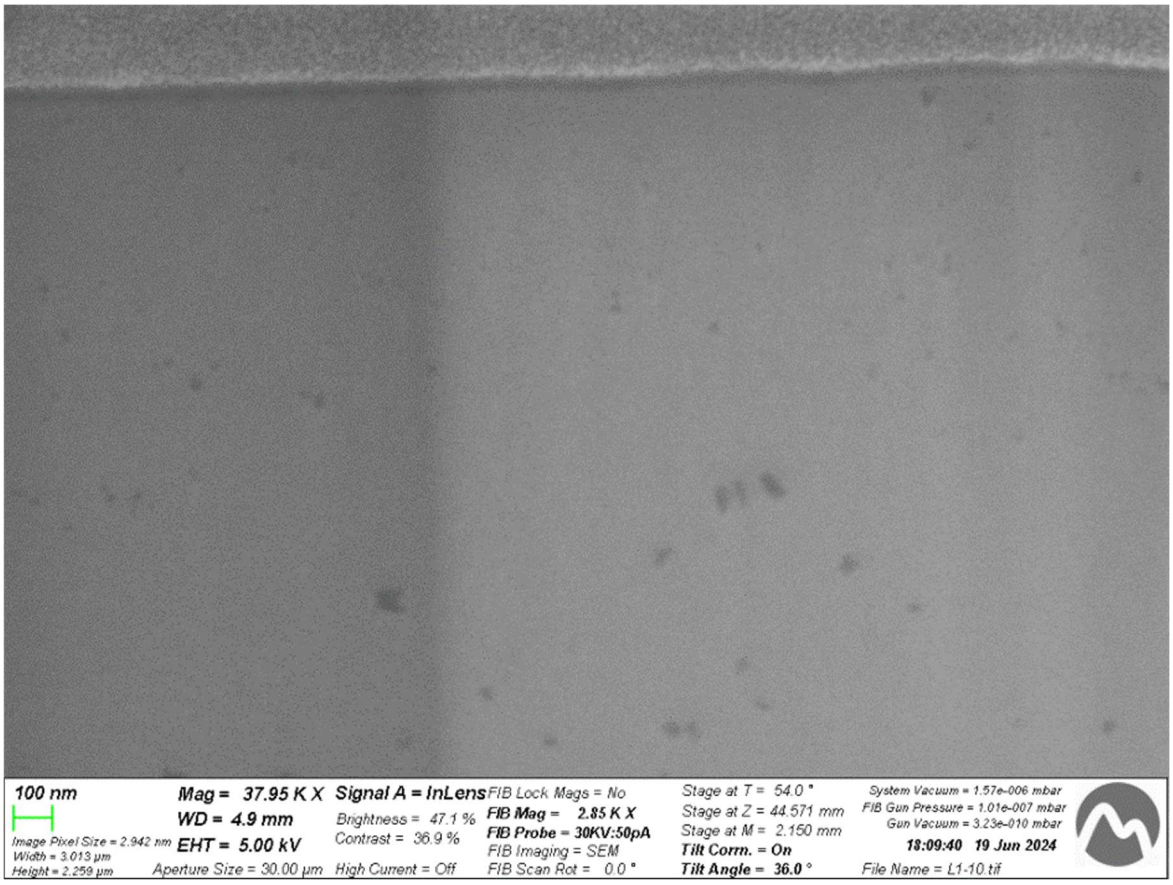

***Figure 4.6**: SEM micrograph of Ce0La100 heated to 225°C prepared using FIB. The image was acquired with the SE detector at an accelerating voltage of 5 kV. The scale bar represents 100 nm.*

Based on the images collected with FIBSEM, it seems that the spatial distribution of the particles formed is inhomogeneous. However, this could be an impression due to the fact that the particles below a certain size are not clearly visible in the image. From the SAXS signal, in fact, there appears to be a certain spatial correlation between the entities [4.2]: the changes in the SAXS signal consist of the formation of a sort of "shoulder" around a q value between 0.1 nm^{-1} and 0.2 nm^{-1}. Changes of this type can be interpreted as a weak spatial correlation between the particles. Using the relationship $d=2\pi/q$, it is calculated that these heterogeneities have an average distance ranging from 31.4 nm and 62.8 nm. The observed shoulder, therefore, indicates a certain level of spatial organization: the particles are positioned at a preferred distance, which is neither random nor follows a rigid regular order. The entities formed have a low probability of overlapping or approaching too closely. This phenomenon could be associated with a local depletion of elements: the entities depleting some specific elements from the surrounding environment, which then has a composition unsuitable for the formation of other heterogeneities.

a)

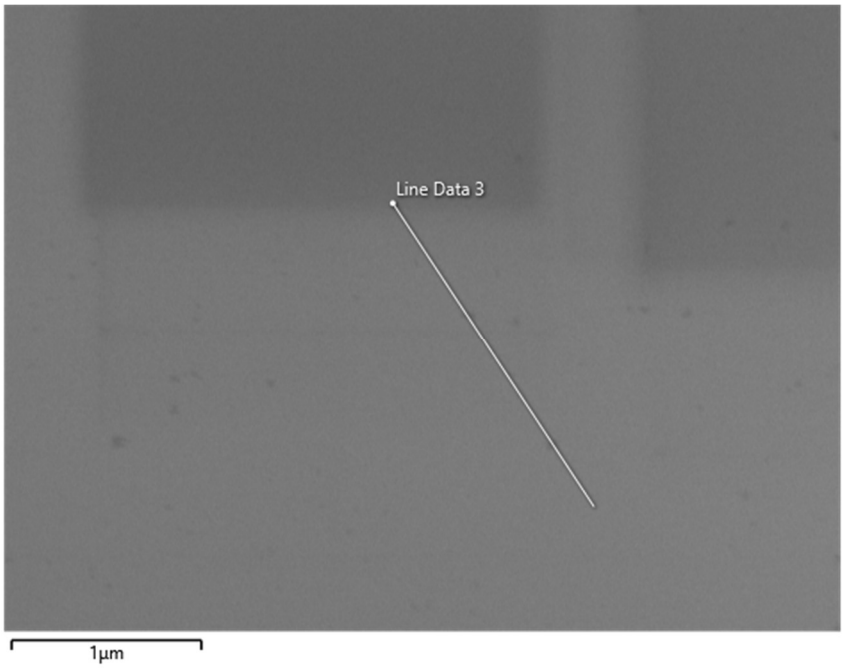

b)

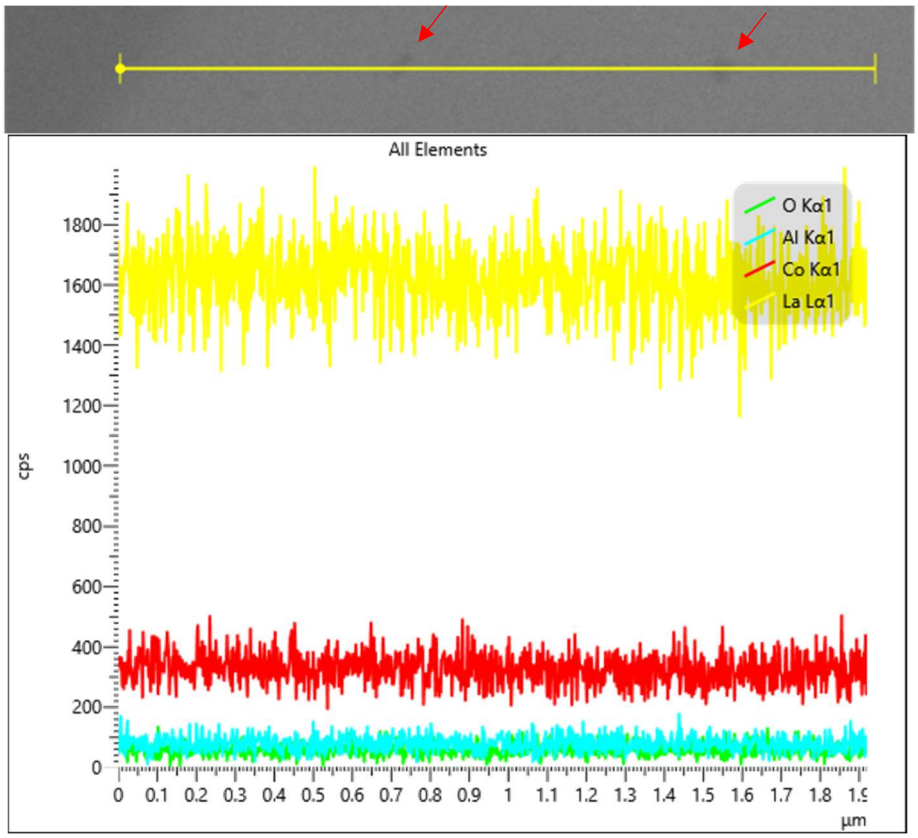

***Figure 4.7**: a) SEM micrograph of Ce0La100 prepared using FIB. The scale bar represents 1µnm.EDS analysis was performed along "Line Data 3". b) "Line Data 3" is shown horizontally (top). The content of the various elements is represented as a function of the position along line (below)*

In order to investigate the composition of these heterogeneities, an EDS analysis was performed. The elements detected along the line in Figure 4.7a are shown in Figure 4.7b; no

significant fluctuations in composition were observed in correspondence with the heterogeneities during EDS analysis. This could be attributed to the small size of heterogeneities, which might have required a longer analysis time.

4.1.3 From 250 to 350

As mentioned, between 250ºC and 350ºC the DSC shows three overlapping peaks. Changes in the WAXS signal (Figure 4.8) evidence crystallization phenomena. The SAXS signal, on the other hand, increases at increasingly lower q values due to the growing size of the crystals.

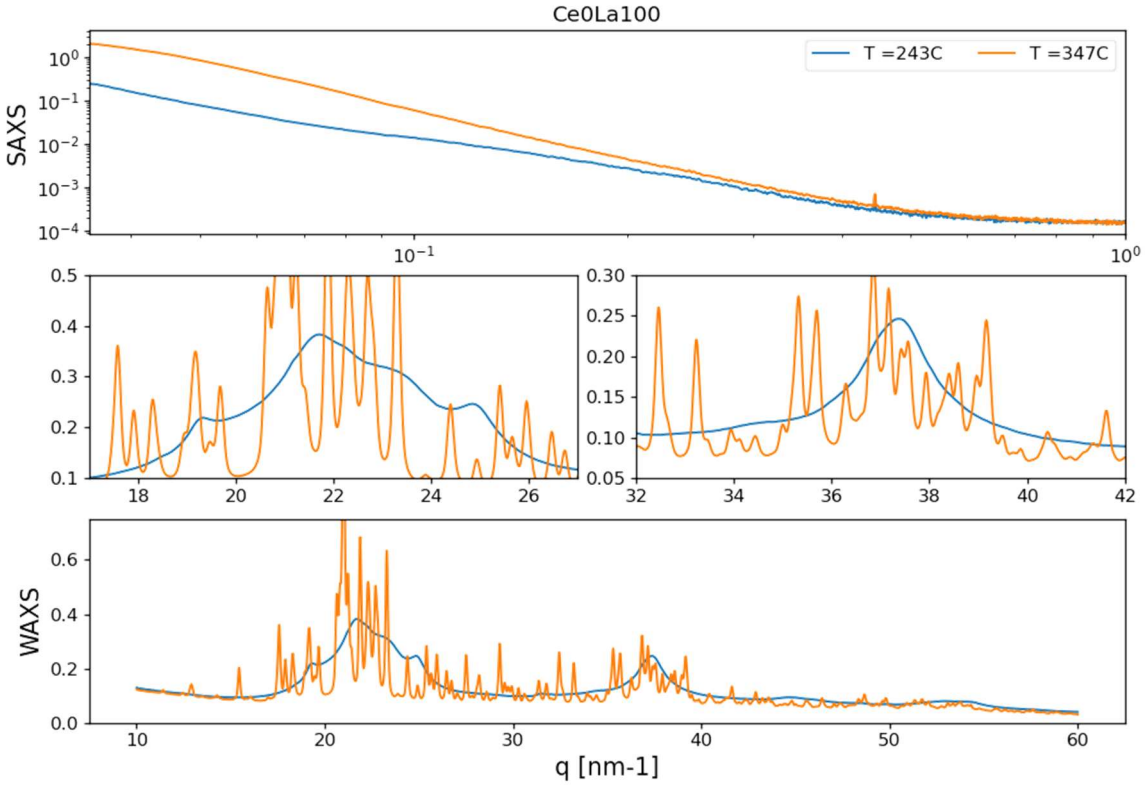

***Figure 4.8**: SAXS (top) and WAXS (bottom) intensity patterns for Ce0La100 heated at 5 K/min at 243ºC and at 347ºC. The two middle plots are magnifications of the sharp amorphous peaks in WAXS.*

A more detailed study of this temperature range attempted to examine the phenomena associated with the three DSC peaks separately. By observing the changes in the WAXS signal, the onset temperatures of the three peaks could be 264ºC, 274ºC and 285ºC. This conclusion is consistent with the fact that the three peaks in the DSC are overlapped. The first two of these three phenomena seem to be associated with the appearance of some sharp and rather narrow peaks in WAXS, which add to the amorphous halos. For the first

phenomenon, the increase in SAXS intensity is quite uniform across all q values and is also rather small. During the second phenomenon, however, the increase in SAXS signal mainly affect smaller q values. The superposition of sharp and narrow peaks on the amorphous halo suggest that the sample contains crystalline regions in an amorphous matrix. The fairly uniform but small increase in SAXS during the first DSC peak (at ~260ºC) suggests the formation of a small number of crystals or crystals with low electron density contrast relative to the starting amorphous material, distributed homogeneously throughout the sample.

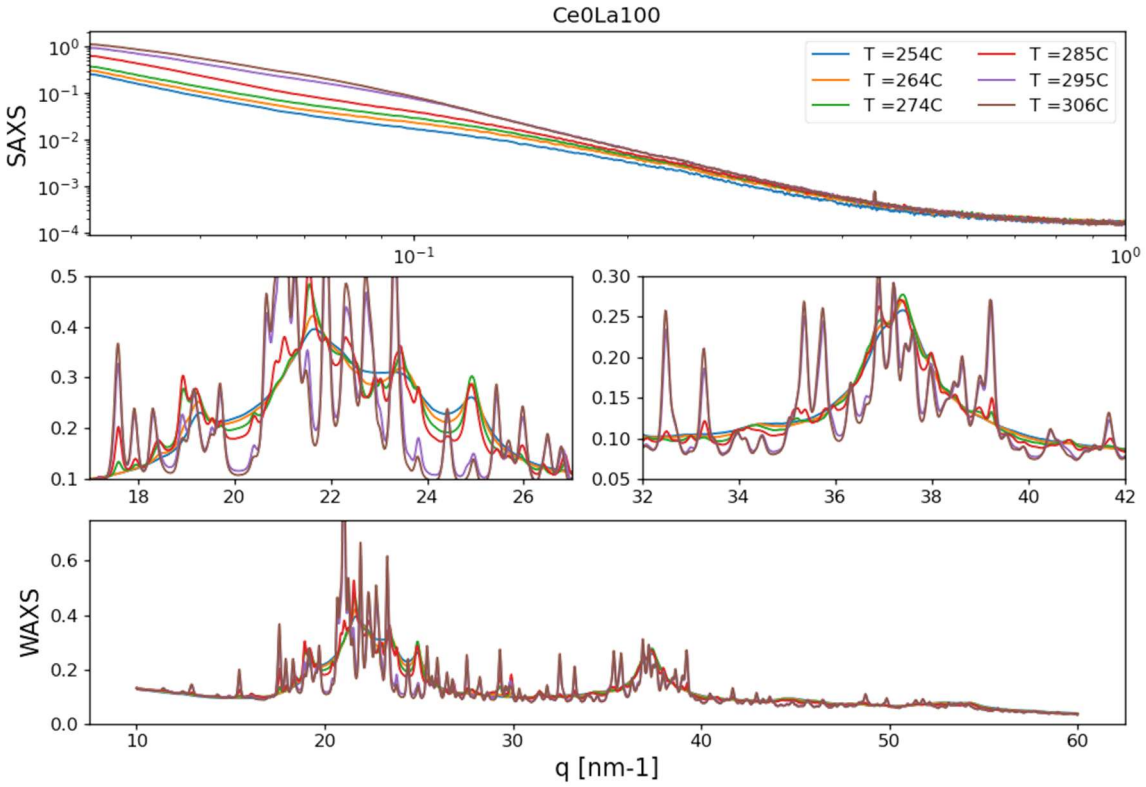

***Figure 4.9**: SAXS (top) and WAXS (bottom) intensity patterns for Ce0La100 heated at 5 K/min before (254ºC), after (295ºC and 306ºC) and at the temperatures (264ºC, 274ºC and 285ºC) thought to correspond to the onset of the three overlapping peaks in the DSC. The two middle plots are magnifications of the sharp amorphous peaks in WAXS.*

During the second phenomenon, a new crystalline phase is formed accompanied by the growth of already existing crystals, as suggested by the low q values at which an increase in the SAXS signal occurs. The last transformation that the sample undergoes is characterized by the appearance of new peaks, as in the other two cases, but also by the almost complete disappearance of the amorphous signal. The SAXS signal shows a rather evident increase at low values. Given the overlap of the phenomena, it is not easy to say exactly which DSC peak corresponds to each change in the SAXS and WAXS signals, but overall, we can say that three different crystalline phases are formed and grow until almost complete

crystallization of the sample. Furthermore, some of the WAXS peaks formed around 260ºC seem to lose intensity as the temperature increase. This could be associated with the use of atoms that constituted the crystals formed at that temperature for the formation of new crystals with different composition and structure. From Figures 4.9 and 4.10, it is possible to observe the changes described in the paragraph.

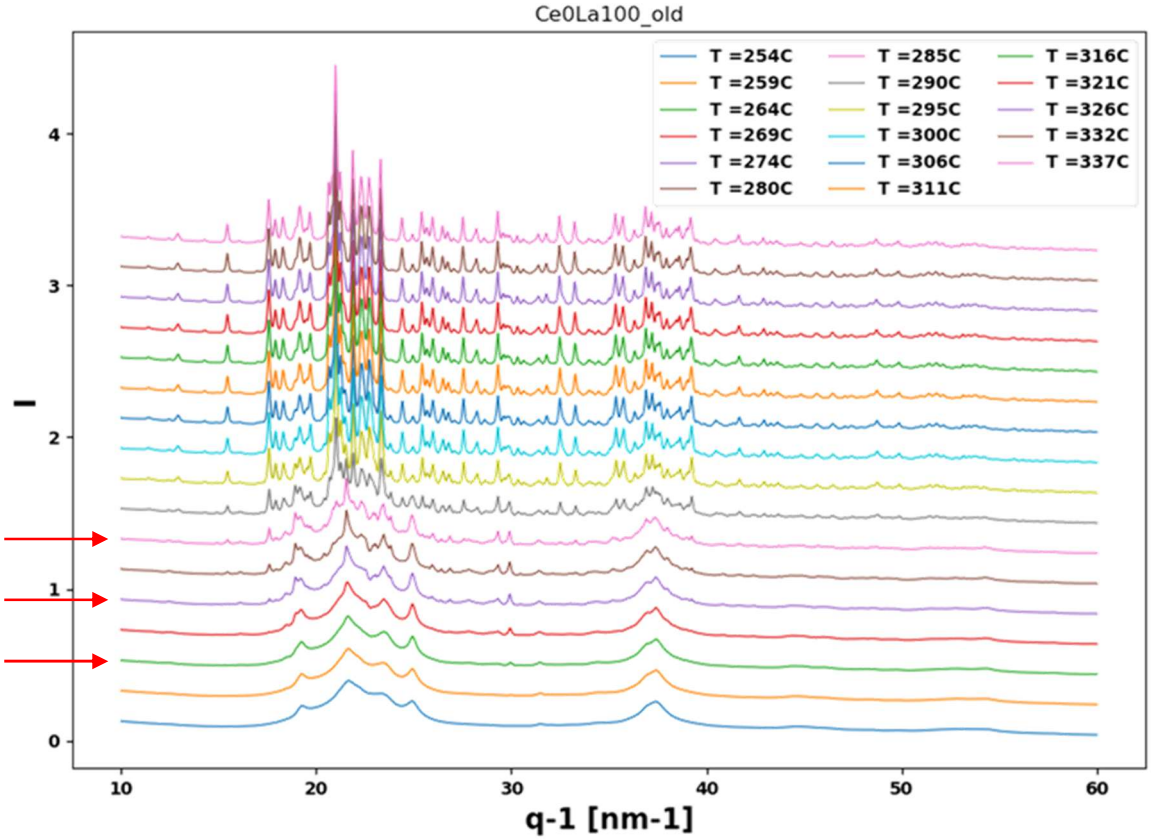

***Figure 4.10**: WAXS intensity patterns for Ce0La100 heated at 5 K/from 254ºC to 337ºC. The temperatures 264ºC, 274ºC and 285ºC, thought to correspond to the onset of the three overlapping peaks in the DSC are highlighted by red arrows.*

It is also noted that starting from 295ºC the WAXS signal remains almost unchanged, which is unexpected considering that the maximum of the third exothermic peak occurs at about 315ºC. It is possible that there is an error in the correspondence between DSC and XRD temperatures due to difficulties in identifying the various DSC peaks because of the overlaps, but, if that were the case, only the precise values of the temperatures at which the changes occur would be incorrect, not the qualitative analysis of the results.

4.2 Ce30La70

Figure 4.11 shows the DSC signal of Ce30La70. Also here, there is an initial exothermic phenomenon associated with the structural relaxation that starts at T_r~115ºC and ends with the glass transition temperature T_g~165ºC. After that, there is a more evident peak with an onset at T_1=180ºC and finally three close peaks between T_2=260ºC and 350ºC. Similarly to the previous case there are no variations in terms of SAXS and WAXS during the first relaxation phenomenon.

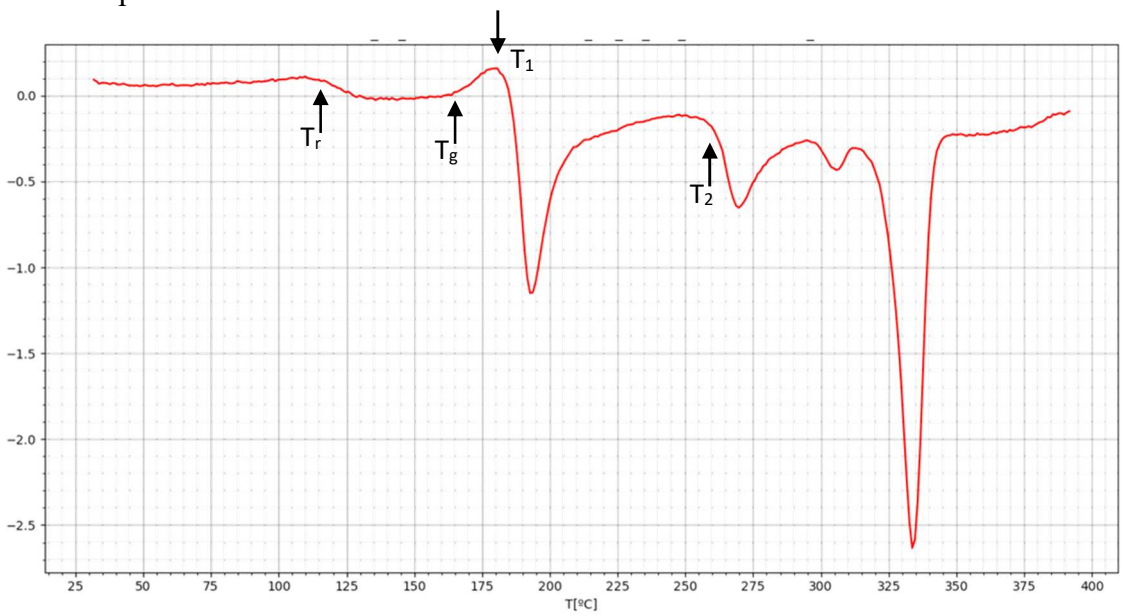

Figure 4.11: *DSC plot for Ce30La70 heated at 5 K/min until 375ºC*

To verify the correct correspondence between the temperatures in the DSC and those of the WAXS (and SAXS) signal, WAXS intensity maps were created, and corrected temperature scales (according to the method described in the previous chapter) were aligned with those of the DSC. Figure 4.12 shows the map for Ce30La70. It is possible to notice that, except for the first structural relaxation, for which no changes in the WAXS signal are expected, all the phenomena recorded by DSC show changes in terms of the position and intensity of the peaks in the WAXS. Therefore, the temperature correction seems to have been carried out correctly for this composition.

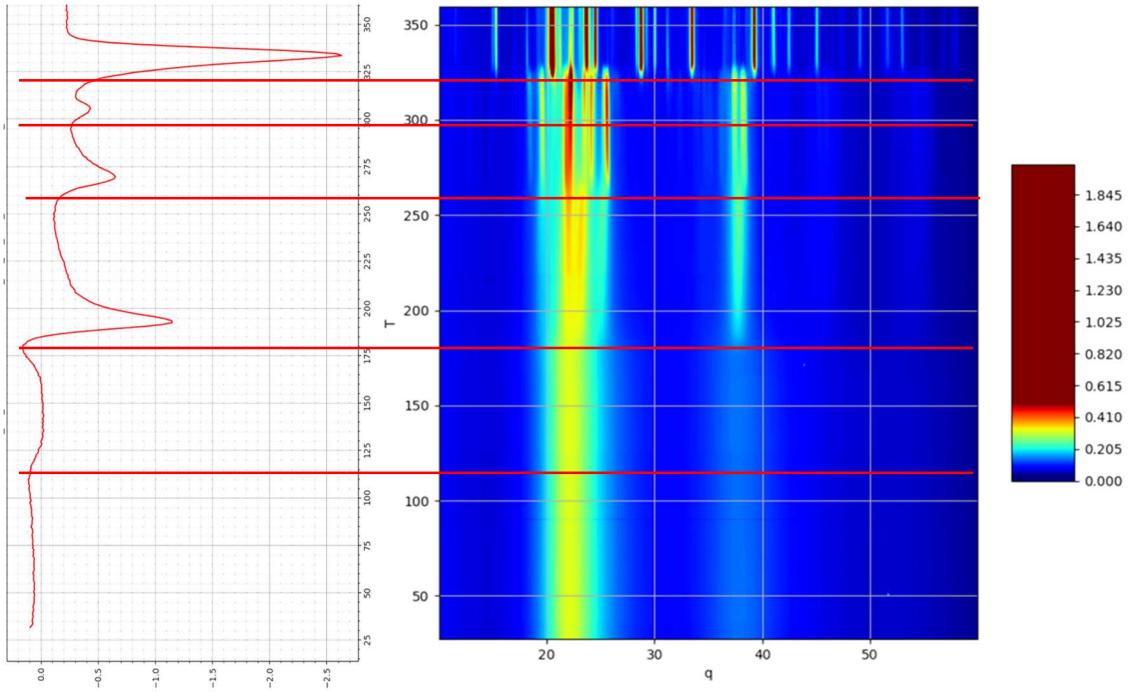

***Figure 4.12**: (left) DSC graph (rotated by 90° compared to the usual orientation) for Ce30La70. (right) 2D map of WAXS intensities for Ce30La70. The temperatures of the two analyses are aligned, and the red lines represent the onset temperatures of the DSC peaks.*

4.2.1 From 180ºC to 245ºC

The first exothermic phenomenon after the relaxation causes an undulation of the first amorphous WAXS peak and an increase in intensity and narrowing of the second. In the SAXS signal, a variation can be observed at intermediate q values (q~0.2), as shown in Figure 4.13.

Differently from the previously analysed composition (Ce0La100), where the variations in the two WAXS peaks occurred in different temperature ranges, in this case, the changes just described both start at around the onset of the DSC peak, at approximately 180ºC. Furthermore, as seen from the comparison between Figure 4.3, 4.4 and 4.13, while changes in the second peak are similar for the two compositions, those in the first peak are qualitatively different.

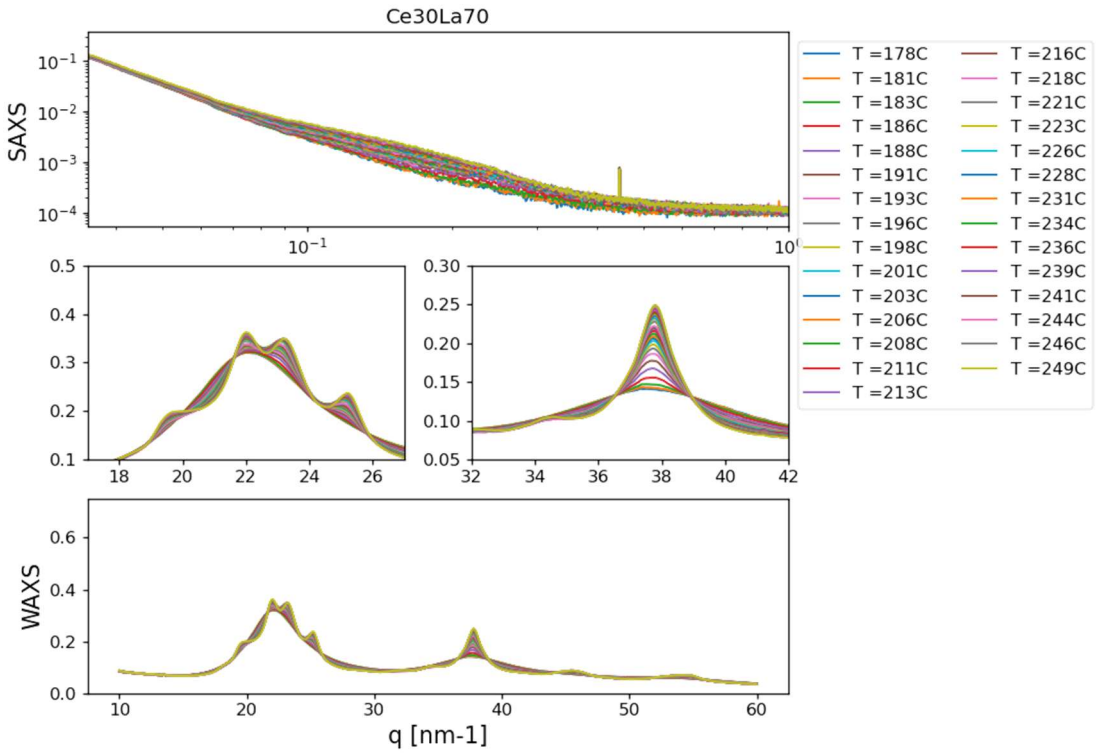

***Figure 4.13**: SAXS (top) and WAXS (bottom) intensity patterns for Ce30La70 heated at 5 K/min from 178ºC to 249ºC. The two middle plots are magnifications of the sharp amorphous peaks in WAXS.*

The sample was observed under FIBSEM microscope to try to detect the presence of heterogeneities; however, no changes were observed between the as-prepared sample (Figure 4.14) and the sample at 225ºC (Figure 4.15).

EDS analysis revealed a higher presence of oxygen and aluminium on the surface of both samples (in Figure 4.16 are shown the contents of Al and O for the as-prepared sample), suggesting that these two elements have reacted to form an aluminium oxide layer on the surface. Additionally, the adhesion of the surface layer applied for FIBSEM analysis is better for the sample at 225ºC. This result might be contradictory since the as-prepared sample is less thermally stressed, but it is important to note that the preparation of the samples for FIBSEM analysis did not account for which side of the sample was exposed to the ion beam.

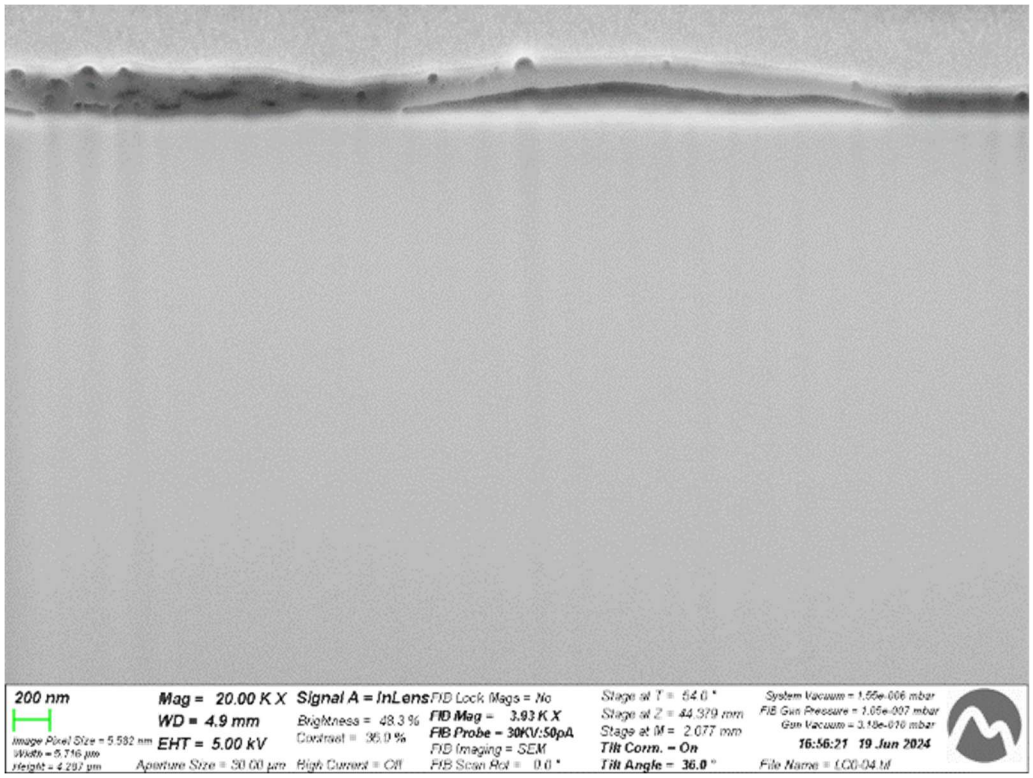

***Figure 4.14**: SEM micrograph of Ce30La70 as-quenched prepared using FIB. The image was acquired with the SE detector at an accelerating voltage of 5 kV. The scale bar represents 200 nm.*

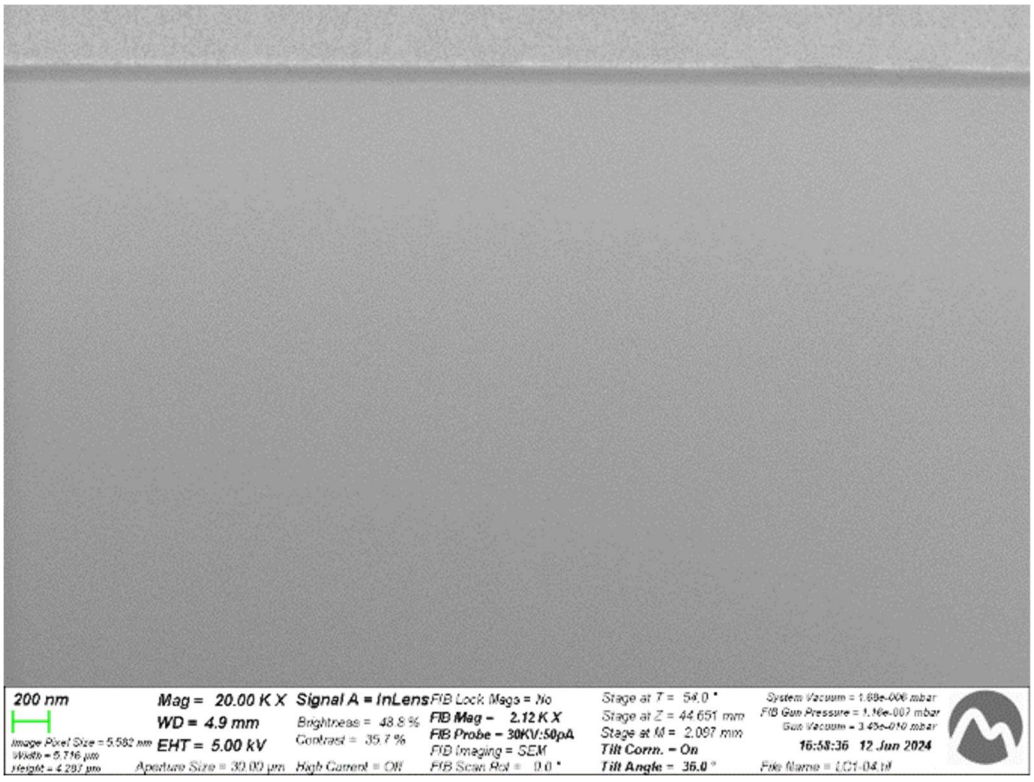

***Figure 4.15**: SEM micrograph of Ce30La70 heated to 225ºC prepared using FIB. The image was acquired with the SE detector at an accelerating voltage of 5 kV. The scale bar represents 200 nm*

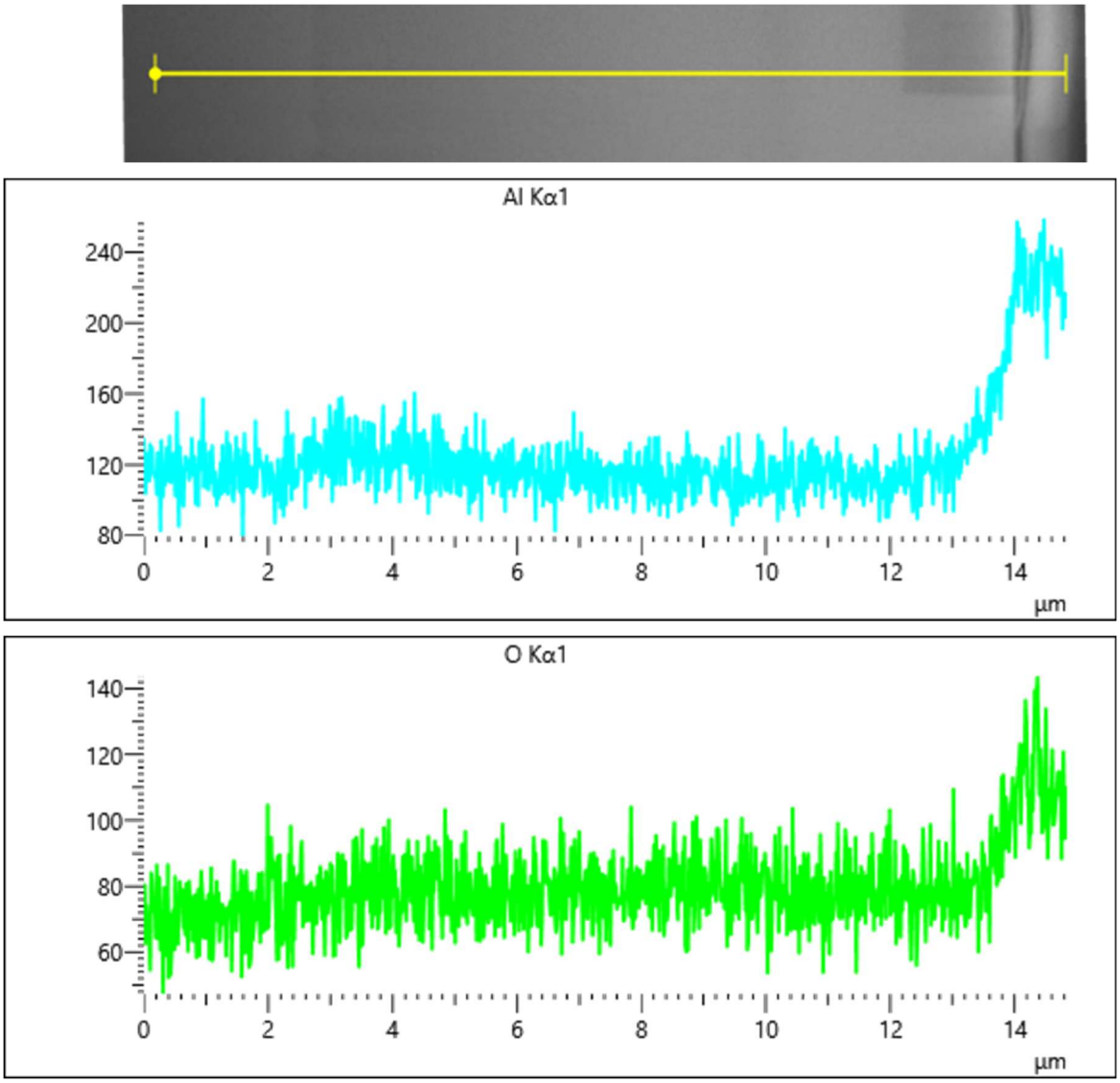

***Figure 4.16**: The content of the Al and O is represented as a function of the position along the line*

In the considered temperature range, we observe contrasting results between SAXS and SEM: in SAXS, the appearance of the shoulder suggests the presence of electron density fluctuations associated with the formation of structural or chemical heterogeneities on nanometric scale. However, these heterogeneities do not emerge in the SEM image. Therefore, the heterogeneities detected by SAXS analysis might not have sufficiently high contrast when observed using the SE detector, as it is sensitive to topography and surface variations but low sensitivity to internal density and compositional fluctuation.

4.2.2 From 250ºC to 280ºC

In the temperature range between 250ºC and 280ºC, the specimen undergoes an exothermic transformation that increases the intensity of the SAXS signal for intermediate q values,

while the WAXS signal attains a characteristic appearance of a crystallized material due to the presence of the peaks shown in Figure 4.17. However, these peaks are quite broad, and it is still possible to perceive the two halos of the glassy material. The described signal has been interpreted as a process of nanocrystallization. FIBSEM microscopy did not reveal the presence of crystals; this could be attributed to the entities being too small or the low contrast between the crystals and the matrix.

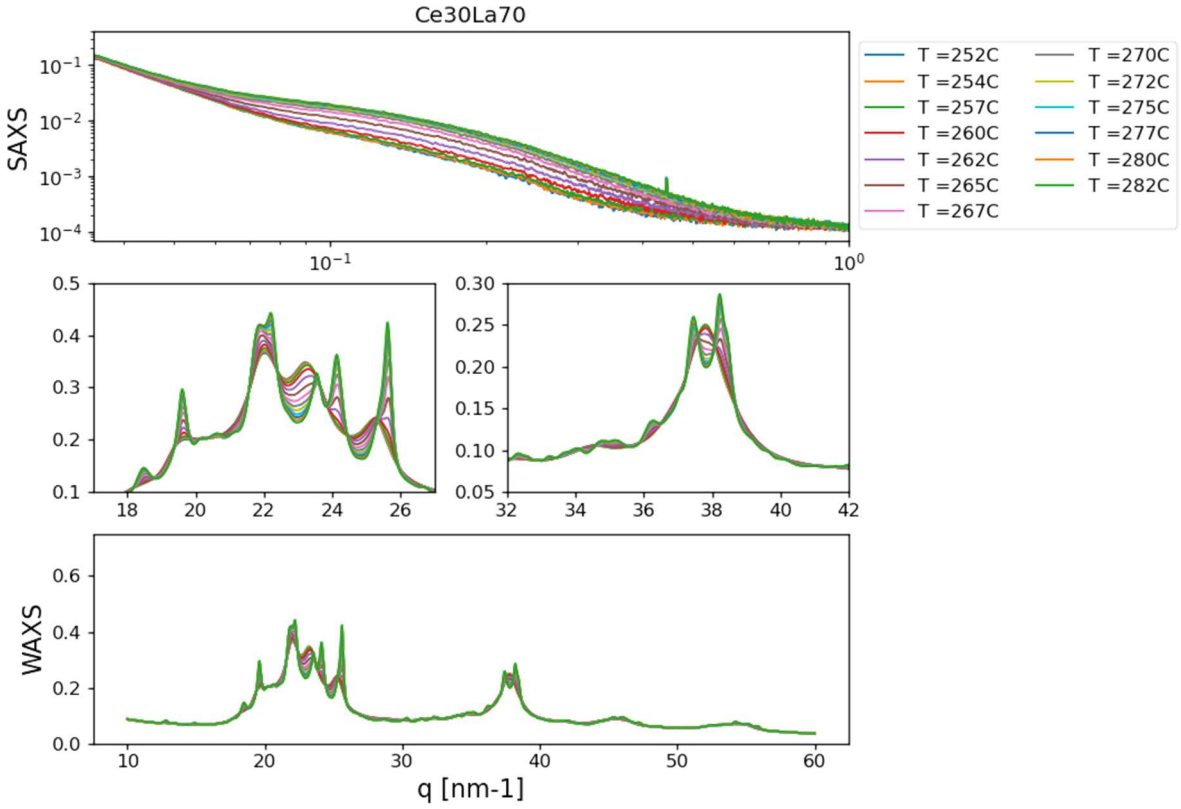

***Figure 4.17**: SAXS (top) and WAXS (bottom) intensity patterns for Ce30La70 heated at 5 K/min from 252ºC to 282ºC. The two middle plots are magnifications of the sharp amorphous peaks in WAXS.*

4.2.3 From 280ºC to 350ºC

Figure 4.18 shows the results of SAXS and WAXS analyses between 280ºC and 350ºC. The WAXS signal at the end of the transformation has the typical shape of a crystallized material, and the increase in the SAXS signal at low q values (corresponding to larger lengths in the actual material) is due to the growth of the formed crystals. From the SAXS signal, a slight decrease in intensity at higher q values can also be observed, which might be due to a reduction in small-scale inhomogeneities. In WAXS results, we have the disappearance of some peaks in favour of others, which can be interpreted as a phase transition in the formed

crystals or the utilization of atoms from the already created crystals to create crystals with a different composition.

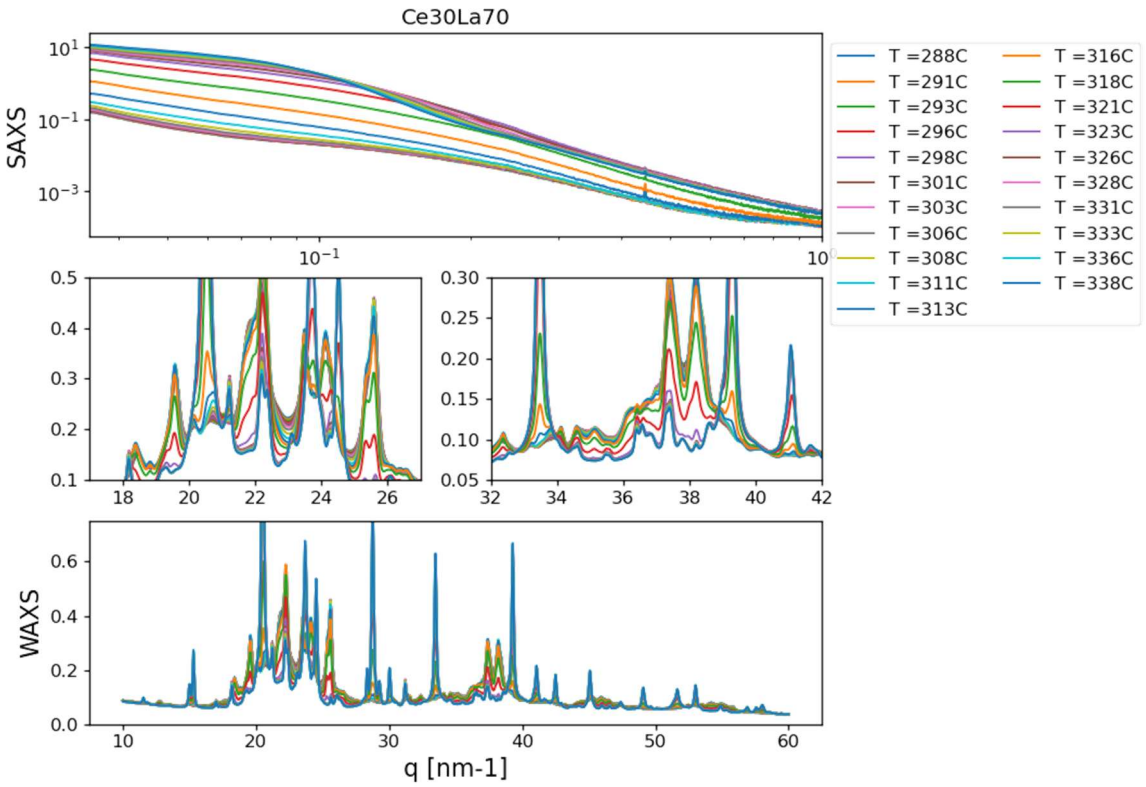

***Figure 4.18**: SAXS (top) and WAXS (bottom) intensity patterns for Ce30La70 heated at 5 K/min from 288ºC to 338ºC. The two middle plots are magnifications of the sharp amorphous peaks in WAXS.*

The DSC signal in this temperature range show two exothermic processes, one with an onset at around 300ºC and the other at around 315ºC. From figure 4.18, it can be observed that in the SAXS plot, between approximately 306ºC and 313ºC, there is a very slight increase in the signal at low q values. This peak could, therefore, be due to the growth of previously formed crystals. As the WAXS, show in figure 4.19 for this narrow temperature range, it is characterized not so much by the appearance of new peaks but rather by the increase in intensity and definition of those already present, confirming that it could be the growth of already existing peaks.

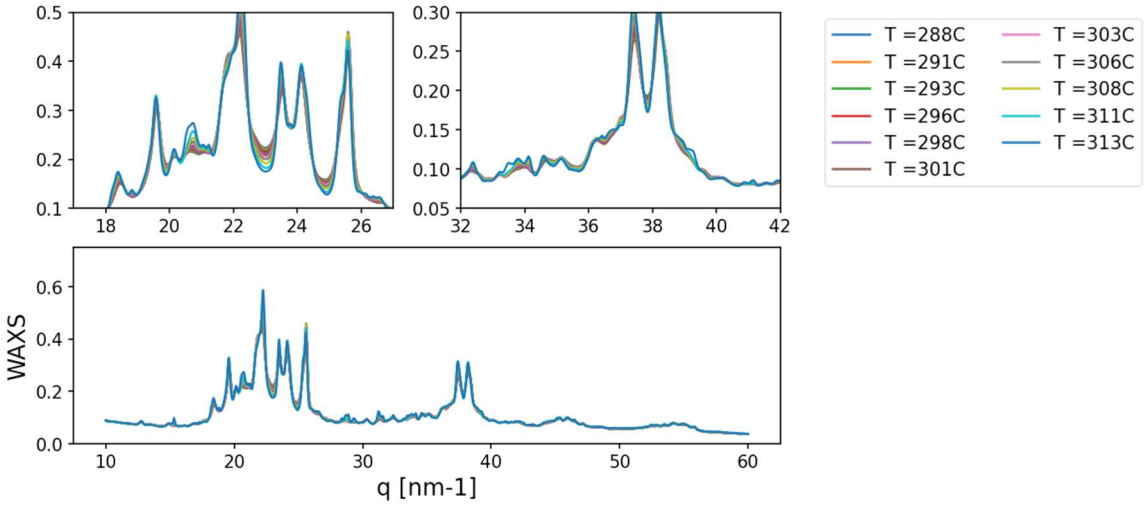

***Figure 4.19**: WAXS (bottom) intensity patterns for Ce30La70 heated at 5 K/min from 288ºC to 313ºC. The two top plots are magnifications of the sharp amorphous peaks in WAXS.*

The other peak, with an onset around 315ºC, is accompanied by a SAXS signal that initially grows uniformly across all q values and then, from around 321ºC, increases at lower q values and decreases at higher q values. In the WAXS signal, on the other hand, there is the formation of new peaks and the disappearance of others. Furthermore, while up to 313ºC (figure 4.19) the initial amorphous halos could still be well perceived, indicating a sort of composite with an amorphous matrix and dispersed crystals, here, at the end of the transformation, the material reaches an almost completely crystalline structure. As mentioned at the beginning of the paragraph, this final transformation is due to the formation of new crystals and their growth, accompanied by the reduction of smaller crystals, whose atoms may have been used for the formation of the new crystals.

4.3 Ce70La30

The DSC plot of Ce70La30 composition is shown in figure 4.20. The behaviour is similar to that observed for previous compositions: there is an initial relaxation at T_r=95ºC which ends with the glass transition temperature T_g=140ºC; in this range of temperature there are not changes in SAXS and WAXS. Afterwards, there are a series of three exothermic transformations that will be analysed in more detail within this section.

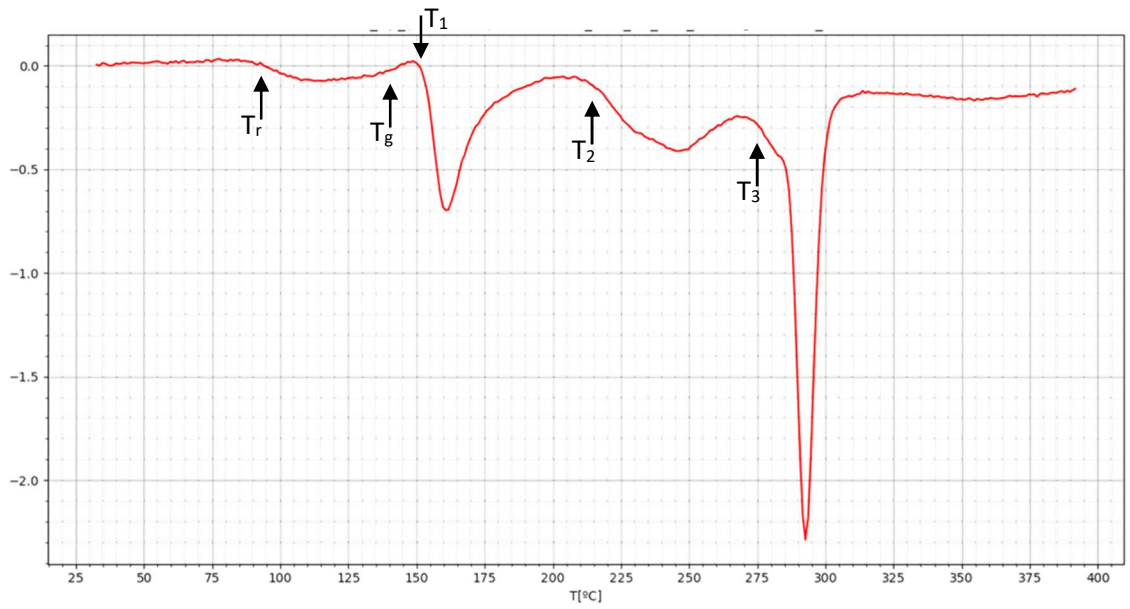

Figure 4.20: *DSC plot for Ce70La30 heated at 5 K/min until 400°C*

The correct correspondence between the DSC and XRD temperatures was verified also for this composition. As shown in Figure 4.21, each peak corresponds to a change in the WAXS signal. This confirms the accurate temperature correction of the XRD.

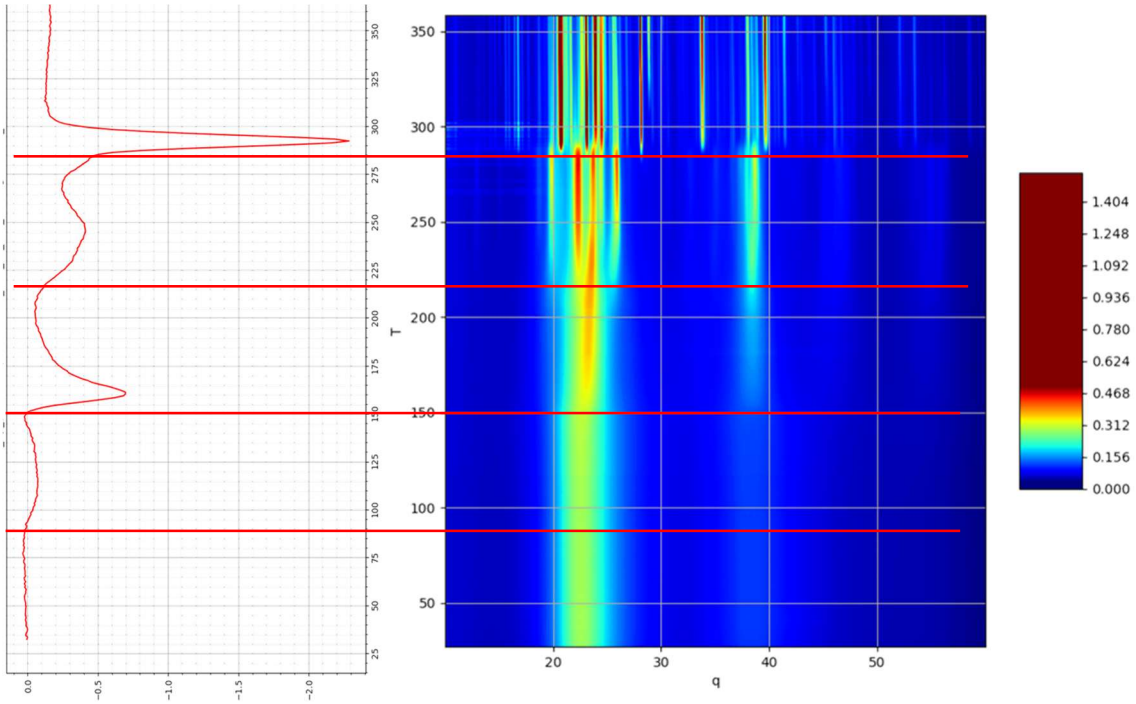

Figure 4.21*: (left) DSC graph (rotated by 90° compared to the usual orientation) for Ce70La30. (right) 2D map of WAXS intensities for Ce70La30. The temperatures of the two analyses are aligned, and the red lines represent the onset temperatures of the DSC peaks.*

4.3.1 From 150ºC to 200ºC

Figure 4.22 depicts the WAXS and SAXS signals between 150ºC and 200ºC. Although the peak in the DSC appears very similar to that observed for Ce0La100 and Ce30La70, the changes in the WAXS are qualitatively different, especially for the first amorphous peak at lower q values. In this case, we do not observe the undulation seen in the previously analysed samples, but instead, there is a variation characterized by an increase in intensity and a narrowing of the peak, similar to what is observed for the second peak. The WAXS signal at both the beginning and the end of this first peak is typical of an amorphous structure, but the narrowing of the peaks and their shift to higher values are indicative of an increase in order and density. Therefore, the transformation corresponds to a transition between a less ordered liquid and a more ordered liquid. The SAXS does not show evident variations during this initial transformation and the FIBSEM analysis do not show heterogeneities in the material (Figure 4.23).

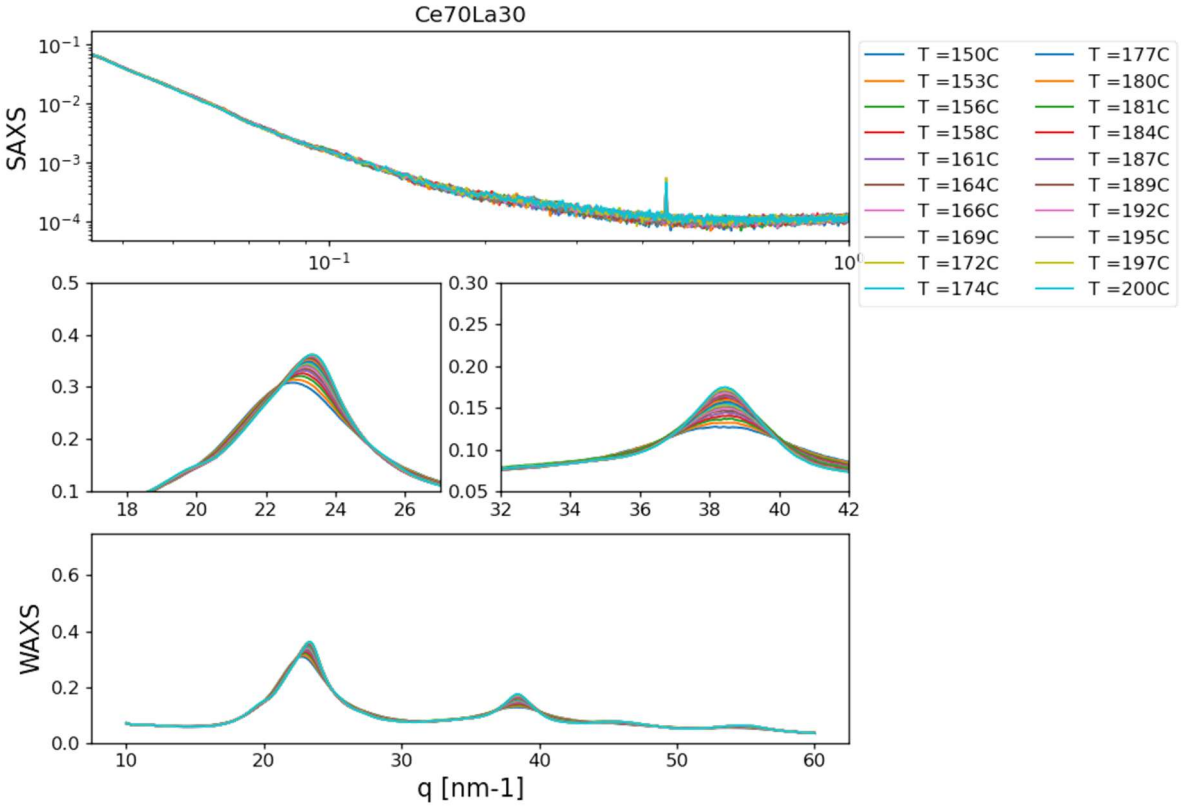

***Figure 4.22**: SAXS (top) and WAXS (bottom) intensity patterns for Ce70La30 heated at 5 K/min from 150ºC to 200ºC. The two middle plots are magnifications of the sharp amorphous peaks in WAXS.*

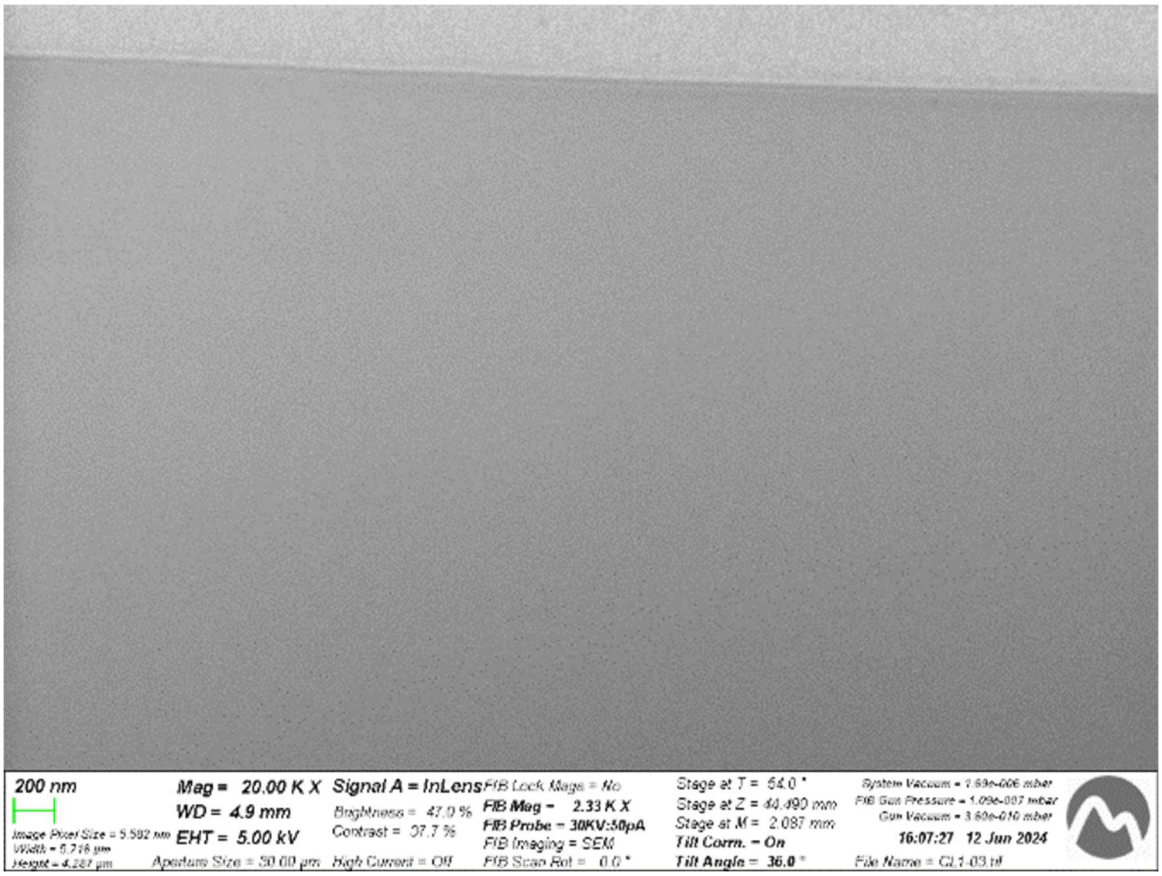

***Figure 4.23**: SEM micrograph of Ce70La30 heated to 185ºC prepared using FIB. The image was acquired with the SE detector at an accelerating voltage of 5 kV. The scale bar represents 200 nm*

4.3.2 From 210ºC to 270ºC

The phenomenon between 210ºC and 270ºC is associated with changes in SAXS and WAXS, shown in figure 4.24, similar to those observed for Ce30La70 between 250ºC and 280ºC: the transformation is accompanied by an increase in SAXS signal intensity and the formation of peaks around fairly well-defined q values but still quite broad, typical of nanocrystal formation process in WAXS. As for the images collected with FIBSEM, they show the presence of heterogeneities with sizes up to ~20 nm within the amorphous phase, as shown in figure 4.25. The shoulder in the SAXS signal suggest a weak spatial correlation between the particles between the particles. This tendency of heterogeneities to remain at a certain distance from each other could be due to the fact that their formation depletes the immediate surrounding environment of certain elements, thereby preventing the nucleation of new heterogeneities of the same type in the closest region. This theory is supported by a careful analysis of the image collected with FIBSEM: the heterogeneities that formed, sown in dark grey in figure 4.25, are all surrounded by a sort of lighter halo.

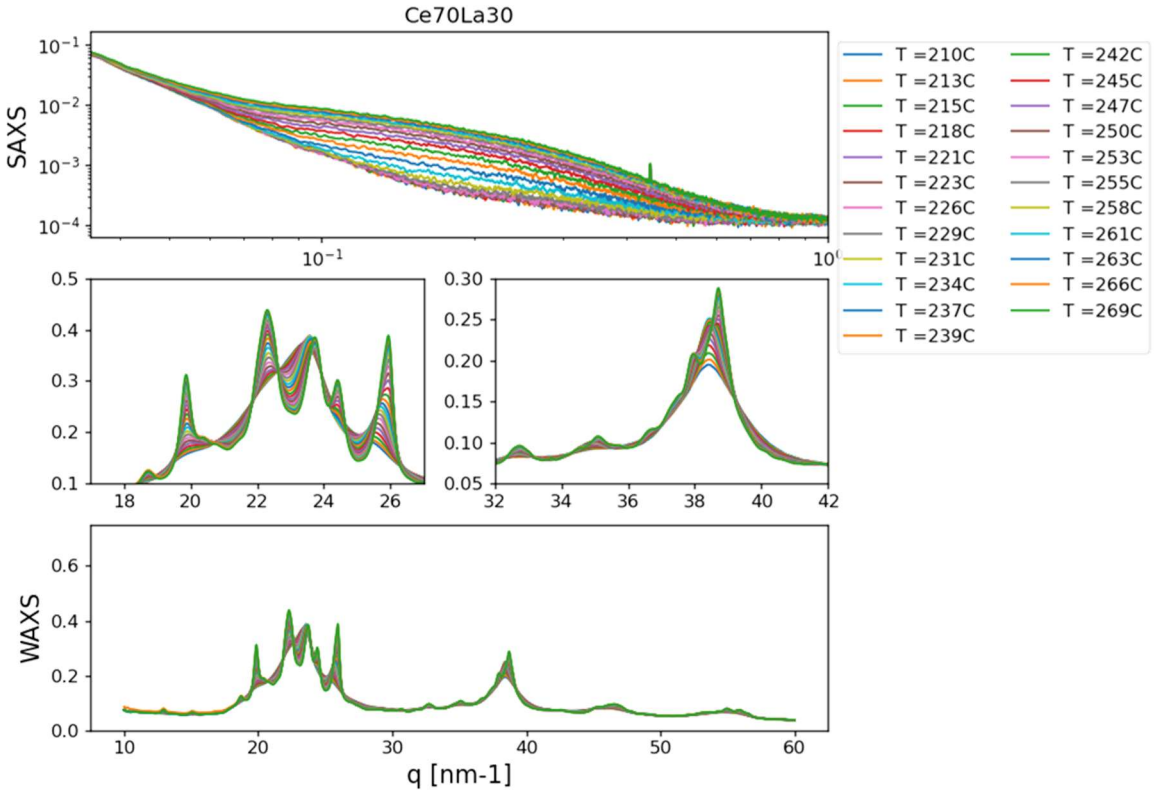

***Figure 4.24**: SAXS (top) and WAXS (bottom) intensity patterns for Ce70La30 heated at 5 K/min from 210ºC to 269ºC. The two middle plots are magnifications of the sharp amorphous peaks in WAXS.*

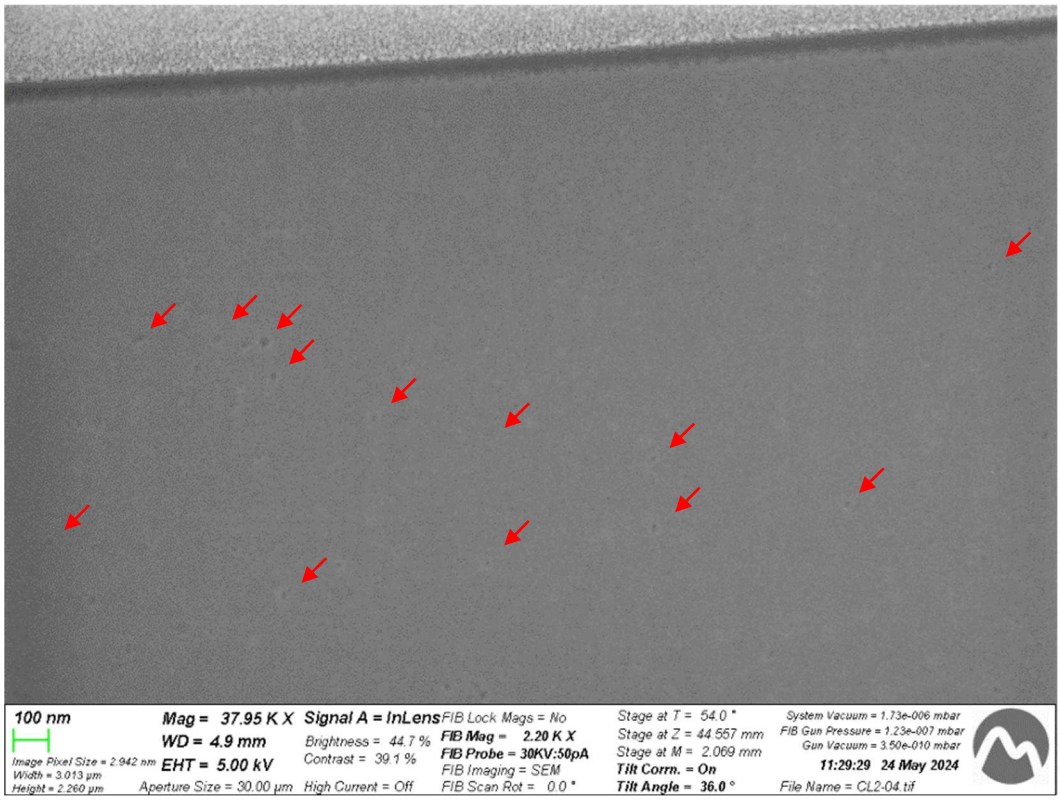

***Figure 4.25**: SEM micrograph of Ce70La30 heated to 255ºC prepared using FIB. The image was acquired with the SE detector at an accelerating voltage of 5 kV. The scale bar represents 200 nm*

4.3.3 From 270ºC to 315ºC

The last peak, between 270ºC and 315ºC, is associated with a crystallization phenomenon: similarly to what happened with the other analysed compositions, here too there is a decrease in the intensity of some previously formed WAXS peaks and the formation and growth of other well-defined peaks, while the SAXS signal intensity increases at small q values due to the growth of these crystals during the transformation, as shown in figure 4.26. disappearance of some peaks in WAXS could indicate a phase transition in the already formed crystals or the use of their atoms for the formation and growth of new crystals.

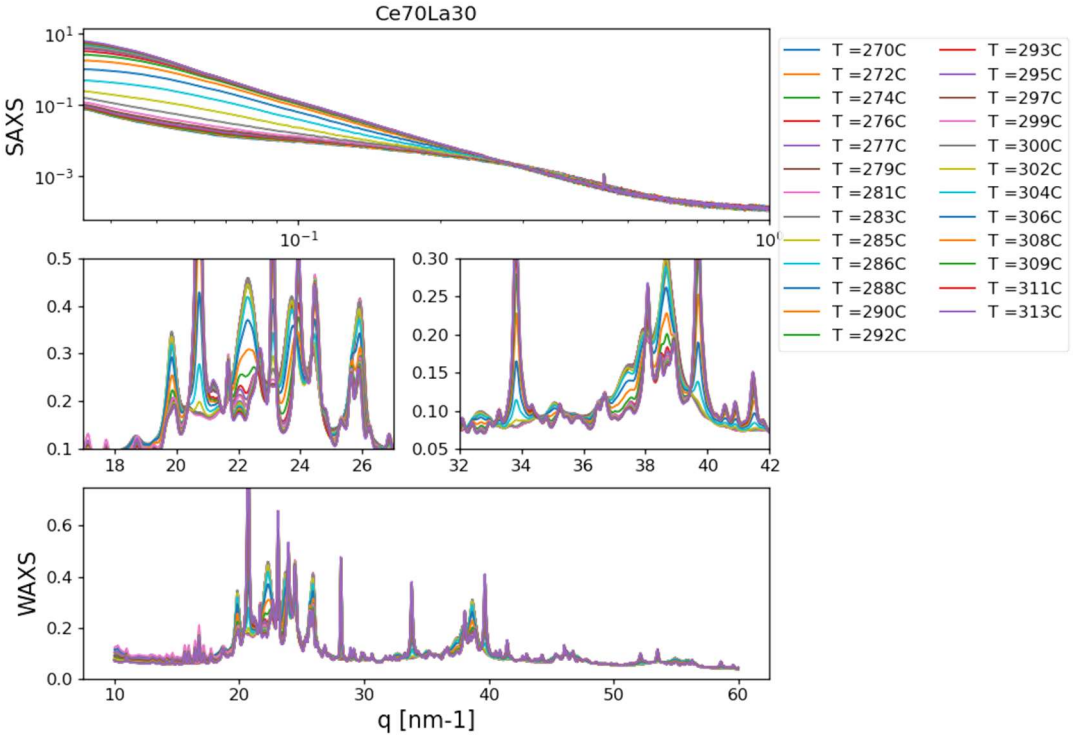

***Figure 4.26**: SAXS (top) and WAXS (bottom) intensity patterns for Ce70La30 heated at 5 K/min from 270ºC to 313ºC. The two middle plots are magnifications of the sharp amorphous peaks in WAXS*

The crystals were also observed with FIBSEM, using both SE and BSE detectors. In the former (Figure 4.27 and 4.28) there is a clear structure consisting of crystals interspersed with lighter amorphous zones. However, in the latter (Figure 4.29), the crystals are almost imperceptible. This difference is due to the fact that both the crystals and the amorphous regions are likely composed of the same elements. Moreover, the contrast in this case depends on the atomic number difference, which for La and Ce is 57 and 58, respectively. Thus, the varying presence of these two elements in the two phases does not significantly contribute to the contrast in the image.

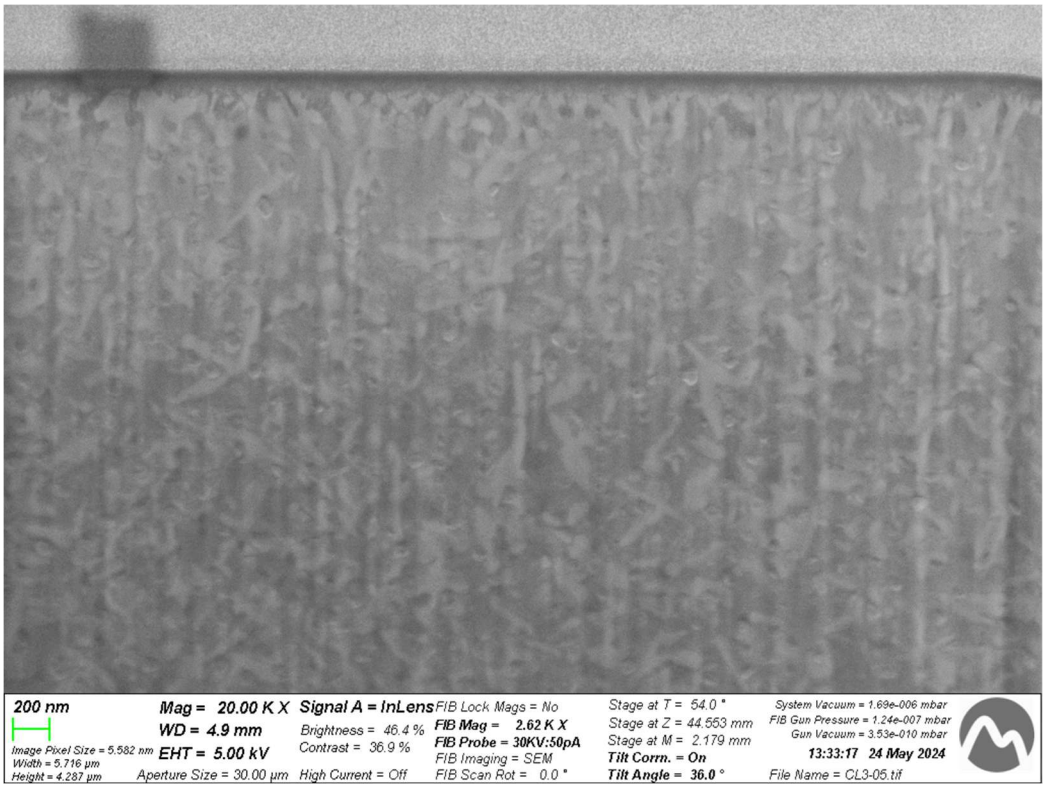

***Figure 4.27**: SEM micrograph of Ce70La30 heated to 315ºC prepared using FIB. The image was acquired with the SE detector at an accelerating voltage of 5 kV. The scale bar represents 200 nm*

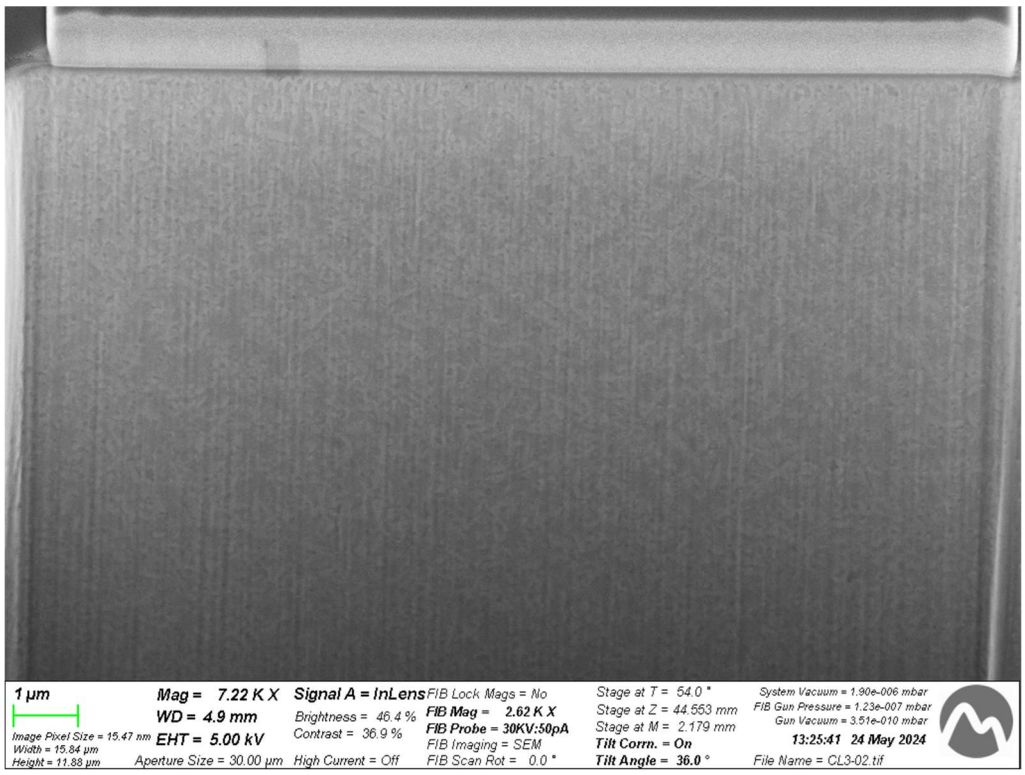

***Figure 4.28**: SEM micrograph of Ce70La30 heated to 315ºC prepared using FIB. The image was acquired with the SE detector at an accelerating voltage of 5 kV. The scale bar represents 1µm*

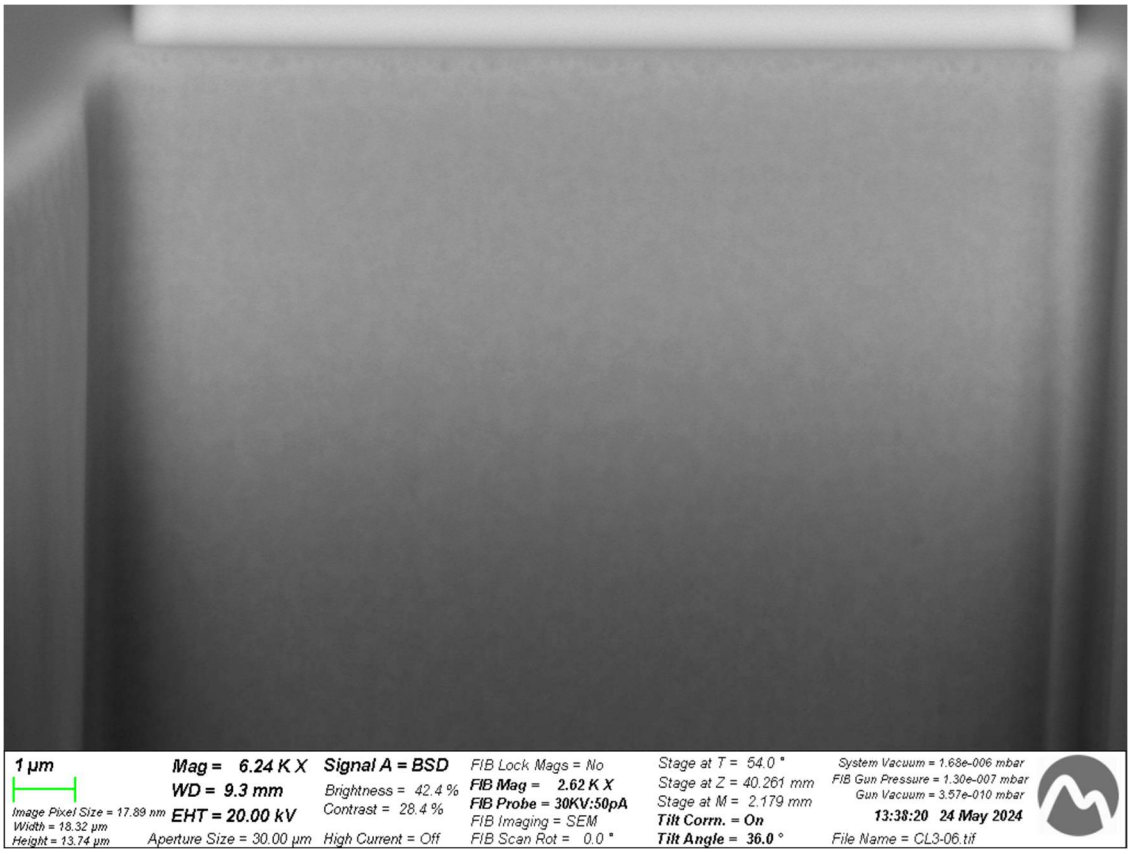

***Figure 4.29**: SEM micrograph of Ce70La30 heated to 315ºC prepared using FIB. The image was acquired with the BSD detector at an accelerating voltage of 20 kV. The scale bar represents 1µm.*

From figures 4.27 and 4.28, vertical striation are also visible in the sample. This effect is not observed in figure 4.29, indicating that these striations are caused by topographical differences rather than compositional ones. For this reason, it is ruled out that they are related to preferential crystal growth along them; instead, it is thought that they could be due to the milling phase using the ion beam.

4.4 Ce100La0

The DSC signal (Figure 4.30) recorded for composition Ce100La0 is qualitatively similar to that observed for Ce0La100, but in this case the various peaks are at lower temperatures. In the first part of the graph the peaks are not well defined, so the WAXS and SAXS plots were studied to identify the end of the relaxation, assuming that, as in other cases, no changes occurred in the SAXS and WAXS signals. Since the SAXS/WAXS signal changes starting from about 125ºC it was concluded that the broad peak at 110ºC could correspond to relaxation, and, by analogy with other compositions, that T_g~125ºC could be identified just

before the peak at T_1=130ºC. At T_2=195ºC there is another slight peak and from T_3=230ºC three overlapping peaks.

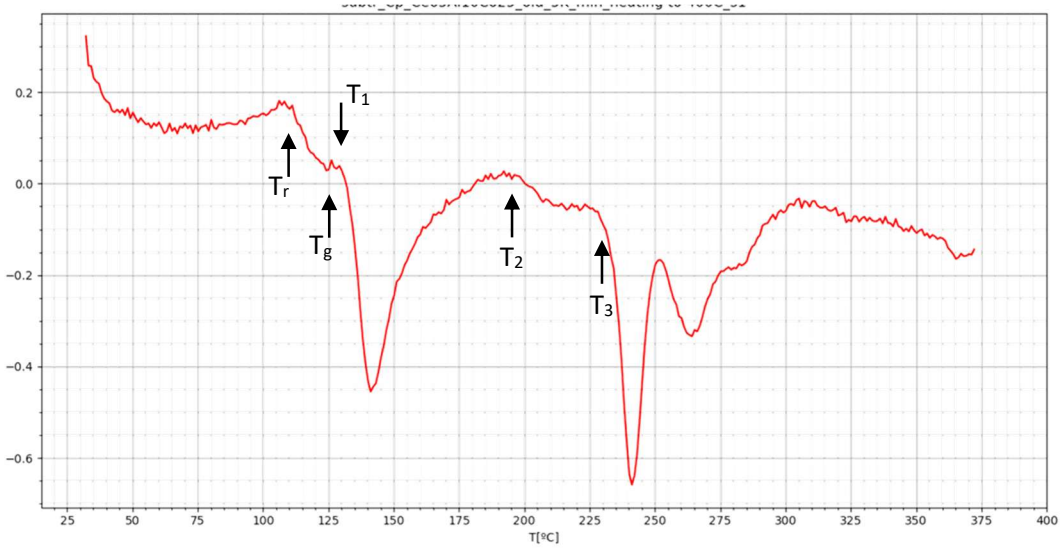

Figure 4.30: *DSC plot for Ce100La0 heated at 5 K/min until 375ºC*

4.4.1 From 125ºC to 190ºC

Between 125ºC and 190ºC, the changes observed in SAXS/WAXS (Figure 4.31) are similar to those seen for Ce70La30 between 150ºC and 200ºC: the two broad WAXS peaks typical of an amorphous structure narrow, increase in intensity and shift towards higher q values. Additionally, another effect, which was not commented on for Ce70La30 but was present, is the appearance of two almost imperceptible amorphous peaks at q ~ 48 nm^{-1} and q ~ 56 nm^{-1}. All these changes are associated with a transition from a disordered liquid to a slightly ordered liquids, as in the previous case.

The analogous study to this one conducted by Lou et al. in 2020 [33] on the composition Ce100La0 revealed a rather evident increase in the SAXS signal corresponding to the DSC peak associated with the liquid-liquid transition. The reasons for the absence of this increase in intensity in our case could be due to various factors, such as different experimental conditions, different sample composition (even small variations can lead to differences in results), or simply the use of different measuring instruments.

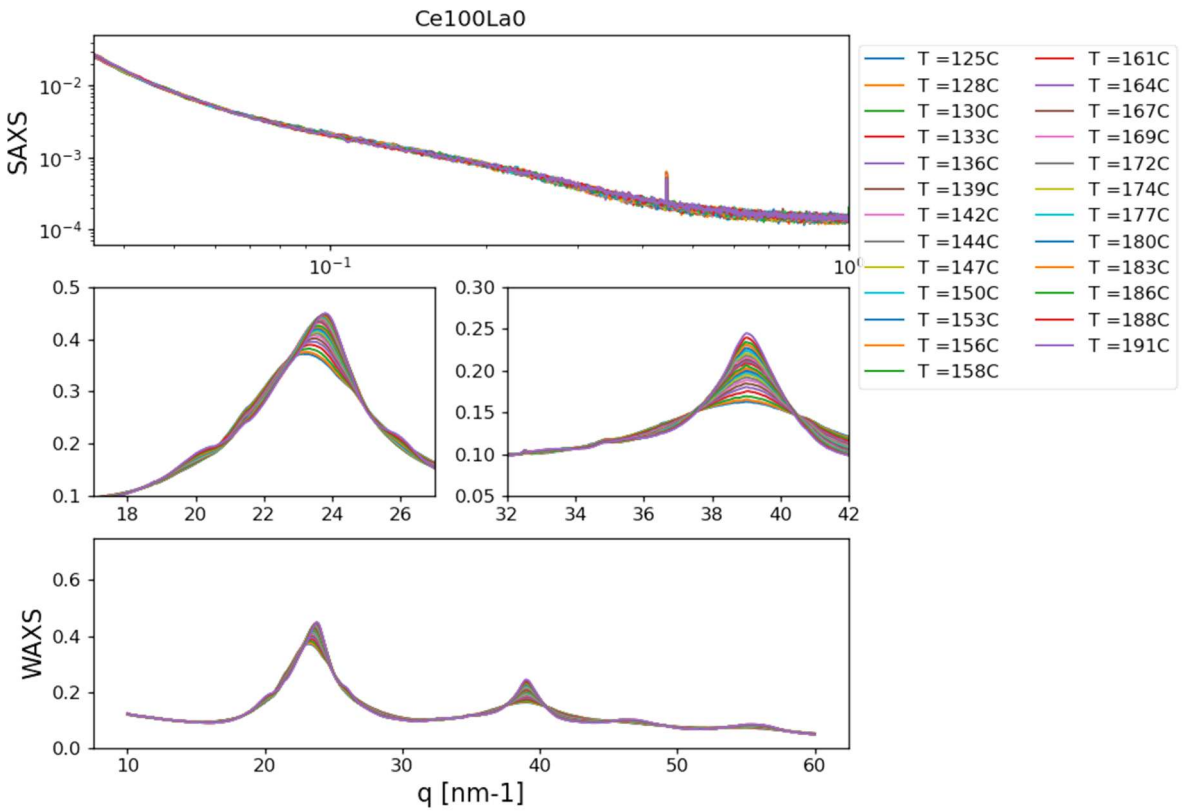

***Figure 4.31**: SAXS (top) and WAXS (bottom) intensity patterns for Ce100La0 heated at 5 K/min from 125ºC to 191ºC. The two middle plots are magnifications of the sharp amorphous peaks in WAXS*

4.4.2 From 195ºC to 225ºC

The changes in WAXS in the temperature range between 195ºC and 225ºC are similar to those observed in Ce70La30 between 210ºC and 270ºC and in Ce30La70 between 250ºC and 280ºC: there is the formation of fairly broad peaks but around well-defined q values. This phenomenon could be associated with the crystallization of small-sized crystals, as in the previous cases. However, unlike the other two compositions, the SAXS in this case does not show any changes. The absence of SAXS signal changes could be due to a contrast difference between the crystals and the amorphous phase that is not sufficient to cause a change in SAXS. WAXS and SAXS signal are shown in Figure 4.32. Another justification for the absence of a SAXS signal could have been the small size of crystals, but this was excluded as the FIBSEM image of the sample heated to 215ºC (Figure 4.33) shows some small heterogeneities within the amorphous matrix.

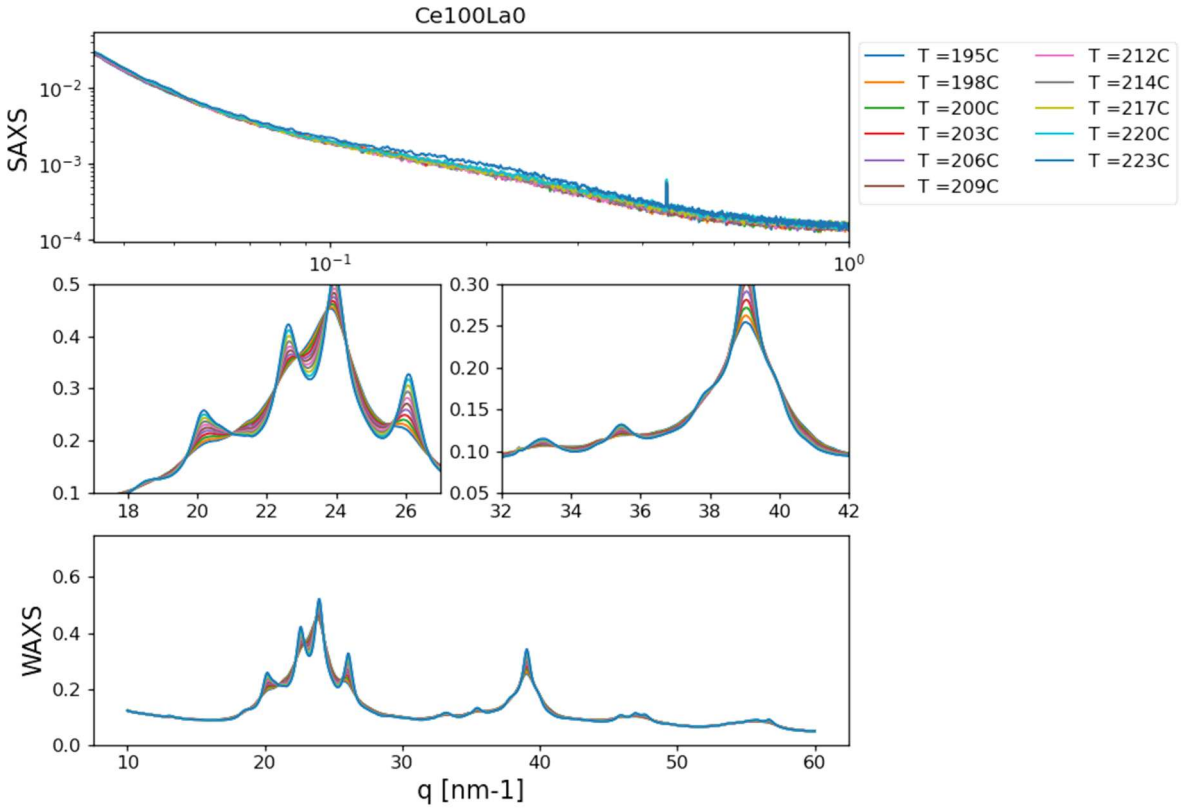

***Figure 4.32**: SAXS (top) and WAXS (bottom) intensity patterns for Ce100La0 heated at 5 K/min from 195ºC to 223ºC. The two middle plots are magnifications of the sharp amorphous peaks in WAXS*

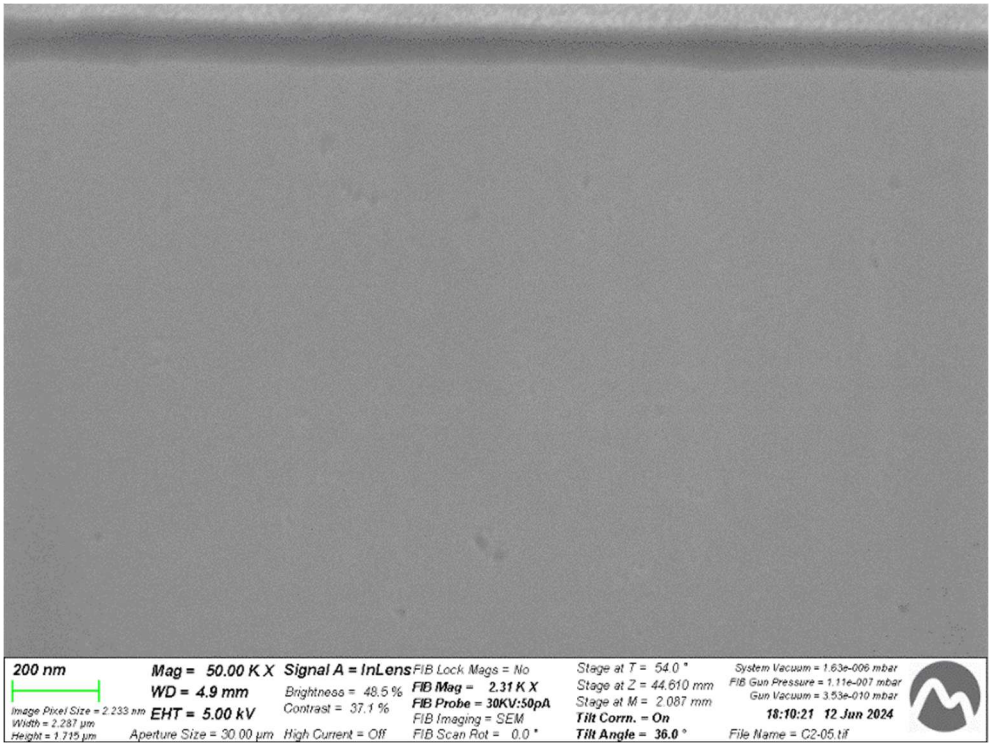

***Figure 4.33**: SEM micrograph of Ce100La0 heated to 215ºC prepared using FIB. The image was acquired with the SE detector at an accelerating voltage of 5 kV. The scale bar represents 200 nm*

4.4.3 From 230ºC to 310ºC

The last three peaks are associated with a crystallization process, as can be deduced from the WAXS graph shown in figure 4.34. At the beginning of the transformation, there is a sudden increase in the SAXS signal, which the continues to grow more gradually and slowly due to the growth of the formed crystals.

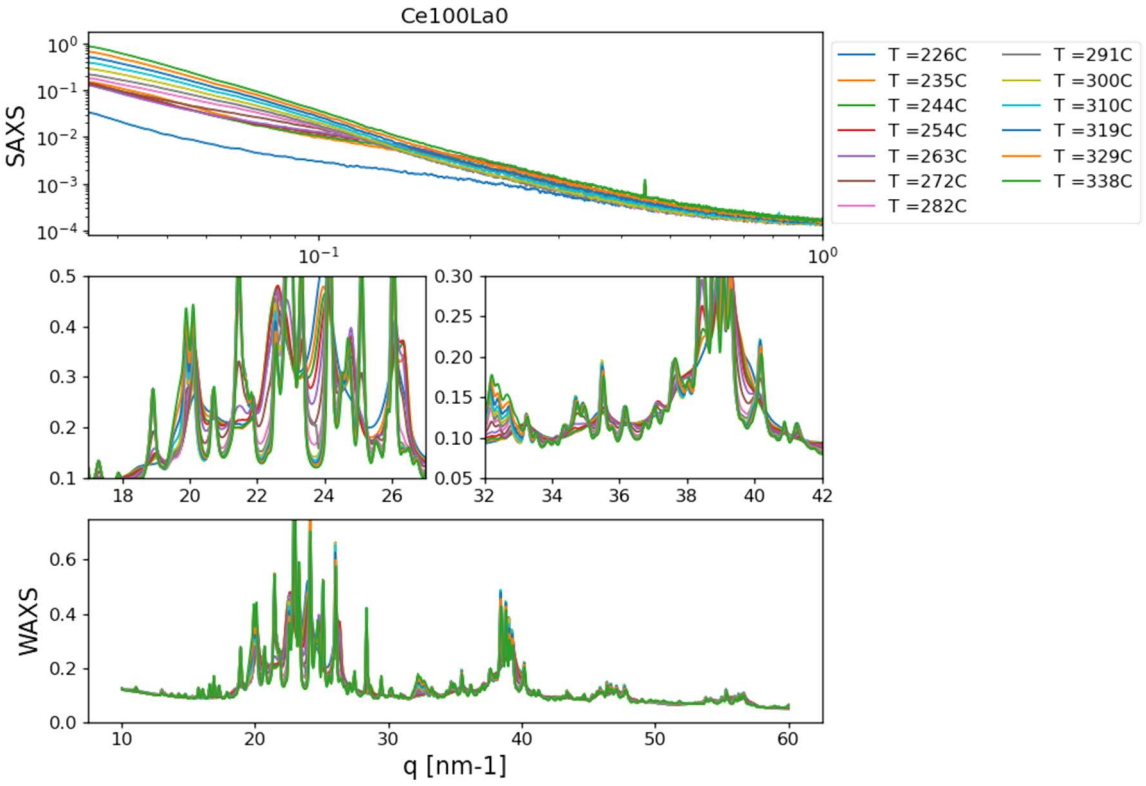

***Figure 4.34**: SAXS (top) and WAXS (bottom) intensity patterns for Ce100La0 heated at 5 K/min from 226ºC to 338ºC. The two middle plots are magnifications of the sharp amorphous peaks in WAXS*

As for FIBSEM, for this composition as well, similar considerations can be made to those observed for Ce70La30 regarding the difference between the images collected using SE detector (Figure 4.35) and those obtained with the BSD detector (Figure 4.36). In the former, there is good contrast that allows the formed crystals to be observed, while in the latter, they are barely perceptible. Another similarity lies in the striations in the SE image, which are absent in the BSD image and are therefore thought to be associated with topographical changes caused by ion beam rather than the direction of crystal growth.

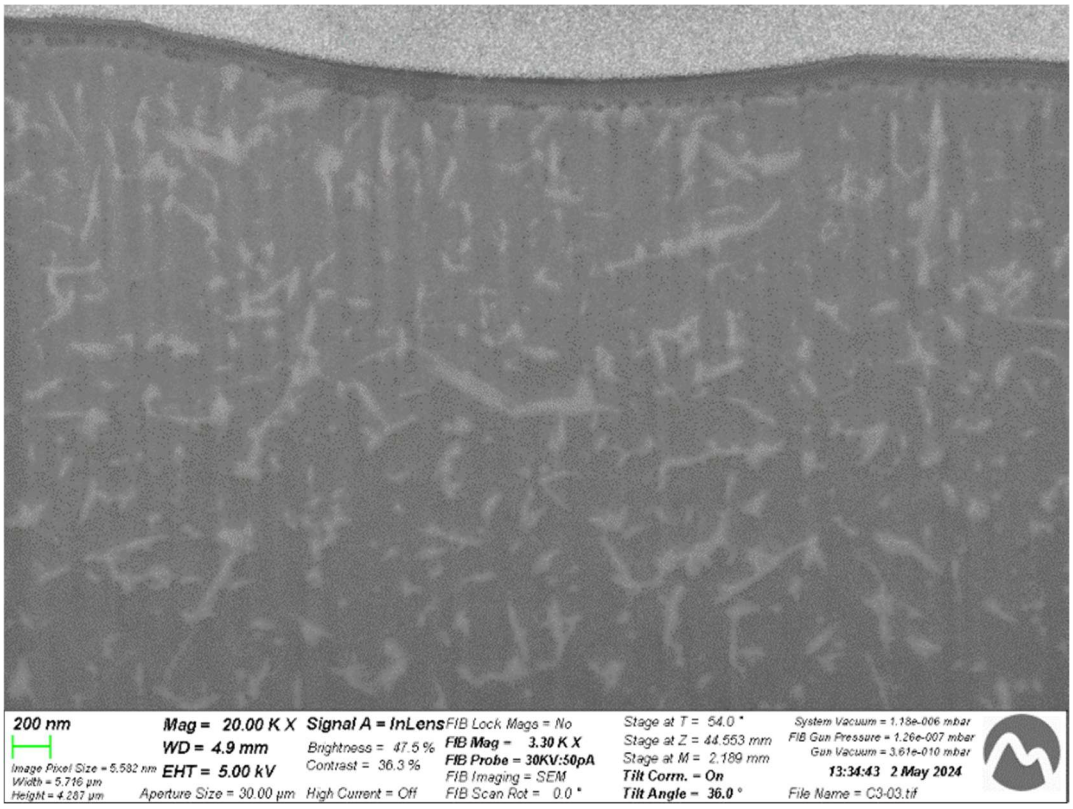

***Figure 4.35**: SEM micrograph of Ce100La0 heated to 305ºC prepared using FIB. The image was acquired with the SE detector at an accelerating voltage of 5 kV. The scale bar represents 200 nm*

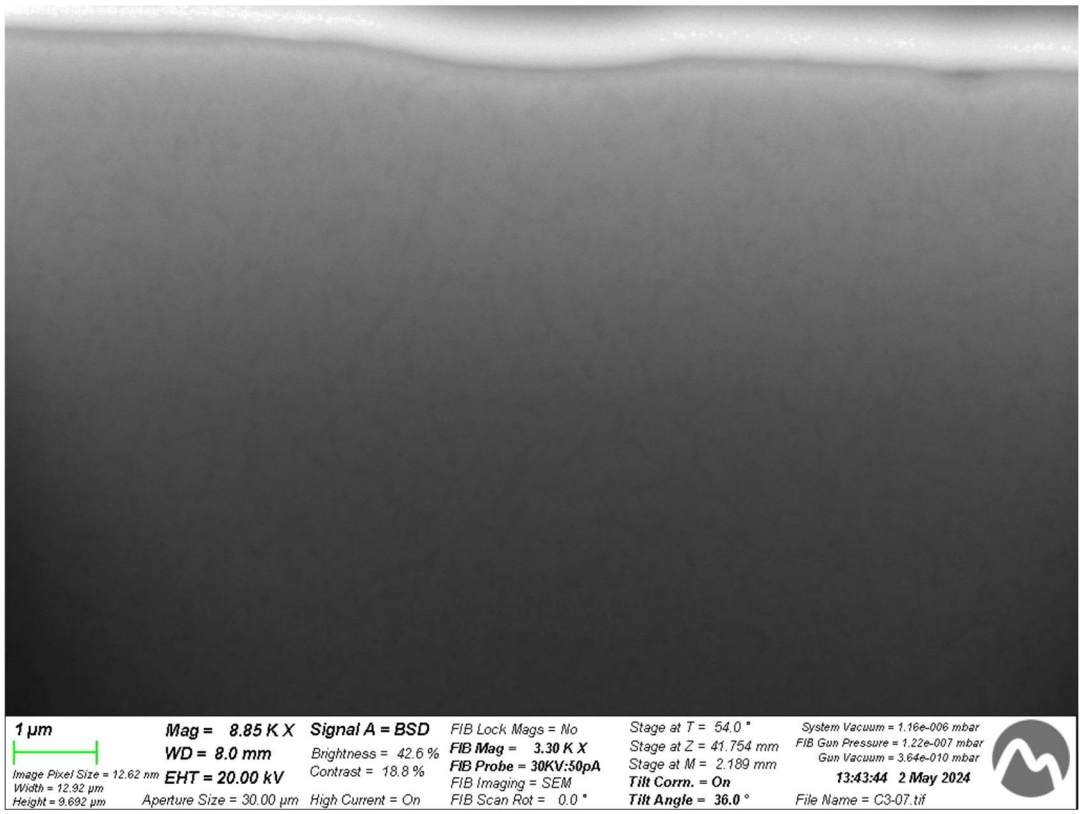

***Figure 4.36**: SEM micrograph of Ce100La0 heated to 305ºC prepared using FIB. The image was acquired with the BSD detector at an accelerating voltage of 20 kV. The scale bar represents 1 µm*

As with the other compositions, an attempt was made to study the three DSC peaks separately in this temperature range. As in the case of Ce0La100, this operation is not simple due to the partial overlap of the three DSC peaks.

By studying the changes in the WAXS/SAXS signal, three onsets of qualitatively different changes can be identified at temperature of 226ºC, 246ºC and 266ºC (indicated in figure 4.37), which could reasonably correspond to the onset temperatures of the three overlapping peaks in the DSC signal.

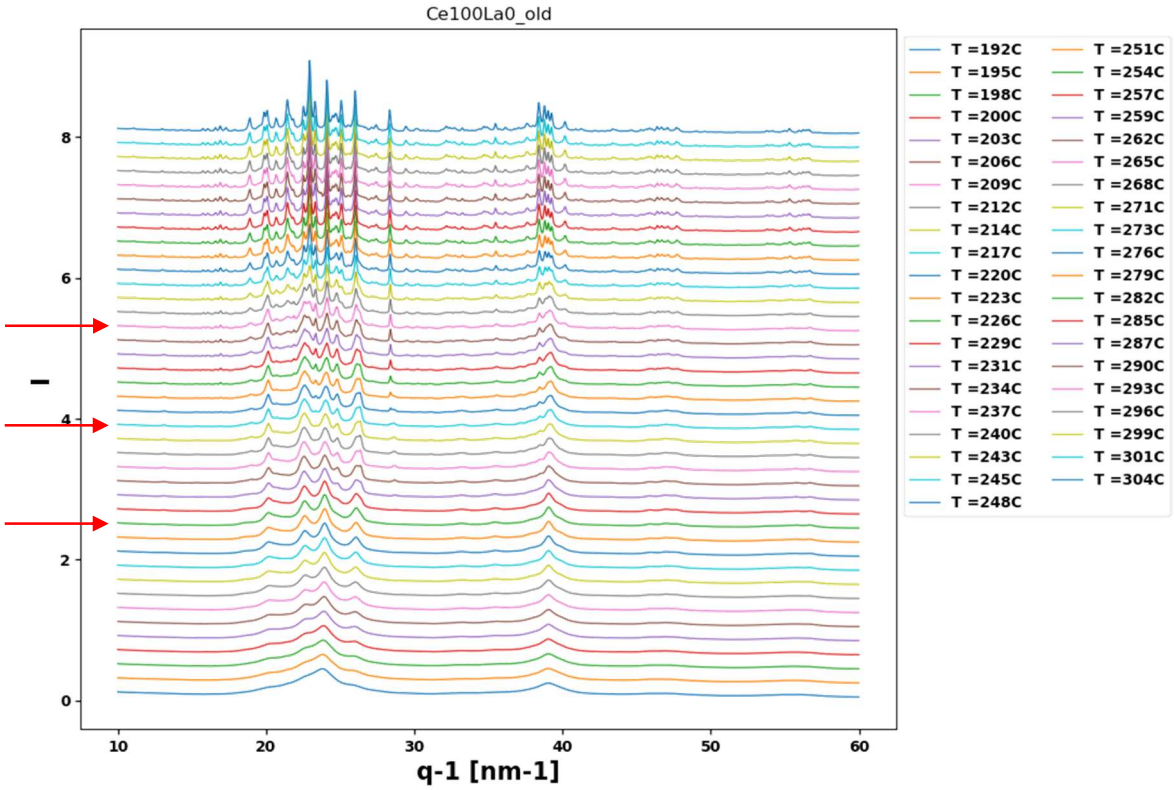

***Figure 4.37**: WAXS intensity patterns for Ce100La0 heated at 5 K/from 192ºC to 304ºC. The temperatures 264ºC, 274ºC and 285ºC, thought to correspond to the onset of the three overlapping peaks in the DSC are highlighted by red arrows*

At 226ºC, the WAXS signal shows sharp and defined peaks, which are characteristic of the crystalline structures. The SAXS signal increases significantly and rapidly during this initial process and then slows down around 240ºC. This increase affects the entire q range, indicating the formation of new crystals and the simultaneous growth of those already present. Regarding the peak with onset at 246ºC, the WAXS signal shows the formation of new crystalline peaks, while changes in the SAXS signal are very subtle and characterized by a slight decrease in the signal at high q values. The limited variations in the SAXS signal suggest the formation of crystals with low contrast relative to the rest of the material or in

extremely small quantities. At the end of this second transformation, the WAXS signal continues to clearly display the two initial amorphous halos. Finally, at approximately 266ºC, there is a further decrease in the SAXS signal at higher q values and an increase at lower values. In the WAXS signal, new peaks appear, and the amorphous background diminishes. Additionally, the crystalline peaks, which are still somewhat broad and previously associated with nanocrystallization, tend to narrow. This final transformation can therefore be interpreted as a process involving the formation of new crystals and the growth of both these and the ones already formed.

4.5 Comparison

In this section, a brief comparison will be made between all the studied compositions.

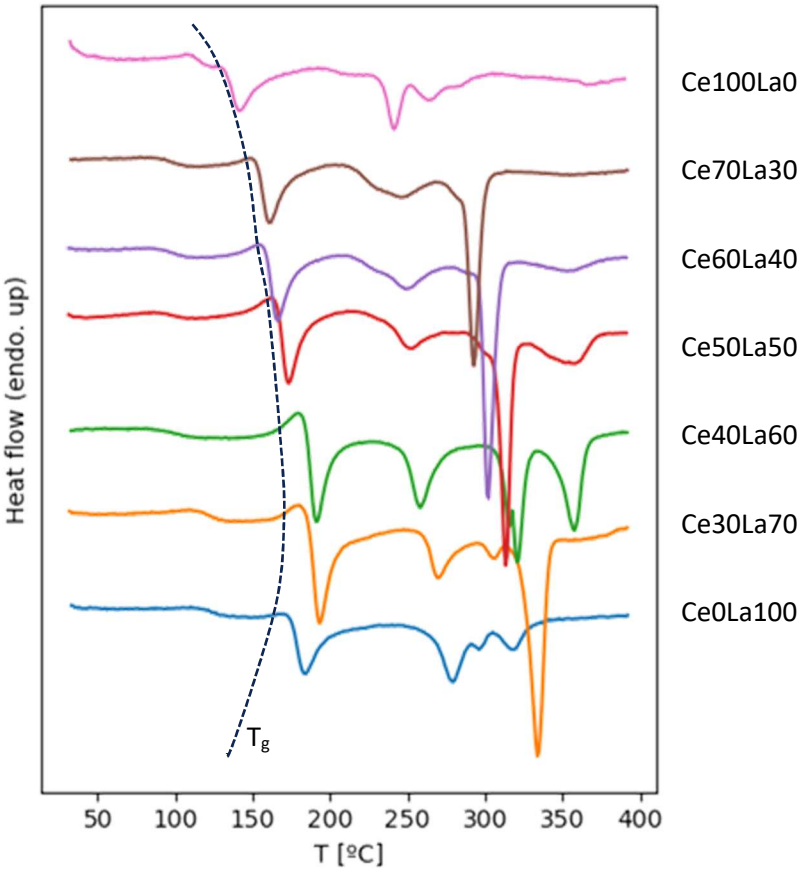

***Figure 4.38**: DSC scans of the analyzed compositions using a rate of 5K/min. The dashed line connects the glass transition temperatures of the various samples*

Figure 4.38 shows the DSC scans of the analyzed compositions using a rate of 5K/min. In all cases relaxation phenomena can be observed before the glass transition, which occurs at T_g. In table 4.2 are reported the glass transition temperatures for all the compositions.

Composition	T_g [ºC]
Ce0La100	~160
Ce30La70	~170
Ce40La60	~160
Ce50La50	~155
Ce60La40	~145
Ce70La30	~140
Ce100La0	~125

***Table 4.2**: glass transition temperature for all the analysed compositions*

The glass transition temperature decreases with the content of cerium in the compositions which contains this element and is maximum for Ce30La70. For Ce0La100, T_g is lower than for Ce30La70. This result is reasonable as metallic glasses with four elements tend to have a higher T_g compared to those with three elements, as the additional element can enhance the stability of the amorphous structure. The XRD analysis in the range of temperature associated to relaxation do not show any change.

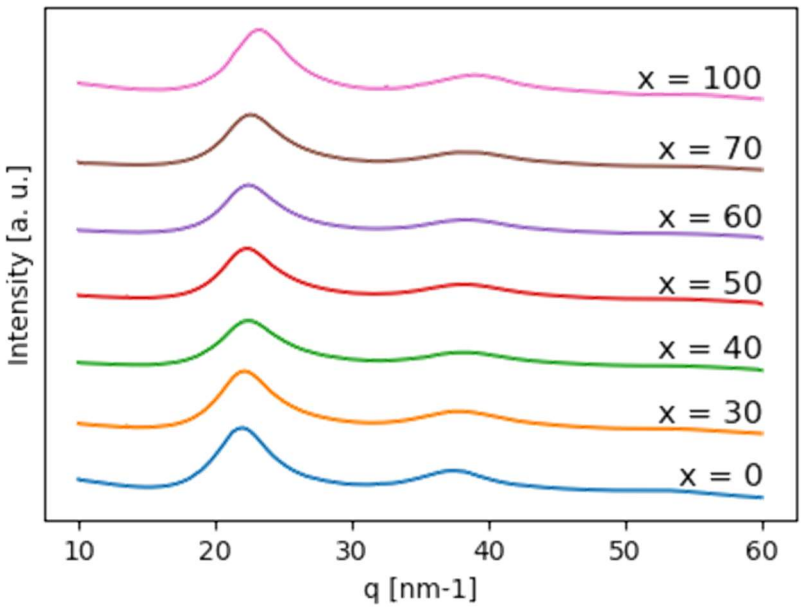

***Figure 4.39**: WAXS patterns of the as-prepared samples. x is the percentage of Ce considering the total amount of Ce and La in the material*

Figure 4.39 shows the WAXS patterns of the as-prepared samples. The broad diffraction maxima in the curves confirm the initial amorphous structure of all the samples. From the comparison between the values of q for which the intensity is maximum, it is obvious that these values are higher as cerium content increases. Since the parameter q is inversely proportional to the distance between the atoms in the real lattice of the material, we can conclude that the atomic density of the glass increases with the cerium content. This result is reasonable given the smaller atomic radius of cerium compared to lanthanum.

The first exothermic phenomenon is the structural relaxation, during which none of the samples show variations in SAXS and WAXS.

The subsequent phenomenon is more complex to compare because, in this case, there is no common behaviour among all the compositions, despite the DSC peaks being very similar to each other, as seen in the previous paragraphs. Figure 4.40 shows the WAXS signal at the onset and at the offset of the LLT peak for all the compositions.

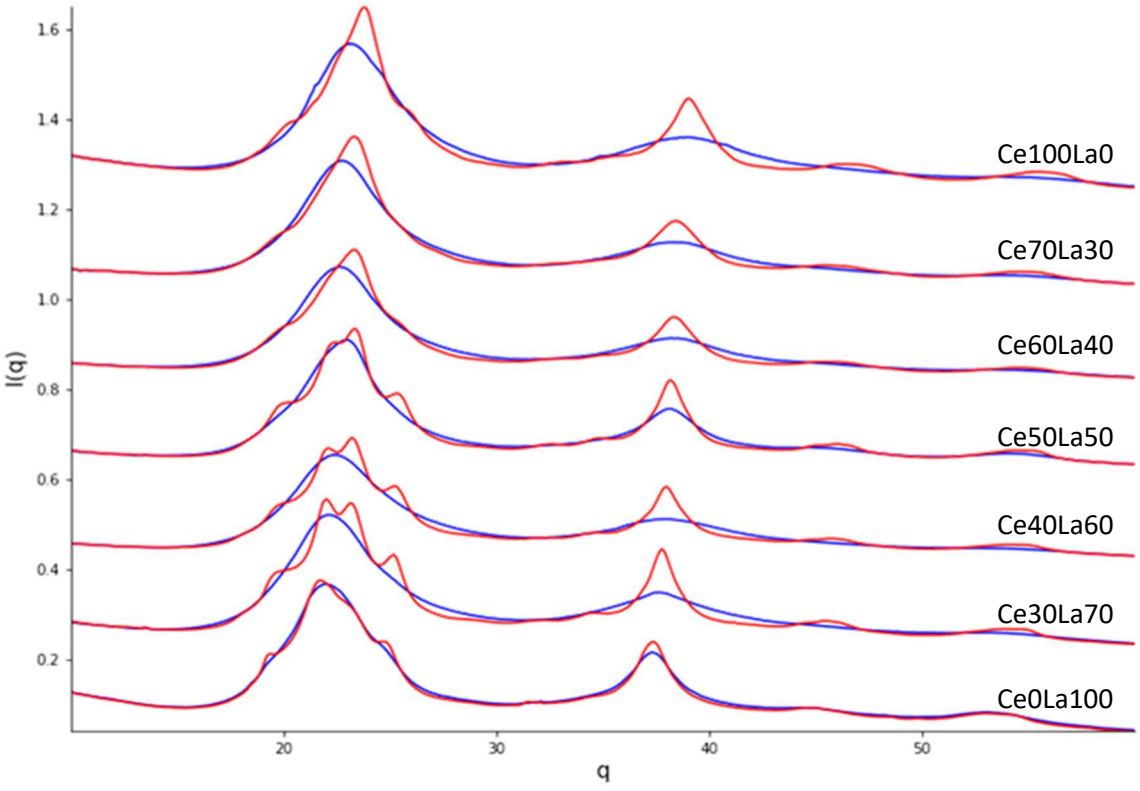

***Figure 4.40**: WAXS patterns of the samples at T_1 (blue) and at the offset (red) of the correspondent DSC peak*

Observing the image, there is a clear difference in the qualitative trend of the WAXS signal for Ce100La0 (practically the same as Ce70La30 and Ce60La40) and Ce0La100. In the former, the first peak grows towards higher q values, while in the latter, a slight peak forms at lower q values. Regarding the compositions Ce50La50, Ce40La60 and Ce30La70, these seem to present both types of peaks at the end of the transformation. For this reason, it can be suggested that for these three compositions, the structure at the end of the transformation is a mixture of the two types of features observed in Ce100La0 and Ce0La100. A possible explanation is that in Ce100La0, Ce70La30, and Ce60La40, as well as in Ce0La100, there was a transition from one amorphous state to another amorphous state. For Ce50La50, Ce40La60 and Ce30La70, however, the system may have undergone a transition from an amorphous phase to a system that decomposes into two amorphous phases: one rich in Ce (similar to that formed in Ce100La0, Ce70La30 and Ce60La40) and one rich in La (similar to that obtained in Ce0La100). This hypothesis agrees with the variation in the SAXS signal seen for the Ce30La70 composition, which could be due to the different electron density of the two separated phases. From the comparison between the various compositions, we can also note that for Ce100La0, the transition is accompanied by densification of the material, observable from the narrowing of the two peaks. Meanwhile, for Ce0La100, there is a rather slight increase in the intensity of the second amorphous halo, which could be associated with the greater order without observing shifts to the right or left of the q value. Regarding the first amorphous "peak" (around q=22), it starts to undulate, suggesting a rearrangement of the atoms into more ordered structures. These differences could be due to the different mechanism of amorphous-amorphous transition: for cerium-based glasses, it is due to the delocalization of 4f electrons with changing the external conditions (in this case temperature), while for lanthanum-based glasses, which do not have 4f electrons, the transition seems to be due to reorganization of the atomic structure driven by changes in external conditions.

Due to the increase in the SAXS signal and the formation of WAXS peaks that are quite broad but still exhibit maxima corresponding to well-defined q values, the subsequent phenomenon at higher temperatures has been considered to correspond to the formation of crystals with sizes too small to be visible through FIBSEM. Considering that for Ce0La100 composition the presence of an intermediate DSC peak, faint and overlapping another one between T1 and the Three final crystallization peaks, had been hypnotized – and considering the similarity with the SAXS and WAXS signal observed in other compositions (Figure

4.41) – it is thought that the invisible overlapping peak could be due to this nanocrystallization phenomenon. This theory is partially supported by the fact that, even for the other compositions, the associated DSC peak is quite broad and has reduced intensity, so its not surprising that it might disappear when overlapping another one. However, it would be better to conduct further investigations on this composition.

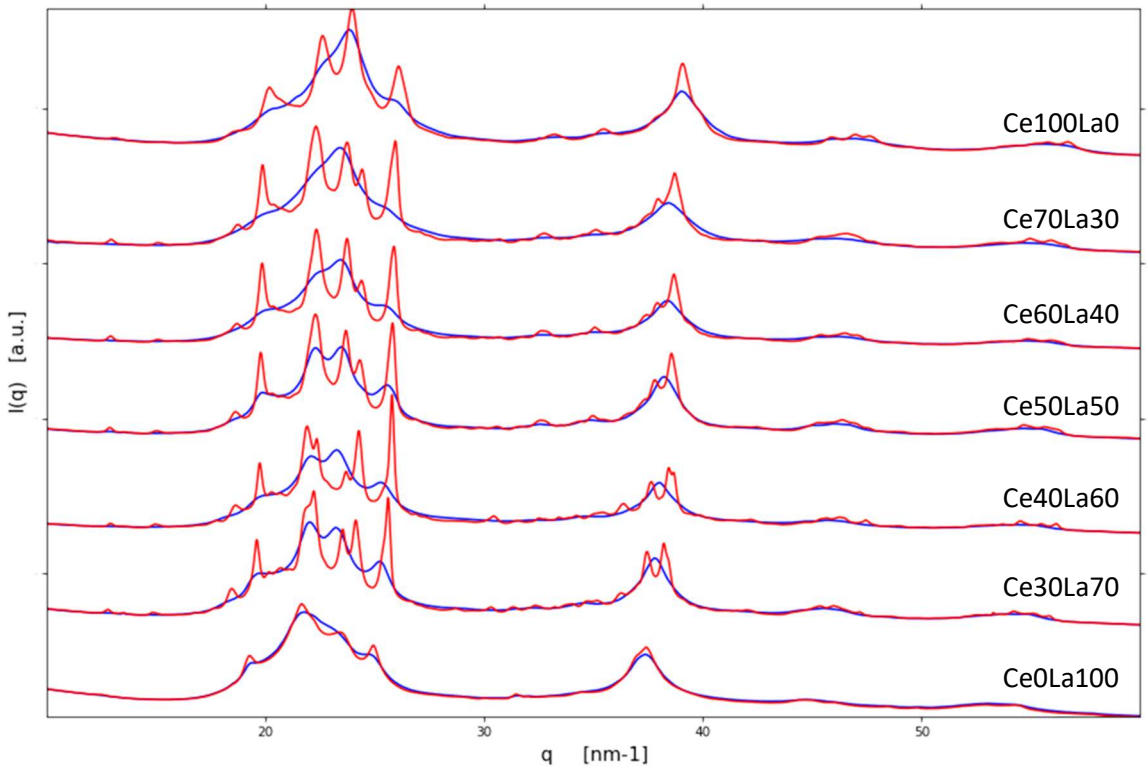

***Figure 4.41**: WAXS patterns of the samples at the beginning (blue) and at the end (red) of the DSC peak thought to be associated to nanocrystallization*

As in the previous phenomenon, it can be observed here as well that the compositions containing both Ce and La exhibit WAXS signal that are a sort of weighted average of the two compositions that contain only one of these elements. Therefore, it is possible that, in the compositions containing both elements, crystals of both typed are formed. However, to verify this, it would be necessary to conduct a more in-depth WAXS analysis, relying on databases to identify the phases formed.

Finally, figure 4.42 shows the results of the crystallization phenomena obtained at the end of the treatment. The first observation concerns the qualitative difference in the behaviour of the WAXS signal for the various compositions. In glasses containing both iron and lanthanum, many peaks are common, while the WAXS signals of the Ce100La0 and

Ce0La100 are very different. From this, for the compositions containing both the elements, it can be concluded that crystals have formed with a unit cell containing both Ce and La. However, since some differences are observed, it is possible that the excess element, relative to stoichiometric ratio of the crystal, has formed other types of crystals. For example, in the case of Ce70La30, La might have been used together with Ce to form a crystalline structure common to all the quaternary compositions, while the remaining Ce might have formed additional crystals. The rather flat background, on the other hand, suggests an almost complete crystallization that occurred in all the samples, as also confirmed by the FIBSEM analysis.

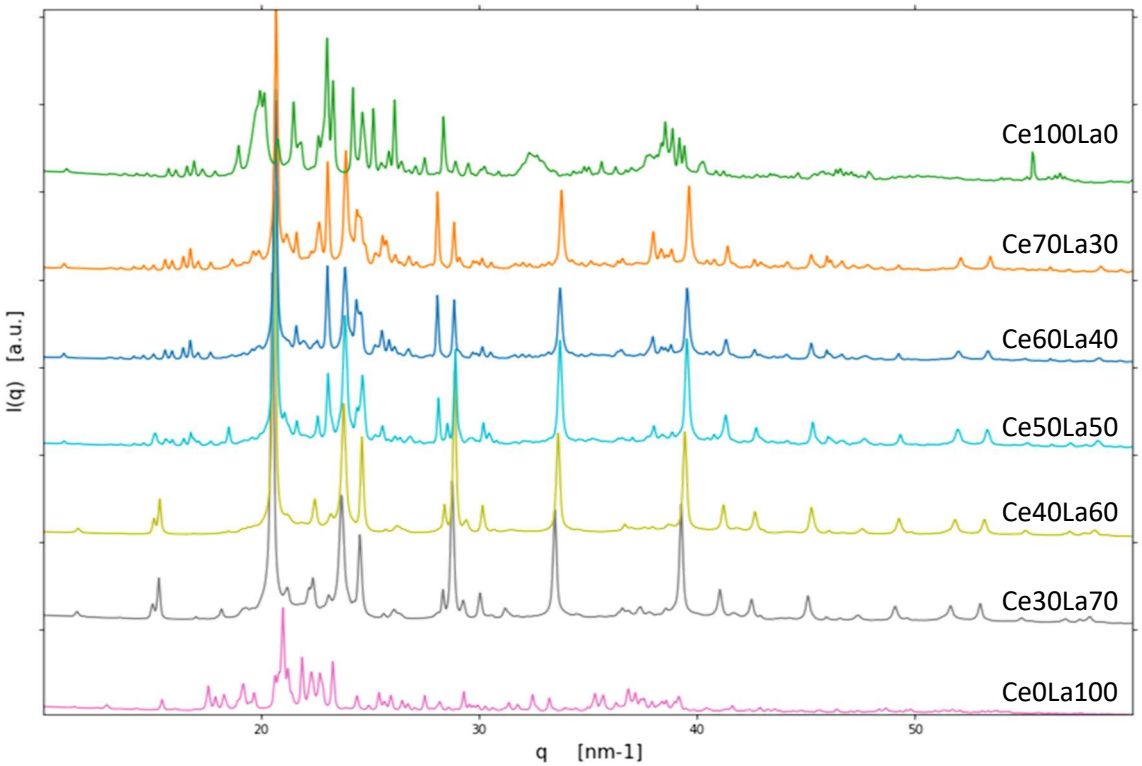

***Figure 4.42**: WAXS patterns of the samples at the end of the DSC treatment (heated to around 380°C)*

5 Conclusions

The study has highlighted the thermal phenomena that the metallic glasses ($Ce_xLa_{1-x})_{65}Al_{10}Co_{25}$ (x=1, 0.7, 0.6, 0.5, 0.4, 0.3, 0) can undergo, along with the associated structural changes. For all the analysed samples, it is believed that, following the initial structural relaxation, a transition between two amorphous phases (AAT) occurs. This transition might be associated with different mechanism depending on the composition and, in some cases (Ce50La50, Ce40La60 and Ce30La70), seems to be followed by a separation of the amorphous phases. After this initial process, nanocrystallization phenomena take place, eventually leading to a full crystallization that results in the almost complete disappearance of the amorphous phase. Additionally, in all cases, a reduction in some WAXS peaks previously formed has been observed, alongside the simultaneous formation and growth of others. This suggest the formation of metastable phases that later disappear when more stable phases appear and that the elements of already-formed crystals are utilized to form the new ones.

To advance this study and obtain further results it would be useful to perform high-resolution characterization of the samples through TEM analysis. Furthermore, the research presented here has been predominantly qualitative. However, WAXS signals could be interpreted using software and databases to determine the phases formed, while SAXS signals could be analysed more quantitatively through Guinier, Kratky, Porod, and IFT analyses. These methods could provide valuable insights into the size and shape of the particles, as well as their tendency to aggregate.

All the described phenomena occur at relatively low temperatures compared to what is observed in other glasses, especially for compositions with a higher Ce content: for example, for the analysed glasses, the glass transition temperatures range between 125ºC and 160ºC, which are significantly lower compared to those based on Zr or Fe, which have T_g values exceeding 330ºC. In the context of applications, it is crucial to understand these limits to

prevent transformations from occurring during the product's usage. In this regard, it would be both appropriate and insightful to investigate how the electrical, magnetic, and mechanical properties of these materials change under varying environmental conditions and compositions. Such research would be valuable for determining whether the property of interest is affected by the conditions (temperature, pression, corrosive environment,..) to which it will be exposed. Additionally, it would be important to assess whether the introduction of La, aimed at increasing the temperature resistance, has an impact on the properties of interest.

In summary, this study has laid the groundwork for understanding the thermal and structural behaviour of $(Ce_xLa_{1-x})_{65}Al_{10}Co_{25}$ metallic glasses, offering valuable insights into their crystallization processes and phase transitions. By combining advanced characterization techniques with quantitative analyses, future research could enhance our knowledge and pave the way for the practical optimization of these materials.

References

[1] Greer A.L. (2015). 4 – Metallic Glasses. In Laughlin, D.E. Hono, K. (edited by) *Physical Metallurgy – Volume 3* (p. 305-385). Elsevier

[2] Stachurski Z.H. (2015). 3.1.1 – Solidification. In *Fundamentals of Amorphous Solids: Structure and Properties* (p. 108-113). John Wiley & Sons

[3] Pelletier J.M., Qiao J. (2019). 18 – Metallic Glasses. In Musgraves, J.D. Hu, J., Calvez, L. (editors) *Springer Handbook of Glass* (p. 617-643). Springer Handbooks

[4] Shmueli U. (2007) 1 – Symmetry in crystals: fundamentals. In Theories and Techniques of Crystal Structure Determination (p. 1-28). Oxford University Press

[5] Conradt R. (2019). 2 – Thermodynamics and Kinetics of Glass. In Musgraves, J.D. Hu, J., Calvez L. (editors) *Springer Handbook of Glass* (p. 51-77). Springer Handbooks

[6] Klinger M. (2013). Glassy Disordered Systems: Glass Formation And Universal Anomalous Low-energy Properties (Soft Modes*)*. World Scientific

[7] Chen M. (2011). A brief overview of bulk metallic glasses, In *NPG Asia Mater – Volume 3* (p. 82-90). Tokyo Institute of Technology

[8] Greer A.L. (2009). Metallic glasses… on the threshold. In *Materials Today – Volume 12* (p. 14 – 22)

[9] Wang X, Zhang M. (2023). 1 – Introduction. In *Metallic Glasses and Their Oxidation* (p. 3-12). Elsevier

[10] Johnson W.L. (1999). Bulk Glass-Forming Metallic Alloys: Science and Technology. In *MRS Bulletin – Volume 24* (p. 42-56)

[11] Stachurski Z.H, Wang G, Tan X. (2021). 1 – Introduction. In *An introduction to Metallic Glasses and Amorphous Metals* (p. 1-7), Elsevier

[12] Chattopadhyay C, Satish Idury K. S. N, Murty B. (2016). Critical evaluation of glass forming ability criteria. In *Materials Science and Technology – Volume 3* (p. 380-400)

[13] Rafique M.M.A, (2021). 2 – Bulk metallic glasses (BMGs) and bulk metallic glass matrix composites (BMGCs). *In Bulk Metallic Glasses and Their Composites - Additive Manufacturing and Modeling and Simulation (2nd Edition)* (p. 5-55)

[14] Johnson L.W. (1999) Bulk Glass-Forming Metallic Alloys: Science and Technology. In *MRS Bulletin – Volume 24* (p.42-56)

[15] Inoue A. (2000). Stabilization of metallic supercooled liquid and bulk amorphous alloys. In *Acta Materialia* – Volume 48 (p. 279-306)

[16] Louzguine-Luzgin D.V, Inoue A. (2013). 3 – Bulk Metallic Glasses: Formation, Structure, Properties, and Applications. In *Handbook of Magnetic Materials – Volume 21* (p. 131-171). Elsevier

[17] Russew K, Stojanova L. (2016). 4 – Viscsous Flow Behaviour of Amorphous Ribbonlike Metallic Alloys Depending on Different Factors. In *Glassy Metals* (p. 1-7). Springer Berlin, Heidelberg

[18] Van den Beukel A, Sietsma J. (1990) The glass transition as a free volumen related kinetic phenomenon . In *Acta Metallurgica et Materialia – Volume 38, Issue 3* (p. 383-389)

[19] Hajime Tanaka (2020) Liquid–liquid transition and polyamorphism. In *The Journal of Chemical Physics – Volume 153*

[20] Hirata A, Guan P, Fujita T, Hirotsu Y, Inoue A. Yavari, A.R. Sakurai, T. Chen, M. (2011) Direct observation of local atomic order in a metallic glass. In *Nature Materials – Volume* (p. 28-33)

[21] Wang X, Zhang M. (2023). 2 – Metallic Glasses. In *Metallic Glasses and Their Oxidation* (p. 3-12). Elsevier

[22] Sheng H.W, Luo W.K, Alamgir F.M, Bai J.M, Ma E. (2006). Atomic packing and short-to-medium-range order in metallic glasses. In *Nature – Volume 439* (p. 419-425)

[23] Stachurski Z.H, Wang G, Tan, X. (2021). 5 – Models of structures. In *An introduction to Metallic Glasses and Amorphous Metals* (p. 137-155), Elsevier

[24] Miracle D.B. (2004) A structural model for metallic glasses. In *Nature Materials – Volume 3* (p. 697-702)

[25] Miracle D.B. (2012) A Physical Model for Metallis Glass Structures: An Introduction and Update. In *JOM – Volume 64* (p. 846-855)

[26] Bakkal M, Karaguzel U, Kuzu A. T. (2019). 6 – Manufacturing Techniques of Bulk Metallic Glasses. In *Modern Manufacturing Processes (eds M. Koc, T. Ozel)* (p. 137-148)

[27] Greer A. L., Costa M. B., Houghton O.S. (2023) Metallic Glasses in *MRS bulletin* – Volume 48 (10, p. 1054-1061), Springer International Publishing

[28] Wang S (2016) Corrosion Resistance and Electrocatalytic Properties of Metallic Glasses In *Metallic Glasses - Formation and Properties*. InTech

[29] Zhao K, Luo Q, Zhao D. Q, Bai H. Y, Pan M. X, Wang, W. H. (2009). Bulk metallic glasses based on binary rare earth elements. In *Journal of Non-Crystalline Solids – Volume 355, Issues 16-17* (p. 1001-1004)

[30] Zhang B, Zhao D.Q, Pan M. X, Wang R. J, Wang W. H. (2006) Formation of cerium-based bulk metallic glasses. In *Acta Materialia – Volume 54, Issue 11* (p.3025-3032)

[31] Belhadi L, Decremps F, Pascarelli S, Cormier L, Le Godec Y. Et al. (2013) Polyamorphism in cerium based bulk metallic glasses: Electronic and structural properties under pressure and temperature by x-ray absorption techniques. In *Applied Physics Letters – Volume 103*

[32] Zhang B, Zhao D.Q, Pan, M. X, Wang W. H. (2004) "Soft" bulk metallic glasses based on cerium. In *Applied Physics Letters – Volume 85* (p. 61-63)

[33] Lou H, Zeng Z, Zhang F. *et al.* (2020) Two-way tuning of structural order in metallic glasses. *Nature Communications – Volume 11*, *Article 314*

[34] Luo Q, Schwarz B, Swarbrick J. C, Bednarcik J, Zhu Y, Tang M, Zheng L, Li R, Shen J, Eckert J (2018) Local-structure change rendered by electronic localization-delocalization transition in cerium-based metallic glasses. In *Physical Review B – Volume 97 – Issue 6*

[35] Decremps F, Morard G, Garbarino G, Casula M (2016) Polyamorphism of a Ce-based bulk metallic glass by high-pressure and high-temperature density measurements. In *Physical Review B – Volume 93*

[36] Xu L, Buldyrev S. V, Giovambattista N, Angell C. A, Stanley H. E (2009) A monatomic system with a liquid-liquid critical point and two distinct glassy states. In *The Journal of Chemical Physics*

[37] Qiao J.C, Pelletier J.M, Blandin J.J, Gravier S (2013) High temperature deformation in a lanthanum based bulk metallic glass showing a pronounced secondary relaxation. In *Materials Science and Engineering – Volume 586* (p. 57-61)

[38] Qiao J.C, Pelletier J.M (2012) Dynamic mechanical analysis in La-based bulk metallic glasses: Secondary (β) and main (α) relaxations. In *Journal of Applied Physics*

[39] Wang Z, Yu H. B, Bai H. Y, Wang W. H (2011) Pronounced slow β-relaxation in La-based bulk metallic glasses. In *Journal of Physics: Condensed Matter – Volume 23*

[40] Qiao J.C, Pelletier J.M (2014) Dynamic Mechanical Relaxation in Bulk Metallic Glasses: A Review. In *Journal of Materials Science & Technology – Volume 30*

[41] Yu H.B, Wang Z, Wang W. H, Bai H. Y (2012) Relation between β relaxation and fragility in LaCe-based metallic glasses. In *Journal of Non-Crystalline Solids – Volume 358 – Issue 4* (p. 869-871)

[42] Ran Li, Shujie Pang, Chaoli Ma, Tao Zhang (2007) Influence of similar atom substitution on glass formation in (La–Ce)–Al–Co bulk metallic glasses. In *Acta Materialia – Volume 55 – Issue 11* (p. 3719-3726)

[43] Rong C, Shan B. (2018). Nanocrystalline and nanocomposite permanent magnets by melt spinning technique. In *Chinese physics B – Volume 27.11*

[44] Gaisford, S. Kett, V. Haines, P. (2016). 5 – Differential Scanning Calorimetry. In *Principles of Thermal Analysis and Calorimetry (2nd Edition)* (pp. 67-103). Royal Society of Chemistry (RSC).

[45] Wachs, Israel, E. Bañares, Miguel A. (2023). 46.2.1 Heat Flux DSC. In Springer Handbook of Advanced Catalyst Characterization (p. 1034). Springer Nature

[46] Schnablegger, H. Singh, Y. (2013). The SAXS Guide Getting acquainted with the principles 3rd edition. Anton Paar GmbH

[47] Cantor, B. (2020). 2 – Bragg's Law. In *Equations of Materials* (p. 24-44). Oxford University Press

[48] ALBA Synchrotron. BL11-NCD-SWEET – non crystalline diffraction. Available at: https://www.albasynchrotron.es/en/beamlines/bl11-ncd [Accessed: June 21, 2024]

[49] PyFAI. Fast Azimuthal Integration using Python — pyFAI 2024.5.0 documentation. Available at: https://pyfai.readthedocs.io/en/stable/# [Accessed: June 21, 2024]

[50] B. Schwarz, U. Vainio, N. Mattern, S.W. Sohn, S. Oswald, D.H. Kim, J. Eckert (2011) Combined in-situ SAXS/WAXS and HRTEM study on crystallization of (Cu60Co40)1−xZrx metallic glasses. In *Journal of Non-Crystalline Solids – Volume 357 – Issue 6* (p. 1538-1546)